View metadata, citation and similar papers at core.ac.uk

brought to you by CORE

provided by CURVE/open

A review of the changes of internal state related to high temperature creep of polycrystalline metals and alloys

Chen, B. , Flewitt, P. E. J. , Cocks, A. C. F. and Smith, D. J.

Author post-print (accepted) deposited in CURVE April 2016

Original citation & hyperlink:
Chen, B. , Flewitt, P. E. J. , Cocks, A. C. F. and Smith, D. J. (2015) A review of the changes of internal state related to high temperature creep of polycrystalline metals and alloys. International Materials Reviews, volume 60 (1): 1-29
http://dx.doi.org/10.1179/1743280414Y.0000000041

DOI 10.1179/1743280414Y.0000000041
ISSN 0950-6608
ESSN 1743-2804

Publisher: Taylor and Francis

Copyright © and Moral Rights are retained by the author(s) and/ or other copyright owners. A copy can be downloaded for personal non-commercial research or study, without prior permission or charge. This item cannot be reproduced or quoted extensively from without first obtaining permission in writing from the copyright holder(s). The content must not be changed in any way or sold commercially in any format or medium without the formal permission of the copyright holders.

This document is the author's post-print version, incorporating any revisions agreed during the peer-review process. Some differences between the published version and this version may remain and you are advised to consult the published version if you wish to cite from it.

CURVE is the Institutional Repository for Coventry University

Manuscript
Click here to download Manuscript (NOT PDF AT REVISE STAGE): Internal stress review_revised version.docx

A Review of the Changes of Internal State Related to High Temperature Creep of Polycrystalline Metals and Alloys

B. Chen[a,*,1], P.E.J. Flewitt[b,c], A.C.F. Cocks[d], D.J. Smith[a]

[a]*Department of Mechanical Engineering, University of Bristol, Bristol BS8 1TR, UK*
[b]*Interface Analysis Centre, University of Bristol, 121 St Michael's Hill, Bristol, BS2 8BS, UK*
[c]*H.H. Wills Physics Laboratory, University of Bristol, Tyndall Avenue, Bristol, BS8 1TL, UK*
[d]*Department of Engineering Science, University of Oxford, Parks Road, Oxford, OX1 3PJ, UK*
[*]Corresponding author. Tel.: +44 117 331 5941. Fax: +44 117 929 4423.
E-mail address: bo.chen-2@manchester.ac.uk

Abstract

When polycrystalline metals and their alloys are used at high temperature, creep deformation leads to changes of their internal state. The change in internal state manifests itself in many ways, but two that concern us in this review are (i) the creation of internal stress arising from the strain incompatibility between grains and/or the formation of cell/sub-grain structures; and (ii) a change in the material resistance. This review aims to provide a clear separation of these two concepts by exploring the origin of each term and how it is associated with the creep deformation mechanism. Experimental techniques used to measure the internal stress and internal resistance over different length-scales are critically reviewed. It is demonstrated that the interpretation of the measured values requires knowledge of the dominant creep deformation mechanism. Finally, the concluding comments provide a summary of the key messages delivered in this review and highlight the challenges that remain to be addressed.

Keywords: Internal stress, Internal resistance, Back stress, Deformation inhomogeneity, Creep, Dislocation structure, Polycrystal

Nomenclature

A	Constant used in the power-law creep equation
a	Constant used in the creep rate equation proposed by Lagneborg
b	Length of the Burgers vector
d	Lattice spacing

[1] Present address: Materials Performance Centre, School of Materials, The University of Manchester, Oxford Road, Manchester, M13 9PL

D_0	Reference diffusivity
D_i	Diffusion coefficient of impurities which pin dislocation glide
D_{sd}	Lattice self-diffusion coefficient
E_{hkl}	Diffraction elastic constant for a specific crystallographic plane {*hkl*}
f^{ci}	Area fraction of cell interiors
f^{cw}	Area fraction of cell walls
$\dot{f}^{ci}$	Rate of the area fraction change of cell interiors
$\dot{f}^{cw}$	Rate of the area fraction change of cell walls
G	Shear modulus
I/I_0 and I/I_{max}	Normalised intensity of diffraction peaks
I_c and I_w	Deconvoluted diffraction peaks representing contributions from cell interiors and cell walls
k	The Boltzmann constant
L	TEM measured projected dislocation link length
M	Taylor factor (which is 3 for a texture-free polycrystalline material)
n	Creep stress exponent used in the power-law creep equation
q	Diffraction vector, $q=2\pi/d$
Q	Activation energy for creep
Q^*	Activation energy for creep after taking into account the presence of internal resistance
r_0	Dislocation core radius
R	Radius of curvature of the bowed dislocation
S	TEM foil thickness
T	Absolute temperature
α	Constant describing the strength of the dislocation node
β	Angle between the Burgers vector and the dislocation direction
θ_0	Peak position of the measured diffraction peak
$\Delta\theta_x$	Shift of the two sub-peaks relative to the centre of gravity of the measured diffraction peak, representing contributions from cell interiors and cell walls
$\Delta\theta_c$ and $\Delta\theta_w$	Peak positions of diffraction peaks representing contributions from cell interiors and cell walls
γ	Stacking fault energy
λ	Dislocation link length
λ_{th}	Critical length of a dislocation link
$\theta(\lambda)$	Number distribution of dislocation link length
v	Dislocation glide velocity
$d\delta$	Angle of a unit length of bowed dislocation link
ε	Strain
ε_n	Strain used to define the permanent softening
ε_{in}	Inelastic strain
ε^{ci}	Strain in the cell interiors in the Mughrabi's composite model
ε^{cw}	Strain in the cell walls in the Mughrabi's composite model
ε^{t}	Total strain in the Mughrabi's composite model
ε_{in}^{ci}	Inelastic strain in the cell interiors
ε_{in}^{cw}	Inelastic strain in the cell walls

$\dot{\varepsilon}_c$	Steady state creep rate
$\dot{\varepsilon}_{in}$	Inelastic strain rate
$\dot{\varepsilon}_{in}^{ci}$	Inelastic strain rate in the cell interiors
$\dot{\varepsilon}_{in}^{cw}$	Inelastic strain rate in the cell walls
ρ	Dislocation density
σ_a	Applied stress
σ_p	Creep pre-strain stress
σ_s	Saturation stress in cyclic deformation
σ_{op}	Operative stress
σ_{is}	Internal stress
σ_{is+a}	A sum of the internal stress and the applied stress
σ_{ir}	Internal resistance
$\sigma_{ir}(\lambda)$	Internal resistance associated with dislocation link length
σ_f and σ_r	Flow stress along forward deformation direction and reversed direction
σ_y	Yield strength
σ_{sn}	Permanent softening stress
σ_{is}^{A} and σ_{is}^{B}	Internal stress in grain A and grain B of a body
σ_{ir}^{A} and σ_{ir}^{B}	Internal resistance in grain A and grain B of a body
$\sigma_{is}^{\{hkl\}}$	Internal stress for a $\{hkl\}$ grain family
σ_{is+a}^{ci}	A sum of internal stress at cell interiors and the applied stress
σ_{is+a}^{cw}	A sum of internal stress at cell walls and the applied stress
σ_{is}^{ci}	Internal stress at cell interiors
σ_{is}^{cw}	Internal stress at cell walls
$\dot{\sigma}_{is}^{ci}$	The rate of internal stress change at cell interiors
$\dot{\sigma}_{is}^{cw}$	The rate of internal stress change at cell walls
τ_0	Additional contribution to the internal resistance due to the presence of the other sources
τ_a	Applied shear stress (τ_a is obtained by multiplying the applied stress, σ_a, by Schmidt factor of 0.3 for a polycrystal)
τ_e	Effective shear stress acting on the dislocation to hold the radius of curvature of bowed dislocation
τ_f and τ_r	Shear flow stress along forward deformation direction and reversed direction
τ_{is}	Internal shear stress
τ_{ir}	Internal shear resistance
τ_{sn}	Permanent softening shear stress
$\tau_{is}^{\{hkl\}}$	Internal shear stress for a $\{hkl\}$ grain family
Λ	Mean dislocation spacing

1. General Introduction

Modern technological progress in, for example electrical power generation, demands the use of materials at increasingly higher temperatures. As a consequence of high temperature exposure, the creep behaviour of materials is perhaps one of the most critical factors in considering such applications[1, 2]. This concern has driven a considerable amount of work on the development of creep-resistant alloys[2, 3]. In addition, we require a greater confidence in predicting the overall creep life of engineering components. This applies to the extension of the life for existing power generation plants as well as prediction of the life for future designs.

There are two significant interactive contributions to the creep lifetime of engineering materials, i.e. creep deformation and creep fracture[4]. Materials may deform by several different mechanisms when subjected to an applied stress at high temperature, and it is convenient to present these mechanisms in the form of a deformation mechanism map[5, 6]. Similarly, materials may fracture by several possible mechanisms, and these can be described by a fracture mechanism map[7, 8]. More importantly, over the operational service life, typically ≥200,000h, there is a potential to change the initial microstructure of a material, which can affect both the controlling deformation and fracture mechanisms. In the present review we focus on creep deformation.

As an example, Type 316 austenitic stainless steel is widely used in nuclear power generation plant, such as the UK Advanced Gas Cooled reactors (AGRs). A typical deformation mechanism map for the steady state creep response of this type of steel has been established by Frost and Ashby[6]. The deformation mechanism map was generated by fitting generic models to creep data[6]. Figure 1 shows the deformation mechanism map for this material with a typical grain size of 50μm in the solution treated condition. Power law creep, dominated by dislocation movement, and diffusional creep are the two main high temperature deformation mechanisms, Figure 1. The former dominates at a relatively high stress and the latter at a relatively low stress. Two widely accepted physically based models that describe diffusional creep deformation were proposed by Nabarro-Herring[9, 10] and Coble[11].

Data to support the diffusional creep mechanism are limited, and most designs are assumed to fall within the regime where dislocation mechanisms dominate the material response. Many different forms of constitutive equations have been

proposed to describe dislocation dominated creep deformation[12-18]. These include the power-law relationships employed by Frost and Ashby[6] and exponential and hyperbolic sine relationships[17]. However, to date no unified mechanistic models have been proposed and most of the equations simply provide a functional form of constitutive model that can be fitted to data. Thus the resulting models can be used to predict creep behaviour only within the bounds of test data[19]. There are at least two obvious drawbacks associated with the development of constitutive equations in this way: (i) the difficulty of transferring the model from one tested material to another and (ii) the limitation of predicting material behaviour beyond the test data range. This leads to the requirement of an expensive creep test programme of work to develop long term creep lifetime predictions.

Because of the incomplete understanding of the dislocation creep deformation mechanisms, most mechanistic models can provide only a good prediction for nominally pure metals and simple solid solution alloys[1, 15, 18, 20]. Nevertheless, there has been some success recently in the development of mechanistic models for the behaviour of nickel based superalloys[21, 22]. Therefore, the development of physically based creep deformation models is required and remains a significant challenge, particularly if we wish to determine the creep behaviour of many engineering alloys for long durations.

A useful method for describing the creep deformation of polycrystalline materials, i.e. creep deformation rate, $\dot{\varepsilon}_c$, is to recognise that the mechanical response of a material is based upon the current state of the microstructure (i.e. internal state), temperature and applied stress[23]. The change in internal state is manifested in many ways[15, 23-27]. For example, creep deformation leads to a change in the internal state of the material. The influence of the microstructural changes during long term service on the creep strain rate has been reviewed in 9 to 12 wt.% chromium steels[28]. The present review focuses on two characteristic features of the internal state: internal stress and internal resistance. The first is a consequence of the strain incompatibility between grains and/or the formation of cell/sub-grain structures. The second relates to a change in the material resistance to dislocation motion and thereby the creep deformation. In the remainder of this paper we examine these features within the framework of the power-law creep relationships as employed by Frost and Ashby[6], which is appropriate for the long term creep problems that are of primary interest here.

There has been a widespread acceptance of the idea that creep deformation is not driven by the applied stress but rather by an operative stress. Sometimes this operative stress is seen as the difference between the applied stress and the so-called "internal stress", often considered to be representative of the material internal state[29, 30]. Many different terms have been used to describe this internal stress concept, such as back stress[29], friction stress[31, 32], threshold stress[33] and residual stress[34]. By incorporating a certain value of "internal stress", attempts to reconcile differences between the theoretically derived creep stress exponents of the steady state creep rate and the experimental observations have been considered[30]. To validate the value of stress which has been incorporated into a creep deformation model, many experimental techniques have been developed to measure the internal stress[26, 35-38]. However, different measurement techniques seem to provide different magnitudes of the internal stress in the same material under very similar creep test conditions. For example, Blum and Finkel[38] creep tested an Al-11 wt.% Zn alloy at 300°C for a range of applied stresses from 5.5MPa to 18.4MPa. Both conventional and modified strain transient dip test techniques were used to measure the "internal stress". Different magnitudes of internal stress were obtained depending on the technique adopted and the model employed to interpret the measured values. Therefore, data from measurements of internal stress do not necessarily permit a critical comparison with the theoretical derivations of the internal stress. Ambiguous definitions of internal stress and the inability to separate the internal stress from the internal resistance at different length-scales are two potential reasons leading to the contradictions.

In section 2 of this review, creep mechanisms associated with the dislocation structures in different classes of materials are briefly reviewed. In section 3, the concepts of internal stress and internal resistance are established. The mechanistic creep deformation models incorporating internal stress and internal resistance terms are critically assessed in section 4. In section 5, the techniques available to measure both at different length-scales are critically assessed. Finally, concluding comments are given in section 6.

2. Dislocation Mechanisms in Creep

2.1. Introduction

When a polycrystalline material is subjected to applied stress at elevated temperatures, dislocation associated deformation requires the dislocations to overcome the intrinsic lattice resistance (Peierls force) and obstacles such as other dislocations, solute elements and second-phase particles/precipitates[39]. Thus, the magnitude of the resistance to dislocation motion is determined by the overall dislocation structure and density, the distribution and types of solute elements, and particles/precipitates.

For a range of materials, including pure metals[13, 40, 41], solid solution alloys[13, 20, 42-44] and engineering materials[42, 45, 46], the most widely used form of the power-law creep equation is that originally proposed by Mukherjee et al.[47] and subsequently referred to by several workers[13, 48, 49]:

$$\dot{\varepsilon}_c = \frac{AGb}{kT}\left(\frac{\sigma_a}{G}\right)^n D_0 \exp\left(\frac{-Q}{kT}\right) \quad (1)$$

where $\dot{\varepsilon}_c$ is the steady state creep rate, σ_a is the applied stress and n is the creep stress exponent. A is a dimensionless constant, G is the shear modulus, b is the length of the Burgers vector, k is the Boltzmann constant, and T is the absolute temperature. D_0 is the reference diffusivity and Q is the activation energy for creep. D_{sd} is often used to describe the lattice self-diffusion coefficient and is equal to $D_0\exp(-Q/kT)$. Both the stress and temperature have a major influence on the steady state creep rate, $\dot{\varepsilon}_c$, as illustrated in Figure 1. Different dislocation creep mechanisms produce different characteristic values of the creep stress exponent, n: (i) dislocation sub-structure formation gives rise to a value of n about 5[13, 16, 40]; (ii) viscous glide controlled creep gives rise to a value of n about 3[50-54]; and (iii) power-law-breakdown (PLB) produces a value of $n>5$, with a generally decreased activation energy compared with self-diffusion[36, 55-59]. This is due to the dominance of dislocation core diffusion in this creep regime[6, 60].

Following Mukherjee et al[47], it is instructive to examine creep data in terms of a normalised steady state creep rate, $\dot{\varepsilon}_c kT/D_{sd}Gb$, and a normalised applied stress, σ_a/G.

This allows the behaviour of different polycrystalline materials to be classified in terms of their creep stress exponent, n. Figures 2 (a) and (b) show some representative data for the pure aluminum and its alloys, and stainless steels, respectively. The required material parameters in equation 1 were mainly obtained from Frost and Ashby[6].

We will now consider the contribution of different dislocation mechanisms to the creep deformation. These include the role of three dimensional dislocation networks; heterogeneous dislocation cell/sub-grain structures; and the presence of solute elements and particles/precipitates. We examine these different mechanisms within the context of the power-law relationship of equation 1.

2.2. Three dimensional dislocation network arrangement

Dislocations usually build-up a randomly distributed three dimensional dislocation network, with dislocations linked at nodes[39]. The detailed form of the dislocation network depends on both the internal and external factors. The most important internal factor is the stacking fault energy, γ[61, 62]. External factors include the stress and the temperature applied to a material. A low value of γ is associated with a random dislocation structure, which could be due to the difficulty for extended dislocations to cross-slip[61, 63] or climb[64]. Such a dislocation arrangement is observed in austenitic stainless steels at relatively low temperatures[65] and α-brasses[66].

Several transmission electron microscopy (TEM) observations[67-69] have revealed that the three dimensional network generated during creep consists of dislocation links connected at attractive and repulsive nodes. Figure 3 shows a TEM micrograph for a creep deformed 20% Cr-35% Ni stainless steel, where a dislocation node has just broken. Based on observations of this type, Lagneborg[66] and McLean[32] have described a creep process in which creep strain occurs when a dislocation link breaks away from the network and glides on an active slip system, before eventually being arrested by other dislocations in the network. The distribution of link lengths in the dislocation network is determined by two processes: (i) hardening, arising from the increase in dislocation density due to the expansion of the released dislocation; and (ii) recovery, where longer links grow at the expense of smaller ones in a process akin to grain growth. It has been suggested by Suzuki and Imura[70] that smaller dislocation networks are unstable, and grow rapidly by diffusion at high temperatures under the

action of their line tension. Both Lagneborg[66] and McLean[32] argued that a dislocation link can break away from the network if it is longer than a critical value, λ_{th}. Under steady state creep conditions there is a balance between the rates of hardening and recovery that continually supplies dislocations of the critical length required for permanent deformation to occur. Following a stress change, transient behaviour occurs as the dislocation structure evolves towards the steady state structure associated with the new stress level. We discuss this further in sections 4 and 5.

2.3. Heterogeneous dislocation cell/sub-grain structure

For pure metals, such as Al[13] and other F.C.C. metals[40], B.C.C. metals[40] and H.C.P. metals[41], a creep stress exponent of n close to five is often obtained. Creep data for pure Al with n=4.6 are shown in Figure 2 (a). It is well established that a stress exponent, n, close to five is typical of pure metals which develop dislocation sub-structures, i.e. a cell or sub-grain structure[12]. Sub-grain formation requires both dislocation cross-slip and climb to enable rapid rearrangement of dislocations[61, 63, 71]. A model which describes the creep response of the resulting dislocation sub-structure was developed by Blum and his co-workers[72-75] based on the earlier model of Mughrabi[37, 76] for time-independent plastic deformation. In this model, each grain includes two distinct areas: the rectangular cells with thin walls containing dense arrays of dislocations and the cell interiors containing a low density of dislocations. The dislocations in the cell walls produce a large resistance to the motion of dislocations through the walls[37, 76]. As a result, some dislocations in the cell interiors are held-up at the interface between cell walls and cell interiors. At the cell interiors, the dislocations are arranged randomly as a three dimensional network structure, which has been confirmed by TEM observations[1, 77, 78]. We consider this model further in sections 3 and 4.

2.4 Solid solution

For solid solution alloys, Al-Mg[13, 20], Al-Zn[43] and Al-Cu[44] alloys are three typical examples where a creep stress exponent, n, close to three was obtained in the intermediate normalised stress region. Creep data of the Al-2.2 at.% Mg and Al-3.3 at.% Mg alloys are shown in Figure 2 (a), where the creep mechanism is viscous glide

of dislocations[50]. The intermediate normalised stress region for the Al-2.2 at.% Mg is between $\sigma_a/G=3\times10^{-4}$ and $\sigma_a/G=2\times10^{-3}$, where the creep stress exponent n=3.0 was obtained, Figure 2 (a). Both TEM and etch pit observations of creep deformed materials with n close to three have shown either a complete absence of the dislocation cell structure or a sluggish tendency to form a cell structure[50, 79]. Dislocations interact in several possible ways with the solute elements, and as a result dislocation climb is impeded[14, 80]. Cottrell and Jaswon[51] proposed that the drag process arises from the segregation of solute atmospheres to moving dislocations. The dislocation velocity, v, is then limited by the rate of migration of the solute elements. Fisher[52] proposed that dislocation motion destroys the short range order in solid solution alloys and creates an interface. Suzuki[81] proposed a drag mechanism due to the segregation of solute elements to stacking faults. Furthermore, Mohamed[80] concluded that the Suzuki and the Fisher dislocation interactions with solute elements are necessary to predict the creep stress exponent of n=3.

Creep data of Al-3.3 at.% Mg, Figure 2 (a), show a deviation from n=3.2 at $\sigma_a/G>3\times10^{-3}$. This indicates an increase in the value of n with the increasing applied stress. In fact, creep experiments on both Al-3.3 at.% Mg and Al-5.6 at.% Mg conducted by Yavari et al.[50, 82] showed that the stress exponent, n, increased from 3 to 4.6 with the increase in the applied stress. When n was close to three, there was essentially a random distribution of dislocations in the material, but a dislocation sub-structure formed when n was close to five. This indicates that rate controlling process changes to dislocation climb in the region where n=5. It is generally agreed that this is due to the breakaway of dislocations from the solute atmospheres enabling them to glide much faster. The large difference in dislocation velocity between dislocations with and without the presence of the solute atmospheres was measured experimentally[19]. The gradual change from n close to five in pure metals to n close to three in solid solution alloys with increasing concentration of solid solution element, Figure 2 (a), has confirmed a physical relationship between the dislocation arrangement and the value of n. It is clear that dislocation climb and viscous glide represent two competing creep mechanisms in solid solution alloys, where the slower one becomes the rate controlling process.

2.5. Second-phase particles/precipitates

Dispersion strengthening is an efficient mechanism for improving the material strength at relatively low temperatures[83]. Orowan[84] was first to attribute this effect to the resistance of dislocations against bowing between impenetrable obstacles. The magnitude of the bowing stress is determined by the spacing between the obstacles. At elevated temperatures, it has been suggested that the stress required to move dislocations is only a fraction of the Orowan bowing stress[29, 85]. This is because dislocation bowing between particles is an athermal process and depends little on temperature[86]. The experimentally observed critical stress to operate creep deformation in a Ni-20Cr-2ThO_2 single crystal is below the measured Orowan bowing stress[85].

A kinked dislocation configuration, where the presence of local climb facilitates dislocation movement, was proposed by Lagneborg[87]. Reppich[88] suggested that the magnitude of the stress required for local dislocation climb over the particles is within 13 to 45% of the Orowan bowing stress. Dislocation climb models of this type implicitly assume that a dislocation is repelled by a particle. TEM observations of creep deformed oxide dispersion strengthened (ODS) alloys suggest that the detachment of dislocations from the departure side of particles is the rate controlling process, rather than local climb[83, 88-90]. The calculation of the stress required for this process also gave a value smaller than that predicted by Orowan bowing.

Čadek et al.[91] analysed several sets of creep data obtained from aluminium alloy matrix composites reinforced by silicon carbide particulates, silicon carbide whiskers or alumina short fibres. High values of the creep stress exponent, $n>5$, were observed over a range of temperatures from 200°C to 450°C[91]. In addition, a high value of creep stress exponent ($n>5$) was obtained by Lund and Nix[85] in creep tests on an ODS alloy Ni-20Cr-2ThO_2. A schematic of the creep rate as a function of applied stress in dispersion strengthened and dispersion free materials has been produced by Arzt et al.[83] to illustrate three distinct creep regions with their characteristic creep stress exponents, Figure 4. At high strain rates the material approximates the behaviour of the dispersion free materials, with $n=5$ and self-diffusion activation energy. At intermediate strain rates high values of stress exponent and apparent activation energy are often observed. At low strain rates, the stress dependence may decrease again to $n=5$.

The dislocation mechanisms responsible for the deformation of ferritic ODS alloys were studied using TEM, to examine the dislocation structure of creep deformed specimens up to a temperature of 1050°C[92]. At temperatures below 950°C, there was no evidence of sub-grain structure in the creep deformed ODS alloy. At relatively low temperatures from 650°C to 750°C, dislocation motion was observed to be viscous glide controlled by solute drag. At an intermediate temperature range from 750°C to 900°C, a thermally activated detachment of dislocations from oxide particles was judged to be the deformation mechanism[92]. A change in the mode of dislocation interactions with obstacles, i.e. the solute elements and the particles, was used to explain the change in the value of *n* observed in the different creep regimes, Figure 4.

However, it has been demonstrated by Morris[65] that application of the same arguments regarding the dislocation interaction with $M_{23}C_6$ precipitates did not provide a completely satisfactory interpretation of the creep behaviour observed in Type 316H stainless steel. The presence of the $M_{23}C_6$ precipitates was a consequence of high temperature exposure of this material. Morris[65] claimed that the distribution of the precipitates defined the distribution of dislocation link length. When this link length was used for the calculation, a good prediction of the creep strain rate was obtained[65].

2.6. Creep of a complex engineering alloy

Having examined simple pure metals and their alloys as well as dispersion strengthened alloys, we now move to a complex engineering alloy, Type 316H stainless steel. The development of dislocation sub-structure in an austenitic stainless steel is shown in Figure 5. The generation of a typical creep curve, Figures 5 (a) and (b), includes five steps: heating, loading, creep deformation, cooling and unloading. In laboratory creep tests significant plastic deformation generally occurs on initial loading. During this loading step, the dislocation density increases dramatically[69] and the dislocations remain randomly distributed in a three dimensional network, Figure 5 (c). This kind of three dimensional dislocation network may be retained until the end of steady state creep, Figure 5 (d). However, if the temperature of a creep test is high enough, this dislocation structure can re-arrange gradually to form a cell structure, Figure 5 (e), or a sub-grain structure, Figure 5 (f). Both processes allow the material to minimise the overall energy by forming low energy boundaries[25, 39].

The extent of this process depends on stress and temperature and it has been shown to vary grain-to-grain[77, 78]. The grain-to-grain variation is due to the relative orientations of the slip systems to the loading direction, which determines the extent of the local plastic deformation and the evolution of the local dislocation density during deformation.

Creep data of Type 316H stainless steel obtained by Morris and Harries[45] showed various creep stress exponents, up to n=22.3 for the test temperature of 525°C in Figure 2 (b). The presence of a three dimensional dislocation network was observed in the temperature range from 525°C to 625°C[45, 65]. Stress exponents from about n=7 at low stresses to about n=16 at high stresses, generated from several creep tests undertaken at 625°C, were also obtained by Morris[65]. The dislocation structure was characterised as a three dimensional dislocation network for all tests. The high values of creep stress exponents (n>5) seem to indicate a change in the mechanism for dislocation creep deformation, since the theoretical predictions of the creep stress exponent based on dislocation mechanisms are always less than five[18, 30, 65, 66]. Creep data at temperatures from 625°C to 900°C are shown in Figure 2 (b). The creep stress exponent, n, decreases with the increasing temperatures as shown in Figure 2 (b). At test temperatures of 750°C and 900°C, values of creep stress exponent, n=5.8 and n=5.5 are obtained. These values are consistent with the typical value of creep stress exponent in pure metals which develop sub-grain dislocation structures. When the creep tests were undertaken at a relatively high temperature of >625°C[45, 77, 78, 93], sub-grain dislocation structures were obtained for stainless steels.

Creep data of ex-service Type 316H stainless steel were collected by Chen[94] (500°C to 600°C); a creep stress exponent of n=6.4 was obtained, as shown in Figure 2 (b). The dislocation structure in these specimens was likely to be dominated by the three dimensional dislocation network, because of the relatively low test temperatures[45, 65]. In fact, Bhargava et al.[95] observed that the presence of $M_{23}C_6$ precipitates in a Type 304 stainless steel inhibited the formation of sub-grain dislocation structures. A value of n=5.6 is found based on the creep data of Fe-21Cr-37Ni stainless steel[30], Figure 2 (b). Creep tests were undertaken within a temperature range from 600°C to 750°C, where cell or sub-grain structures formed[96]. This value of n is similar to those derived from the creep data of ex-service Type 316H stainless steel (500°C to 600°C) obtained by Chen[94] and the creep data of the same type of steel (>625°C) obtained by Morris and Harries[45], Figure 2 (b). Thus it is likely that

there is no difference in sub-grain structured and three dimensional dislocation structured stainless steels in terms of their creep stress exponents. We explain this in sections 3.3 and 4.5.

2.7. Summary

Different classes of polycrystalline materials have been considered in terms of the dislocation mechanisms operating during creep. In dislocation based creep deformation, dislocation glide and climb are two possible rate controlling mechanisms. Creep in pure metals reveals that the presence of a dislocation sub-structure normally gives a creep stress exponent of n=5, whereas the presence of a three dimensional dislocation network in solid solution alloys gives a creep stress exponent of n=3. Dislocation climb is judged to be the rate controlling mechanism for the former and dislocation glide is the rate controlling mechanism for the latter. For the creep deformation behaviour of engineering alloys, such as Type 316H stainless steel and dispersion strengthened alloys, a higher value of n is often obtained for tests undertaken over a particular range of temperatures and stresses. Both dislocation cell structures and three dimensional dislocation networks are possible in these creep tests. Dislocation interactions with other obstacles are the main reason for high values of creep stress exponent in dispersion strengthened alloys. At a certain range of temperatures, the activation energy for dislocation climb from obstacles becomes the rate controlling factor, rather than the dislocation-dislocation interactions.

3. Internal Stress and Internal Resistance

3.1. Concept

The term “internal stress” has been used ambiguously in creep to describe the internal resistance of the material to creep deformation[29]. Here the operative stress, defined as a difference between the applied stress and the “internal stress”, is the driving force for material deformation. Accordingly, the creep stress exponent describes the dependence of the creep strain rate on the operative stress. Different terms have been used in the literature, including threshold stress[33], back stress[29], internal stress[26], friction stress[31, 32] and residual stress[34]. These terms were introduced

in the context of specific dislocation creep mechanisms.

The term threshold stress is often used to describe the dislocation based creep deformation of dispersion strengthened materials, where a certain value of threshold stress must be overcome in order for dislocations to bypass particles/precipitates[29, 86, 97, 98]. Thus, the threshold stress is the lower limiting stress below which no measurable creep strain can be achieved[99]. It is envisaged that the mobile dislocations are arrested or slowed down at the particles/precipitates, by one of four possible mechanisms[86]: (a) particle shearing, (b) Orowan bowing, (c) global/local climb, and (d) drag of particles/precipitates. Both (a) and (b) are athermal processes. Global and or local climb allows creep to occur at lower stresses than predicted by the athermal processes, because the activation energy for creep becomes lower for dislocation climb[86, 97]. Particle drag requires diffusional rearrangement of the particles under the action of the forces exerted by the mobile dislocations. The diffusion coefficients for the particulate material are generally much smaller than those for the matrix and this process occurs only at large values of the homologous temperature. Therefore particle drag is rarely observed under test conditions of practical importance. In general, the global and or local climb of dislocations around particles is an important mechanism for particle strengthened materials. Hence it is more appropriate to classify the threshold stress as an internal resistance term, reflecting the ease of the dislocation climb limited by the addition of the particles/precipitates.

The term back stress suggests the existence of an opposing stress to resist creep deformation when the material is subjected to an applied stress at high temperature. The occurrence of anelastic strain recovery (backflow) after removing part or all of the applied stress from the creep deformed material has been judged to be an appropriate example for supporting the back stress concept[100]. The backflow is defined as the anelastic strain recovery, opposite to the straining direction at the maximum applied stress. It was claimed by Čadek[30] that the anelastic strain recovery in a material with a heterogeneous dislocation sub-structure could be attributed to two processes: (i) straightening of the bowed dislocation links under the applied stress and (ii) reverse motion of dislocations in the cell interiors towards cell walls. The first process is associated with the disappearance of the equilibrium curvature of dislocation link under an applied stress. Thus this partly reflects the magnitude of the resistance that dislocations must overcome before moving. The second process is associated with the localised internal stress field, such as that described by the

heterogeneous dislocation sub-structure models developed by Dobeš and Blum[72] and Mughrabi[37, 76], Figure 6. In this model compatibility requires dislocations to flow within the cell interiors and through the cell walls. It is more difficult for the dislocations to break through the cell walls and thus a higher shear stress is generated in these regions than within the cell interiors. This is illustrated in Figure 6 for both the stress at cell walls, σ_{is+a}^{cw}, and the stress at cell interiors, σ_{is+a}^{ci}, respectively. After the removal of the applied stress, σ_a, the material unloads elastically. But the occurrence of a significant stress in the cell interiors, σ_{is}^{ci}, results in creep deformation in the reverse direction. Thus the term back stress does not make a clear distinction between the internal resistance and internal stress terms.

The term internal stress in the creep community is used to emphasise that the origin of this stress is from the material internal state. Internal stress and back stress are often used interchangeably by researchers[30, 38]; both are widely used to describe the dislocation related material internal state. The difference between these two terms may occur, when describing a stress state due to the presence of creep induced heterogeneous dislocation sub-structure. An internal forward stress, σ_{is}^{cw}, is associated with the cell walls and an internal back stress, σ_{is}^{ci}, is associated with the cell interiors, as shown in Figure 6.

The term friction stress was used by Wilshire and his co-workers[31, 101, 102] to rationalise large values of creep stress exponents. The friction stress appears to characterise the back stress associated with the heterogeneous dislocation cell structure developed during creep of polycrystalline Cu[31]. Thus, the friction stress takes the meaning of an internal stress term. However, Burt et al.[101] measured the friction stress for dislocation interaction with precipitates in a Nimonic alloy. Thus the measured friction stress takes the meaning of an internal resistance term. McLean[32] used the term friction stress to interpret the resistance to dislocation glide, which was controlled by the growth of the three dimensional dislocation network. Therefore, it is unclear whether friction stress is a measure of internal stress or internal resistance. The existence of a period of zero creep after a sudden stress reduction during a creep test, which is the basis of the friction stress concept, has been questioned by Gibeling and Nix[103].

The term residual stress is used to describe those stresses that exist in the material

in the absence of externally applied stresses. The classification of the residual stresses, i.e. Type I, Type II and Type III, is generally based on the length-scale over which they vary[104, 105]. Type I (macro-) residual stress varies continuously over a length-scale, which is comparable to the macroscopic dimension of a component. Type II (meso-) residual stress self-equilibrates over the length-scale of grains. As a consequence it is recognised that Type II residual stress is related to heterogeneity in polycrystalline materials at the grain and sub-grain length-scale. The grain-to-grain misfit stress is created by the orientation dependent elastic and plastic deformation within a polycrystalline material[105-107]. Rao et al.[34, 108] attributed the presence of anelastic strain recovery in creep to Type II residual stress. Here, the residual stress clearly takes the meaning of an internal stress term. Type III (micro-) residual stress varies over a length-scale of dislocations[104, 105, 109]. This type of residual stress arises from the stress fields of dislocations and discrete dislocation/dislocation interactions. In terms of the individual dislocations, it proves more convenient in the current context to include the effect of the rapidly changing (both spatially and temporally) residual stress in the definition of internal resistance as discussed in section 3.3.

After re-visiting different terms used for the so-called "internal stress" in creep, it is clear that there is confusion about the meaning of the internal stress and internal resistance. There is a need to consider different terms in the context of the dislocation structure associated with creep deformation mechanisms, i.e. internal stress and internal resistance. In the following two sections, we will consider their origins and the characteristics of the length-scales for these two terms.

3.2. Origins of internal stress

The length-scale of internal stress is similar to the definition of Type II and Type III residual stress[104, 105]. During deformation, different grain families deform to different levels, due to the elastic-plastic anisotropy of the grains. Both room temperature[106, 110] and high temperature tensile tests[107] have shown the presence of internal elastic strains at a grain-to-grain length-scale following unloading. These strains are representative of the internal residual stress state. Using a self-consistent model, Clausen et al.[106] predicted the magnitude of Type II internal stress in different grain families.

As described before, the presence of the heterogeneous dislocation sub-structure,

proposed initially by Mughrabi[37, 76], produces an inhomogeneous residual stress state, see σ_{is}^{ci} and σ_{is}^{cw} in Figure 6. The shear component of this type of internal stress is in the direction of flow within cell walls and in the opposite direction in the cell interiors. This type of internal stress satisfies the self-equilibrium condition between the cell walls and cell interiors and between all the grains in a polycrystalline material. Since there is a potential for a measure of confusion when discussing Type II and Type III internal stresses we adopt the simple definition that includes sub-grains within Type II and individual dislocations together with their geometries within Type III. The dislocation sub-structure (sub-grain) induced internal stresses are often called as long-range internal stresses[37, 76]. In the current context, we define this type of internal stresses as a sub-class of Type II internal stress.

In a stress free material, dislocation links are straight. They bow in response to the shear stress acting on the glide plane, with the radius of curvature, R, proportional to the magnitude of that stress acting on the dislocation, τ_a, Figure 7 (a). Thus measurements of the radius of curvature of bowed dislocations can be used to determine the Type III internal stress. We consider this further in section 5.

3.3. Origins of internal resistance

The internal resistance of a material depends on the dislocation density and arrangement as well as the distribution of solute elements and particles/precipitates when present. This provides barriers to both dislocation glide and climb[1, 92]. The yield strength also depends on these features and can be used to provide a measure of the material internal resistance. This is consistent with the work undertaken in 2008 by Wilshire and Scharning[3], where the yield strength of the material has been used to analyse creep deformation data.

Many mechanisms have been proposed to describe the change in internal resistance associated with dislocation creep processes[32, 66, 77, 111, 112]. These involve a range of processes which lead to changes in dislocation density and arrangement as well as variations in the mode of dislocation interaction with obstacles. In a material that forms a three dimensional dislocation network, as illustrated in Figure 3, the nodes at the end of a dislocation link must be broken to allow a dislocation to glide. Thus the interaction energy associated with the formation of a node is a measure of the internal

resistance. Alternatively, we can view the internal resistance as the stress required to break a link from the dislocation network. For a regular repeating dislocation network, the critical resolved shear stress or the internal shear resistance, of the network is:

$$\tau_{ir} = \frac{\alpha G b}{\lambda} = \alpha G b \sqrt{\rho} \tag{2}$$

where τ_{ir} is the internal shear resistance, λ is the dislocation link length, G is the shear modulus, b is the length of the Burgers vector, α is a dimensionless constant describing the strength of the dislocation node and ρ is the dislocation density. The second part of this equation follows the classic Taylor strain hardening formula[27, 113]. Thus equation 2 implies that the dislocation link length and dislocation density are interchangeable. Both of them provide a measure of the average internal resistance of a material.

Lagneborg and Forsen[114] proposed that the internal resistance is determined by the longest dislocation link length, λ_{th}, that is immobile:

$$\tau_{ir} = \frac{\alpha G b}{\lambda_{th}} \tag{3}$$

Thus, the applied stress has to be larger than this critical value to initiate permanent deformation. In this analysis, the dislocation structure is assumed to be the only source of the internal resistance. This is likely to be the case for pure metals. However, the presence of the other sources, such as the solute elements and second-phase particles/precipitates, may affect the overall material internal resistance. Accordingly, equation 3 needs to be modified:

$$\tau_{ir} = \frac{\alpha G b}{\lambda_{th}} + \tau_0 \tag{4}$$

where τ_0 is the additional contribution to the internal resistance due to the presence of the other sources.

Although the curvature of a bowed dislocation is a measure of Type III internal stress, as described in section 3.2 and Figure 7 (a), the critical configuration is a measure of the maximum stress required before the dislocation becomes unstable, as shown schematically by step 4 in Figure 7 (b). Thus the maximum curvature of the

bowed dislocation is another manifestation of internal resistance[39, 115]. Figure 7 (b) shows a schematic diagram for the development of a Frank-Read source[39]. A new dislocation loop is generated after the dislocation becomes unstable, step 5 in Figure 7 (b). However, it is clear that the experimentally observed dislocation structure with a bowed-out structure provides only a value of Type III internal stress which should be below the internal resistance. This is because the observed bowed-out dislocation structure is an equilibrium state, rather than the stage that completes a new loop. After the development of the new loop, the dislocation link will be restored to its original length, step 6 in Figure 7 (b).

For material, which forms a cell or sub-grain structure, the internal resistance to initiate permanent deformation could be attributed to the dislocation configuration within the cell walls, cell interiors or a combination of these two. Cell walls containing a high dislocation density might be treated as another obstacle to the dislocation movement and therefore another source of internal resistance[37, 76]. Morris and Martin[58] claimed that the presence of a high value of internal stress is required in the sub-grain boundaries to ensure dislocation emission from the boundaries. This contributes to a permanent deformation.

3.4. Summary

It is now clear that the misfit strain creates internal stress, where a Type II internal stress varies over a length-scale comparable with the grain size and a sub-class of Type II internal stress reflects the difference of stress between the cell walls and cell interiors. They are revealed as genuine measures of internal stresses after the material is unloaded. In parallel, the density and structure of dislocations vary with creep deformation, leading to a change in the internal resistance of the material, as illustrated in Figures 5 (c) to (f). In addition, the presence of other obstacles to dislocation motion may modify the internal resistance, as demonstrated by the creep response of dispersion strengthened alloys. Here we emphasise the fundamental difference between these two terms: internal stress and internal resistance.

These two terms are readily understood by comparing the mechanical behaviour with respect to stress-strain diagrams for a bi-crystal. A schematic diagram is illustrated in Figure 8, where no strain hardening is considered for simplicity, i.e. perfectly plastic strain and creep strain. Creep is a time-dependent plasticity and we

describe the plastic strain and creep strain in a similar way in Figure 8. The different stress-strain behaviour in grain A and grain B within the bi-crystal is shown in Figure 8 (a), while the externally applied stress-strain macroscopic behaviour of the bi-crystal is illustrated in Figure 8 (b). When the bi-crystal, Figure 8 (c), is loaded under an applied stress, σ_a, grain B yields first, followed by the yielding of grain A. The preferential yield of grain B leads to a change in the slope of the macroscopic stress-strain curve, Figure 8 (b). The slope determined from the line XY in Figure 8 (b) is no longer a measure of the macroscopic elastic response of the bi-crystal due to the yield of grain B. Grain A still supports an increasing stress until it reaches yield, Figure 8 (a). The different yield points in each grain can be envisaged as a consequence of the different Schmid factors on the slip systems, as illustrated in Figure 8 (c). The indicated magnitudes of σ_{ir}^{A} and σ_{ir}^{B} in Figure 8 (a), reflect the internal resistance of grain A and grain B, respectively. On unloading, the bi-crystal responds elastically, Figure 8 (b). The slope of the macroscopic stress-strain curve is determined by the initial slope, i.e. line OX is parallel to line ZO' in Figure 8 (b). However, at the unloaded state (σ_a=0), internal stress remains in the grains, as illustrated by both the σ_{is}^{A} and σ_{is}^{B} in Figure 8 (a). Grain A is subjected to a tensile internal stress and grain B is subjected to a compressive internal stress.

If the bi-crystal given in Figure 8 contains a pre-existing internal stress in the grains, determination of the internal resistance becomes difficult without prior knowledge of the internal stress in each grain of the bi-crystal. For example, the external stress was applied to this bi-crystal from point O' in Figure 8 (b). As a consequence of the presence of a tensile internal stress in grain A and compressive internal stress in grain B after the first loading history, the applied stress required to create the preferential yield in the bi-crystal is then equal to the difference between the magnitude of σ_{ir}^{A} and σ_{is}^{A}. However, the genuine internal resistance for grains A and B never changes, i.e. σ_{ir}^{A} and σ_{ir}^{B}.

4. Creep Deformation Models

4.1. Introduction

In section 2 we described the material response within the framework of a power-law constitutive model for the creep deformation rate, equation 1. We now seek modifications to this relationship by taking into account the roles of internal stress and internal resistance as defined in section 3. We start by examining in more detail the recovery creep model proposed by Lagneborg[66] associated with the development of dislocation networks within a material. We then evaluate models for particle (dispersion) and solute strengthened materials which identify the roles of internal stress and internal resistance. Finally we consider the individual role of cell walls and cell interiors in steady state creep and transient creep when either a part or all of the applied stress is removed using the composite model described by Blum and his co-workers[72-75].

4.2. Recovery creep model

Recovery creep models are based on the observation that materials harden with strain and soften with time[1]. The formulations of recovery creep models proposed by McLean[116] and Lagneborg[66] consider the dislocations to be arranged in a three dimensional network. Based on detailed TEM examinations of dislocation link length distributions and the calculation of the fraction of mobile dislocations, Morris[65] provided a satisfactory interpretation of creep deformation in Type 316H stainless steel, tested at a temperature of 625°C and under stresses in the range from 200MPa to 395MPa. The creep rate was described as:

$$\dot{\varepsilon}_c \propto \int_{\alpha G b/\sigma_a}^{\infty} \frac{1}{\lambda}[\sigma_a - \sigma_{ir}(\lambda)]^{\frac{ab}{kT}} \theta(\lambda) d\lambda \qquad (5)$$

This equation was initially proposed by Lagneborg et al.[66, 114]. The value of ab/kT may be taken as approximately four and that of α close to one[65]. $\sigma_{ir}(\lambda)$ is the internal resistance associated with dislocation link length and σ_a is the applied stress. The internal resistance, $\sigma_{ir}(\lambda)$, is related to the length of a dislocation link through an

equation of the form described in equation 2. $\theta(\lambda)$ is the number density of dislocation links with a characteristic length, λ. The lower bound of the integration, $\alpha Gb/\sigma_a$, describes the separation of mobile and immobile dislocation links. The condition for a dislocation link to be mobile is $\lambda > \alpha Gb/\sigma_{ir}$. It is only when the applied stress, σ_a, exceeds the internal resistance, $\sigma_{ir}(\lambda)$, that a dislocation becomes mobile and contributes to strain accumulation[114]. Glide occurs when the nodes formed by dislocation links are broken.

The existence of an athermal component of the applied stress has been considered in Lagneborg's model[66]. When this athermal component originates entirely from the dislocation structure, the creep rate is then expressed by:

$$\dot{\varepsilon}_c = A[\exp(-\frac{Q}{kT})][\sigma_a - \sigma_{ir}(\lambda)]^{\frac{ab}{kT}} \tag{6}$$

where Q is the activation energy for creep, k is the Boltzmann constant, and T is the absolute temperature. A detailed description for the second part of this equation has been given in equation 5, where the dislocation interaction was implied to be the source of internal resistance. The presence of other sources, such as the solute elements and second-phase particles/precipitates can be considered by introducing an additional term τ_0, as described by equation 4.

4.3. Creep model for particle strengthened material

Generally the dependences of the steady state creep rate on applied stress and temperature for a material can be described by equation 1. The value of creep stress exponent n close to five or three has been observed experimentally, as illustrated in Figure 2 (a). However, a much higher stress exponent n has been obtained in particle strengthened materials within the intermediate levels of applied stresses, as shown in Figure 4. This is accompanied with the presence of a high value of activation energy Q. Creep tests in a Nimonic alloy were undertaken by Williams and Wilshire[117]. Q=460kJ/mol and n=8.3 have been obtained by them. The nickel self-diffusion activation energy was reported to be 280kJ/mol[6] and the activation energy for creep was much higher than this self-diffusion activation energy. Williams and Wilshire[117]

proposed that the high values of Q and n could be accounted for in terms of the stress and temperature dependences of the internal resistance. The steady state creep rate, $\dot{\varepsilon}_c$, was then described as:

$$\dot{\varepsilon}_c = A(\sigma_a - \sigma_{ir})^4 \exp\left(\frac{-Q^*}{kT}\right) \tag{7}$$

where σ_a is the applied stress, σ_{ir} is the internal resistance, and n=4 is the creep stress exponent. By plotting the experimentally obtained creep strain rate against the different temperatures at the same value of effective stress, $(\sigma_a - \sigma_{ir})$, the value of Q^* was obtained to be 305kJ/mol[117]. This is close to the self-diffusion activation energy for nickel, 280kJ/mol[6]. Thus it has been demonstrated that the incorporation of a certain value of internal resistance into the creep deformation model rationalises the creep activation energy and therefore provides a further step in developing a physically based creep model.

4.4. Viscous glide model for solid solution material

The creep rate due to dislocation glide has been described by Orowan[118]:

$$\dot{\varepsilon}_c = \frac{\rho b \nu}{M} \tag{8}$$

where ρ is the dislocation density, b is the length of the Burgers vector, M is the Taylor factor (which is 3 for a texture-free polycrystalline material) and ν is the dislocation glide velocity. Friedel[39] analysed the diffusion of pinning atoms assisted by the dislocation line tension, and obtained a detailed form of creep deformation law to describe dislocation glide:

$$\dot{\varepsilon}_c = \frac{2\rho D_i \sigma_a b^3}{kT} \tag{9}$$

where D_i is the diffusion coefficient of impurity atoms which pin the dislocations. This equation was applied successfully to a wide range of materials[18]. Equation 2 indicates that the stress dependence of the dislocation density is two ($\rho \propto \sigma_{ir}^2$). For plastic deformation at a relatively low temperature or creep deformation at a relatively

low stress, it has been accepted that $\sigma_{ir}=\sigma_a$[66, 119]. Thus equation 9 gives a creep stress exponent of n=3 for solid solution materials. However, the magnitude of σ_{ir} becomes smaller than σ_a with increasing temperatures[66], although σ_{ir} could be treated as being proportional to σ_a[26, 30].

4.5. Model for a heterogeneous dislocation sub-structure

In section 2.3, the effect of a heterogeneous dislocation sub-structure on creep deformation has been described, i.e. the rectangular cells with thin walls containing dense arrays of dislocations and the cell interiors containing a low density of dislocations[37, 76]. Furthermore, the development of a sub-class of Type II internal stresses associated with this dislocation structure has been discussed in section 3.2, see Figure 6. It is evident that both internal stress and internal resistance are associated with the heterogeneous dislocation sub-structure. The internal resistance associated with the dislocation density, dislocation link length as well as the distribution of solute elements and/or secondary-phase particles/precipitates when present have been discussed in section 3.3. A composite model which accounts for the mechanical interaction between the cell walls and cell interiors has been developed by Blum and his co-workers [72, 74, 75]. In this model it is assumed that the cell walls and cell interiors experience the same total strain (elastic plus inelastic). In their original model they also consider the contribution to the total inelastic strain arising from migration of the cell walls. They acknowledge that this contribution is related to the deformation of the cell walls, but simply add it to the prediction of the composite model. The migration process results in a local incompatible strain and this should strictly be incorporated within the composite model, rather than simply added as an additional term. In this section we limit our discussion to the composite model, omitting any contribution from cell wall migration. The resulting description is consistent with the model described by Sedlacek and Blum [73].

The requirement of strain compatibility between the cell walls and cell interiors gives:

$$\varepsilon^t = \frac{\sigma_a}{E} + \varepsilon_{in} = \varepsilon^{ci} = \frac{\sigma_a + \sigma_{is}^{ci}}{E} + \varepsilon_{in}^{ci} = \varepsilon^{cw} = \frac{\sigma_a + \sigma_{is}^{cw}}{E} + \varepsilon_{in}^{cw} \qquad (10)$$

where ε^t is the total strain (which consists of both the elastic, σ_a / E, and inelastic, ε_{in} components), which is the same as that in the cell interiors, ε^{ci}, and cell walls, ε^{cw} (which also consist of elastic and inelastic components). The stresses σ_{is}^{ci} and σ_{is}^{cw} are the internal stresses in the cell interiors and cell walls respectively. The area fractions of cell interiors, f^{ci}, and cell walls, f^{cw}, are related through:

$$f^{ci} + f^{cw} = 1 \tag{11}$$

and equilibrium requires that:

$$\sigma_{is}^{ci} f^{ci} + \sigma_{is}^{cw} f^{cw} = 0 \tag{12}$$

Combining equations 10 to 12 gives the internal stresses in the cell interiors and cell walls:

$$\sigma_{is}^{ci} = E f^{cw} (\varepsilon_{in}^{cw} - \varepsilon_{in}^{ci}) \tag{13a}$$

$$\sigma_{is}^{cw} = E f^{ci} (\varepsilon_{in}^{ci} - \varepsilon_{in}^{cw}) \tag{13b}$$

The important term in these equations is $(\varepsilon_{pl}^{cw} - \varepsilon_{pl}^{ci})$, which describes the inelastic strain mismatch between the cell walls and cell interiors. The magnitude of the inelastic strain in the cell interiors is larger than that in the cell walls due to their lower yield or creep strength[37, 73, 76]. Thus following a period of tensile loading which results in macroscopic inelastic straining of the material, the internal stress in the cell interiors is compressive and that in the cell walls is tensile after unloading.

The inelastic strain rate and evolution of the internal stresses are obtained by differentiating equations 10 to 13 with respect to time:

$$\dot{\varepsilon}_{in} = \dot{\varepsilon}_{in}^{ci} + f^{cw} \left(\dot{\varepsilon}_{in}^{cw} - \dot{\varepsilon}_{in}^{ci} \right) + \dot{f}^{cw} \left(\varepsilon_{in}^{cw} - \varepsilon_{in}^{ci} \right) \tag{14a}$$

$$\dot{\sigma}_{is}^{ci} = E(\dot{\varepsilon}_{in} - \dot{\varepsilon}_{in}^{ci}) \tag{14b}$$

$$\dot{\sigma}_{is}^{cw} = E(\dot{\varepsilon}_{in} - \dot{\varepsilon}_{in}^{cw}) \tag{14c}$$

The inelastic strain rates in the cell walls and cell interiors can be expressed in

terms of the local stresses using constitutive models such as those described in section 4.2. The model is completed by providing an evolution law for the area fraction of cell walls, f^{cw}[72-75]. In the steady state $\dot{f}^{cw} = \dot{\sigma}_{is}^{ci} = \dot{\sigma}_{is}^{cw} = 0$ and equations 14b and 14c requires the creep rate to be the same in the cell interiors and cell walls. This is consistent with the experimental observation of Milička[96], who observed that the form of the stress dependences of the steady state creep rate in two distinct dislocation arrangements are the same.

When part or all of the applied stress is removed from the specimen in a transient creep experiment, the internal resistance associated with the density and arrangement of dislocations in the cell walls decreases more rapidly than in the cell interiors as a consequence of recovery, due to the higher local dislocation density. It is instructive to argue that the relative change of the internal resistance to the internal stress in the cell walls determines the transient creep behaviour.

5. Measurement of Internal Stress and Internal Resistance

5.1. Introduction

Different types of internal stresses have been described in section 3 with respect to their characteristic length-scales over which they vary. For example, a Type II internal stress arises from the mismatch between a grain and its neighbours. Thus the magnitude of the internal stress is determined by the relative strength and orientation of its neighbours. Measurement techniques sample a variety of length-scales, thus they may record different stress values. Internal resistance originates from the dislocation arrangement and dislocation density as well as the interaction with obstacles. The magnitude of the internal resistance could be measured from a single dislocation, a group of dislocations or even an overall mechanical response of the material, i.e. yield strength.

This section describes techniques available to measure internal stress and internal resistance. These are summarised in Figure 9, with their characteristic length-scales. These techniques can be classified as (i) dislocation; (ii) diffraction and (iii) mechanically based. Alternatively we simply consider them in the layout of direct and indirect methods for evaluating both the internal stress and internal resistance.

This is because the prime purpose is to use the measured values for the creep deformation models and improve the predictions of the models. Some of the techniques in Figure 9 have been applied only at room temperature, but there is a potential to extend these techniques to studies addressing higher temperatures. For example, Chen et al.[120] have demonstrated that it is possible to measure by neutron diffraction the creep relaxation of Type I residual stresses in a weldment when subject to a stress relief heat treatment. In this case measurements were made during the heating to 650°C, hold at temperatures, and the cooling cycle.

In section 5.2, the techniques classified as direct measurements of internal stress will be described, including radius of curvature of bowed dislocation (which is one type of dislocation geometry), convergent beam electron diffraction (CBED), electron backscattered diffraction (EBSD), synchrotron X-ray diffraction, and the conventional X-ray and neutron diffraction. The sampling volume of these techniques increases from the length-scale of dislocations to that of several grains, Figure 9. In section 5.3, the techniques that provide a direct measure of internal resistance will be described, including dislocation link length (which is another type of dislocation geometry) and the Bauschinger and permanent softening effect test. The former measures a characteristic dislocation length-scale and the latter measures the overall behaviour of a bulk material, Figure 9. In section 5.4, two indirect measurement techniques will be described (i) analysis of peak asymmetry in X-ray diffraction and (ii) stress reduction type tests. The former provides a measure of internal stress and the latter provides some measure of internal resistance, Figure 9. Indirect measurement techniques indicate that the interpretation of the measured result relies on specific dislocation based models. We cover both dislocation sub-structured materials and those exhibiting three dimensional dislocation networks.

5.2. Direct measurement of internal stress

5.2.1. Radius of curvature of bowed dislocation

Morris and Martin[36, 58] measured Type III internal stresses due to creep deformation in a Al-11 wt.% Zn alloy. Specimens were creep deformed at different stresses (from 6MPa to 17MPa) and temperatures (210°C and 250°C). Dislocation sub-grain structures were observed in these creep deformed specimens[36, 58]. The

radius of curvature of bowed dislocations in both the sub-grain interiors and sub-grain boundaries were measured by TEM. A freezing technique was used in an attempt to retain the curved dislocations in their loaded state[58]. This was achieved by rapidly quenching specimens from the test temperature under the applied stress to room temperature. The dislocations remained bowed and from their radius of curvature, R, Morris and Martin[36, 58] determined the effective shear stress (i.e. the local stress at loaded state), τ_e, acting on the dislocation:

$$\tau_e = \frac{Gb}{R}\left\{\frac{1}{16\pi} ln(\frac{\Lambda}{r_0})[5 - cos2\beta]\right\} \quad (15)$$

where G is the shear modulus, b is the length of the Burgers vector, Λ is the mean dislocation spacing, r_0 is the dislocation core radius, and β is the angle between the Burgers vector and the dislocation direction. The radius of curvature of bowed dislocations, R, were estimated by fitting TEM images of the dislocations to an ellipse[58]. From their analysis the effective stress, τ_e, was assumed to be a measure of the stress required to hold the radius of curvature of a bowed dislocation. The internal stress was then calculated by Morris and Martin[36, 58] through assuming $\tau_{is}=\tau_e-\tau_a$. The applied shear stress, τ_a, was obtained by multiplying the applied stress, σ_a, by the Schmid factor of 0.3[58]. It is important to clarify that the term effective shear stress used by Morris and Martin[36, 58] is a local stress at the loaded state. This should not be confused with the same term effective stress that has been used in the literature by Lagneborg et al.[1, 114] but indicating a thermal stress component which depends on temperature and strain rate. In addition, from the measurement of the radius of curvature of a bowed dislocation, the magnitude of the internal stress can be derived, but not the sign of that stress.

Using the approach adopted by Morris and Martin[36, 58], the internal shear stresses, $\tau_{is}=\tau_e-\tau_a$, acting on dislocations were measured at both sub-grain boundaries and sub-grain interiors, for creep tested specimens (250°C and 8MPa) interrupted at creep strains of 5%, 7%, 10%, 15%[58]. In this case, a steady state creep was achieved after 4% creep strain. Thus, these selected creep strain values are representative of steady state condition. The average sub-grain diameter was 30μm and several sub-grains were selected where between 50 and 100 dislocations were analysed for each. The normalised values of internal shear stress with respect to the applied shear stress (τ_{is}/τ_a)

are plotted against the distance from the sub-grain boundaries in Figure 10. The applied shear stress in these creep specimens was 2.4MPa (applied stress of 8MPa times the Schmid factor of 0.3). Figure 10 shows that the calculated internal shear stress is about nine times of the applied stress for 7% creep strain, when the measurement was undertaken at sub-grain boundaries. This value increases to sixteen times of the applied stress for a 10% creep strain and twenty-five times of the applied stress for 15% creep strain, as shown in Figure 10. In addition, a much lower internal shear stress exists at the sub-grain interiors. These values are in contrast to results obtained after 5% creep strain, where the internal shear stress at sub-grain boundaries is similar to that at sub-grain interiors, Figure 10. Thus, the high magnitude of Type III internal stress is associated with the dislocation sub-grain boundaries, which is consistent with the dislocation sub-structure model, as shown in Figure 6.

Morris[65] also measured the radius of curvature of bowed dislocations in crept Type 316H stainless steel (tested at 625°C and 230MPa). In this material there were no cell/sub-grain dislocation structures observed using TEM[65]. For each specimen examined by Morris[65], the internal stress acting on the dislocation was measured to be in the range of $0.25\tau_a$. The magnitude of Type III internal stress was estimated to be 58MPa, one quarter of the externally applied tensile stress of 230MPa. The absence of a sub-grain structure suggests that there is also a variation of the Type III internal stresses within material that contains a three dimensional dislocation network.

5.2.2. Convergent beam electron diffraction

Convergent beam electron diffraction (CBED) applied to foil specimens for TEM studies provides a measure of localised lattice parameters with high accuracy and high spatial resolution using high order Laue zone (HOLZ) lines[121]. Lattice parameters are usually evaluated from the best match of the experimental pattern with computer-simulated patterns based on a kinematical approach[122]. The CBED experimental data are available to measure the internal stresses in room temperature cyclically deformed polycrystalline Cu[123], creep deformed single crystal Al[124], Cu[125] and polycrystalline Cu[124], and severely room temperature deformed polycrystalline Al[126]. Most of these experiments were conducted to identify the changes in lattice parameters due to the presence of a dislocation sub-structure[126].

The CBED technique provides a measure of the stress field around a few

dislocations and consequently these can be classed as Type III internal stress. The sampled gauge volume is determined by the incident electron probe size. Different probe diameters have been used previously, such as 5nm by Maier et al.[123] and Straub et al.[127], 20nm by Alhajeri et al.[126], and 80nm by Kassner et al.[124, 125]. It has been shown that a group of dislocations may have a large value of internal stress when using a 5nm diameter probe size[123, 127], but a corresponding larger group using an 80nm diameter probe size may have a zero internal stress[124, 125]. As a consequence the variations in the measured results from zero to a significant value could be due to an inappropriate selection of electron probe size and reflect the fact that stresses vary rapidly in the vicinity of dislocations. Hence the results can be sensitive to the characteristic length-scale over which measurements are made. The internal stress field associated with dislocations under a 80nm length-scale could self-equilibrate, as claimed by Alhajeri et al.[126].

The internal stress associated with dislocation cell structures, generated by room temperature cyclic deformation in polycrystalline Cu, was examined by Maier et al.[123] using an electron probe diameter of 5nm. Measurements showed that dislocations at cell interiors had tensile internal stresses of ~60MPa when unloaded from the compressive part of the cycle. This magnitude of internal stress is equivalent to 40% of the saturation stress, $\sigma_{is}^{ci}/\sigma_s$ = -0.4, in cyclic deformation. The internal stress in the cell walls could not be measured using the CBED technique, because the dislocation density within cell walls was too high[123]. The HOLZ lines are broadened by the presence of high density of dislocations and this reduces the accuracy of the stress measurement[126]. However, based on stress equilibrium in a dislocation cell structure, Maier et al.[123] claimed that Type III internal stress in the cell walls would be high and compressive, that is of the same sign as the applied compressive stress.

Straub et al.[127] studied Type III internal stresses induced by the presence of the dislocation cell/sub-grain structures in creep of polycrystalline Cu, using a 5nm diameter electron probe. Compression creep tests at a constant normalised applied stress, $\sigma_a/G = 4.3\times10^{-3}$, in a temperature range from 25°C to 360°C were undertaken to generate the dislocation sub-structures. A tensile internal stress of 25MPa in the sub-grain interiors was obtained for a crept specimen under compression (300°C and 162MPa). But internal stress close to the sub-grain boundaries could not be measured due to the high dislocation density in that region[127]. Straub et al.[127] concluded that a

tensile internal stress was present in the sub-grain interiors for the specimens crept under compression. The gradient of internal stress in the sub-grain interiors was observed to be relatively small. Close to the sub-grain boundaries, large stress gradients would be expected.

The above discussion illustrates the difficulty in measuring stresses at the length-scale of a few nanometres and in interpreting how these stresses are likely to influence the macroscopic creep response. Stresses at this length-scale vary rapidly and the result is very sensitive to the sampled volume. From a constitutive modelling perspective, the most important measures of Type III internal stresses are the volume averaged stresses in the cell walls and cell interiors within a given family of grains. At this length-scale, the cell structure associated internal stresses is judged to be a sub-class of Type II internal stress.

5.2.3. Electron backscattered diffraction

Electron backscattered diffraction (EBSD) offers a technique to measure both Type II and a subclass of Type II internal strains/stresses in a polycrystalline material, as indicated by the sampled gauge length of EBSD in Figure 9. The grain orientation and sub-grain orientation can be also correlated with the measured strains/stresses[128]. Using this method, Type II internal stress in an austenitic stainless steel arising from room temperature plastic deformation (up to 10%) has been evaluated by Ojima et al.[128]. The measurements were performed before deformation (stress-free reference), during in-situ loading and after unloading. The stress-free reference points were selected in each grain before deformation. By comparing the EBSD pattern in a stressed region with that of stress-free reference, the shifts of the zone axis in the EBSD-Kikuchi patterns, caused by the elastic strains and lattice rotations, were measured through cross-correlation based pattern shift analysis[129]. The detailed description of how the shifts were converted to strain and rotation tensors has been given by Ojima et al.[128].

Figure 11 (a) shows a typical stress-strain curve together with the EBSD measurement points at both unloaded and loaded states. In terms of the measurement during in-situ loading, only four grains were selected, thus the conclusion based on this is judged to be not statistically convincing. In terms of the unloaded measurements, the specimen was loaded elastically to 239MPa and 284MPa and then

unloaded, as shown in Figure 11 (a). Stress measurements, along the tensile direction, were undertaken in nine grains, where five grains had a <100> orientation and the other four had a <110> orientation[128]. In a F.C.C. material, they are equivalent to measurements of {200} and {220} grain families. Many measurement points were selected in each grain. A percentage distribution of residual elastic strains at 0MPa, 239MPa (unloaded state) and 284MPa (unloaded state), were given in the original article by Ojima et al.[128]. To show the values of internal stresses using the EBSD technique, we have selected the maximum values in the percentage distribution of residual elastic strains for each unloaded condition. The diffraction elastic constants (E_{200}=149.8GPa and E_{220}=212.0GPa), reported by Clausen et al.[106], have been used to convert the strain to stress, i.e. the internal stress. The derived internal stresses for the {200} and {220} grain families are shown in Figure 11 (b). Grains 1 to 5 belong to the {200} grain family, where in general tensile internal stresses are present at the unloaded state. On the other hand, for the {220} grain family, including grains 6 to 9, both tensile and compressive internal stresses are present. The grain-to-grain variations can be explained in terms of Type II internal stresses. The magnitude of the stress on a grain is determined by the relative strengths and orientations of neighbouring grains. For a crystallographically texture-free material, the grains are orientated randomly and therefore each grain, which belongs to the same grain family, has different neighbouring grains. However, the measured values should be treated carefully, because their magnitudes are larger than expected, with the internal stresses ranging from -300MPa to 700MPa, see Figure 11 (b). It should be noted that local variations in chemical composition contribute to a change in the lattice parameter and therefore introduce a diffraction peak shift. In addition, the diffraction elastic constants for the specific grains in the material need to be established. Finally, the application of this technique at high temperature remains a challenge, due to the degradation of imaging quality when elevating the temperature for in-situ testing.

5.2.4. Synchrotron X-ray diffraction

The advanced photon source (APS) synchrotron provides an X-ray beam with a typical gauge length of 14μm, which is smaller than the grain size of many metals and alloys[130]. Figure 12 (a) shows schematically a typical set-up of the synchrotron X-ray diffraction in APS. A highly penetrating 52keV high flux, narrow energy spread and

divergence X-ray beam impinged on a test sample that is 300μm thick and made from polycrystalline Cu with a grain size of 36μm. The bulk polycrystalline specimen was subjected to a tensile stress at room temperature and the dynamic behaviour of individual, deeply embedded sub-grains was measured by Jakobsen et al.[130]. Two detectors were used to obtain diffraction patterns on the grain length-scale (detector A) and sub-grain length-scale (detector B) respectively, Figure 12 (a). The latter corresponds to an angular resolution of ~0.004° and is an order of magnitude better than that obtained by TEM[130].

Figure 12 (b) shows the intensity distribution parallel to the diffraction vector for selected peaks, which appeared in the intensity map projected onto the reciprocal space coordinate $\mathbf{q_y}$, as shown in Figure 12 (a). The entire mapped intensity is indicated in black and this represents the diffraction pattern from a few sub-grains within a {400} grain, at 3% strain. The centres of each peak, from several individual sub-grains within this {400} grain, are clearly separated, indicating the presence of different magnitudes of elastic strains, i.e. internal stresses, shown by diffraction peaks in red, blue and magenta in Figure 12 (b). The observed width of the individual peaks is close to the experimental resolution as measured with a standard powder[130]. This indicates that there are no dislocations in the sub-grain interiors. Jakobsen et al.[130] concluded that the contribution of the sub-grain structure to diffraction peak shape cannot be described by a shifted profile broadened by a substantial dislocation density based on the soft and hard region model proposed by Mughrabi[37]. This model was used to interpret the asymmetric peak profile by X-ray diffraction[35, 127], which will be described in section 5.4.1. The observed individual sharp peak profiles, shown in Figure 12 (b), indicate the presence of a sub-class of Type II internal stress associated with sub-grain interiors. Thus each individual sub-grain experiences a different value of internal stress[130]. Certainly the synchrotron X-ray work undertaken by Jakobsen et al.[130] demonstrates that a sub-class of Type II internal stress could be generated as a misfit from sub-grain to sub-grain.

A spatially resolved measurement of elastic strains within the cell interiors in a single crystal of Cu, deformed in tension and compression along the <001> axis have been undertaken using micro-beam diffraction, 0.5μm diameter, scanning monochromatic differential-aperture X-ray microscopy (DAXM) at the APS[131]. The compression specimen was a 10mm diameter and 20mm long cylinder, and the tension specimen had a 5mm square cross-section and was 10mm long. These

specimens were deformed at room temperature to a relatively large true stress of ~200MPa at a true strain of ~30%. The DAXM specimens were then extracted from the centre of prior deformed specimens. Figures 13 (a) and (b) show the spatially integrated diffraction peak profiles (red curves) and the individual diffraction peak positions corresponding to each dislocation cell (vertical blue lines). The spatially integrated diffraction peak profiles exhibit an asymmetric shape with a skewed distribution at high diffraction angles for compression, red curves in Figure 13 (a), and for tension skewed at low diffraction angles, red curves in Figure 13 (b). In the compressive deformed specimen, all twelve peaks in Figure 13 (a) representing each individual cell interior are shifted to the left in $\Delta q/q$ ($q=2\pi/d$, d is the lattice spacing). A smaller q indicates a larger lattice spacing d. In the tensile deformed specimen, all nine peaks are shifted to the right, larger q but smaller d spacing, Figure 13 (b). This is consistent with the description given in the Mughrabi soft and hard region model[37, 132].

The average elastic strains for the compression and tension specimens were measured by Levine et al.[131] to be 8.5×10^{-4} and 5.2×10^{-4}, respectively, with a standard deviation of ~1.0×10^{-4}. Converting these measured axial elastic strains to stresses using a diffraction elastic constant for the {006} plane of E_{006}=66.6GPa[133], the magnitude of a sub-class of Type II internal stresses associated with the cell interiors is calculated to be 56.6MPa in tension for the compressive deformed specimen and 34.6MPa in compression for the tensile deformed specimen. Thus, the observed peak shifts due to individual cell interiors, Figure 13 (a) and (b), provides a direct measure of a sub-class of Type II internal stress in the cell interiors. However, this observation is inconsistent with that reported by Jakobsen et al.[130], see Figure 12 (b), where the diffraction peaks from each sub-grain interior could contain both tensile and compressive internal stresses.

5.2.5. Conventional X-ray and neutron diffraction

Historically, the presence of Type II internal stress in polycrystalline materials after being subjected to plastic deformation at room temperature was confirmed by using conventional X-ray diffraction[134-137]. This diffraction technique is inherently selective in terms of the grain orientations, thus it can be used to provide the stress state (Type II internal stress) from each grain family provided that Bragg's law is satisfied[104].

The main drawback of using conventional X-ray diffraction is that only the internal stress in the near surface material (<50μm for Al) can be measured[104]. This problem has been solved by the development of the neutron diffraction technique, which offers a measure of the internal stress in the bulk material (200mm for Al). These two techniques sample many grains in a material.

Neutron diffraction techniques have been used to measure Type II internal stresses in austenitic stainless steels subjected to creep deformation by Rao et al.[34, 138]. The development of internal stresses was obtained from a group of creep specimens, interrupted at different creep times for a fixed applied stress of 180MPa and a temperature of 650°C[34]. Figure 14 shows the magnitude of Type II internal stresses in three grain families: {200}, {220} and {311}. Here the originally measured lattice strains have been converted into stresses using diffraction elastic constants for each crystallographic plane reported by Clausen et al.[106]. Since the magnitudes of the transverse strains were not reported in their study, the Poisson contraction cannot be considered. Figure 14 shows that the strain incompatibility between grain families increases with test duration and thereby creep strain accumulated. The {200} grain family changes to a tensile stress and reaches around 100MPa after 450h at 650°C, whereas {220} becomes compressive, with a magnitude of about 20MPa. In this case the internal stress is small in the {311} grain family after creep. The changes in the internal stresses for these three grain families are similar to those obtained from the room temperature and high temperature tensile tests[106, 139]. This indicates that the magnitude of the strain incompatibility is determined by the strength of a grain relative to its neighbours, i.e. the generation of internal stress is likely a strain-dependent process, rather than a time-dependent one.

5.3. Direct measurement of internal resistance

5.3.1. Dislocation link length

TEM examinations of prior crept 316H stainless steels were undertaken by Morris[65]. Thin foils were prepared from specimens crept to the steady state at 625°C and 250MPa. The dislocation link length, λ, was determined following:

$$\lambda = \frac{(LS)^{1/2}}{2} \tag{16}$$

where L is the measured projected link length under TEM, and S is the foil thickness. The value of the internal resistance based on the dislocation link length, λ, was not given in the original paper by Morris[65]. Using the longest dislocation link length, λ_{th}, of ~13×10^{-8}m from his work, the internal resistance based on equation 3 is calculated to be 115MPa. The shear modulus at 625°C was taken as 5.8×10^{10}N/m^2 and the length of the Burgers vector was taken as 2.58×10^{-10}m, suggested by Frost and Ashby[6]. Thus the magnitude of the internal resistance, determined from the dislocation link length, is about one half of the applied stress.

5.3.2. Bauschinger and permanent softening effect test

Orowan[140] proposed a strain hardening theory, considering the presence of internal stress and gave a possible explanation to the stress-strain relationship on stress reversal, as schematically shown in Figure 15. First, the material is plastically deformed along the OA curve in the forward direction. If the direction of the applied stress is reversed at some point after yielding, material is then deformed along the AB curve to C point. As shown in Figure 15, part of the strain hardening developed by the forward straining is lost. This can be seen more clearly if we compare the OAD curve and the BC' curve which is the reverse straining curve BC re-plotted. The transient softening of the material on stress reversal is called the Bauschinger effect, the horizontal hatched area in Figure 15. This phenomenon is manifested by the early yield of the material if the direction of straining is reversed after the initial yield[141]. The vertical hatched area in Figure 15 has been defined as permanent softening of the material, indicated by the stress σ_{sn}, which is equal to σ_f - σ_r at the same magnitude of absolute strain. Both σ_f and σ_r are measures of material internal resistance. Here σ_f is the flow stress obtained if a monotonically increasing stress is applied to the material along the forward direction, OAD in Figure 15. Thus, permanent softening can be measured at the same absolute strain and beyond the first few percent of reversed deformation. Orowan[140] considered the magnitude of the permanent softening, σ_{sn}, to be a measure of internal stress, reflecting the difference between the internal resistance to the forward deformation (σ_f) and reverse deformation (σ_r).

Wilson[136] attempted to validate the permanent softening concept by measuring the internal stress. The approach was applied to several alloys with a cubic crystal structure. Several torsion specimens were prepared from a given material: each was pre-strained at room temperature to 9% and then subjected to one of a series of reverse strains in the range from 0% to 10%[136], as illustrated schematically in Figure 16 (a). The magnitude of permanent softening, τ_{sn}, was evaluated by the difference between the flow stress in the forward direction, τ_f, and the flow stress in the reversed direction, τ_r. The specimen subject to a 9% forward strain and then 0% reverse strain, i.e. in the unloaded condition after forward straining, was used for the internal stress measurement by conventional X-ray diffraction (described in section 5.2.5). This approach offers information about Type II internal stress.

Figure 16 (b) compares the permanent softening stress, τ_{sn}, with the X-ray diffraction measured Type II internal stress, τ_{is}, in several alloys considered by Wilson[136]. The selected alloys can be divided into two groups: (i) alloys that are mainly a single phase, as indicated by the arrows in Figure 16 (b), and (ii) dispersion hardened alloys. The magnitude of the measured internal stress in two alloys that are mainly a single phase is similar to the magnitude of the permanent softening stress, see the arrows in Figure 16 (b). However, for the dispersion hardened alloys, the internal stress is only half the magnitude of the permanent softening stress, Figure 16 (b). It was concluded by Wilson[136] that the lower values of the measured internal stress, τ_{is}, were due to stress relaxation arising from both the unloading procedure and sample preparation. The latter was supposed to introduce a stress change in a ~10μm thick layer close to the free surface used for X-ray measurement. However, whether this large difference can be attributed solely to these two reasons is doubtful. X-ray diffraction provides a measure of Type II internal stress, whereas the value of permanent softening stress τ_{sn} is a measure of the difference between the forward and reverse internal resistances.

5.4. Indirect measurement of internal stress and internal resistance

5.4.1. Analysis of peak asymmetry in X-ray diffraction

Theoretical and experimental studies of the broadening of X-ray diffraction peaks in deformed crystals have been well developed. Peak broadening provides a measure

of dislocation density which correlates well with TEM data[35]. Although this technique provides an indirect measurement of internal resistance, it has the advantage that it measures at the millimetre length-scale, Figure 9. As described in equation 2, the internal resistance can be derived from the measured dislocation density. In addition, the presence of high dislocation density at cell walls or sub-grain boundaries can be inferred from a detailed peak profile analysis[35, 127]. Profile analysis of broadened X-ray diffraction peaks in deformed crystals was based on the theory proposed by Wilkens[142], where both the density and arrangement of the dislocations were considered.

Many X-ray diffraction studies have demonstrated that the diffracted peaks in the deformed crystals can be broadened and become increasingly asymmetric with increasing deformation[35, 127, 132, 143, 144]. All the X-ray diffraction measurements were undertaken at the unloaded state. For example, single crystal Cu deformed by wire drawing at room temperature to strains reaching 0.26 and 0.92, showed the presence of a dislocation cell structure[143]. Figure 17 (a) shows the typical X-ray peak profiles obtained from the {002} crystallographic plane for two deformation values ε=0.26 and ε=0.92 together with the non-deformed state. The direction of the measured crystallographic plane was parallel to the applied stress. First, the full width at half maximum (FWHM) of the diffraction peak increases with the strain, ε. The FWHM of the diffraction peak for ε=0.26 is seven times and that for ε=0.92 is nine times greater than the FWHM of the undeformed material, Figure 17 (a). Second, the peak profiles obtained from the deformed condition are increasingly asymmetric, Figure 17 (a). Assuming that the cell walls and cell interiors scatter X-rays incoherently, the asymmetric diffraction peak profile can be decomposed into two symmetric sub-peaks, as shown in Figure 17 (b). One peak represents the cell walls and the other represents the cell interiors. The separation of sub-peaks was interpreted using the model proposed by Mughrabi[37]. This has been described in section 4.5. The integral intensities of each individual peak relative to the measured peak are proportional to the area fractions of the cell walls, f^{cw}, and cell interiors, f^{ci}, respectively. The peak positions of the deconvoluted peaks (two symmetric sub-peaks) are shifted in opposite directions and this was expressed by the relative change in the lattice spacing, $\Delta d/d$, for the $\{hkl\}$ crystallographic plane:

$$(\frac{\Delta d}{d})_x = -\Delta\theta_x \cot(\theta_0) \quad (17)$$

where $\Delta\theta_x$ is the shift of the two sub-peaks relative to the centre of gravity of the measured diffraction peak. θ_0 is the position of the measured diffraction peak. The letter *x* was used as a subscript to stand for either a cell wall or cell interior. Figure 17 (b) illustrates schematically the peak deconvolution, where the derived internal strains for cell interiors and cell walls can be converted to internal stresses, using the generalised Hooke's law and the diffraction elastic constants[143]. Both principal strain tensors, along the axial and radial directions of the specimen, were measured by Borbely et al.[143]. For the single crystal Cu, strained to ε=0.25 at room temperature and an applied stress of σ_a=60.1MPa, the magnitudes of internal stresses within cell walls and cell interiors were measured to be 107MPa and 46.1MPa, respectively[132]. The internal stress in the cell walls acts in the direction of the applied stress, whereas that in the cell interiors acts in the opposite direction.

The internal stress associated with the dislocation sub-structures in a polycrystalline Cu was measured using the same method by Straub et al.[127]. Compression creep tests were undertaken at different temperatures ranging from 25°C to 360°C and under a constant normalised stress, $\sigma_a/G=4.3\times10^{-3}$. Measurements showed that the increase in temperature had little effect on σ_{is}^{ci} (tensile internal stress at cell interiors) and σ_{is}^{cw} (compressive internal stress in the cell walls), Figure 18. For the applied stress of σ_a=-165MPa (compression), the measured internal stress in the cell walls was -59.2±18.4MPa (compression) and that in the cell interiors was 8.0±3.2MPa (tension). Also it has been demonstrated that the internal stress is almost independent of the strain accumulated over the creep tests[127]. This is inconsistent with the internal stress results obtained by measuring the radius of curvature of bowed dislocations under TEM[58], see Figure 10. This could be due to the different length-scales over which measurements were made by these two techniques. The radius of curvature of bowed dislocations when imaged using TEM provides a measure of Type III internal stress, whereas the analysis of peak asymmetry in X-ray diffraction provides a measure of a sub-class of Type II internal stress.

5.4.2. Stress reduction type tests

A variety of stress reduction type techniques have been developed in an attempt to measure the so-called "internal stress" in creep for different classes of materials, such as single crystal Al and Al-Mg alloys[26, 145], polycrystalline Al and Al-Mg alloys[26, 96], Al-Zn alloy[38], Ni based alloy[32], Fe-21Cr-32Ni[96] and Fe-21Cr-37Ni alloys[30], Fe-3% Si alloy[27], Type 304 austenitic stainless steel[146], and Type 316H austenitic stainless steel[111]. These techniques include the incremental unloading technique[145], constant structure stress reduction technique[146], stress/strain transient dip test technique[26] and a modified transient dip test technique[38]. It has been claimed by different groups of researchers[26, 30, 32] that these techniques provide an average value of "internal stress" over a significant number of grains in a bulk material, as indicated by the sampled gauge length in Figure 9. However these mechanical based techniques are now rarely used, because of the uncertainties in the measured values[19, 23, 147].

In general, stress reduction test techniques require that a certain proportion of the applied stress is removed during the creep test and the stress or strain transient is monitored instantaneously[23, 26, 147]. They are all based on an assumption that a constant dislocation structure is retained over the period of the rapid change in applied stress and the subsequent measurement. Thus, the measured values are a reflection of the microstructural condition at the moment before the stress reduction[26]. Another assumption is that the anelastic flow due to backward moving dislocations, driven by internal stress, exactly compensates for the continued forward moving dislocations, driven by the remnant applied stress. This leads to a zero net creep strain rate, $\dot{\varepsilon}_c = 0$, when the applied stress is reduced to a critical level, which is equal to the internal stress[147]. In this case, the measured stress takes a meaning of internal stress.

However, other investigators[30, 32] have questioned whether the stress reduction measurements could be interpreted by a recovery creep model (see section 4.2), where the duration of the time when $\dot{\varepsilon}_c = 0$ depends on the rate of creep recovery to allow further creep deformation. Such a change in dislocation structure would be an indication of the magnitude of internal resistance. Stress reduction type tests provide a measure of the internal resistance if we accept the recovery creep mechanism. This is supported by the rapid decrease in the magnitude of the measured value over the elapsed time after complete stress removal from the specimen, see Figure 19. Thus it

is unclear whether the measured values should be interpreted as an internal stress, internal resistance, or a combination of these two terms. In this review, we accept that stress reduction type tests provide some measure of internal resistance, because the measured value can be affected by the presence of internal stress. Thus application of the stress reduction type tests to materials that do not form a dislocation sub-structure provides a measure of internal resistance, if the formation of the dislocation sub-structure is the sole reason for the presence of internal stress.

The single stress relaxation test, shown in Figure 20 (a), offers a very simple approach to measure the internal resistance. However, stress relaxation to a subjectively judged limit value takes considerable time, leading to errors arising from the creep recovery during the measurement, i.e. the constant structure assumption is no longer valid[148]. This single stress relaxation test was replaced by the incremental unloading technique, shown in Figure 20 (b). In this case, the time required to reach the deformation limit, where no further stress relaxation occurs, is shortened by repeating the stress reduction in a series of unloading steps, Figure 20 (b). Early work by MacEwen et al.[145] attempted to use the incremental unloading technique to measure internal resistance. At various points in the tensile stress-strain curve, incremental unloading tests were undertaken on both single crystal Cu and single crystal Al-0.7% Mg alloy[145]. For single crystal Cu, a range of applied stresses from 1.2MPa to 22.9MPa were studied. The measured values were 0.8MPa for the former and 19.8MPa for the latter. Thus, the ratio of the measured internal resistance to the applied stress was between 0.7 and 0.9. In terms of the single crystal Al-Mg alloy, the measured internal resistance was about 90% of the applied stress.

Ahlquist and Nix[26] proposed a more widely accepted stress/strain transient dip test technique , which involves a series of unloading steps from an identical deformation state, see Figure 20 (c) for an illustration of the stress transient dip test. The stress or strain transient dip test technique measures either the stress change or the strain change after a reduction in applied stress[26]. The strain transient dip test technique was more often used to determine the internal resistance in creep deformed material, because this technique only required holding the stress constant. This can be easily achieved using conventional creep test machines[149]. Internal resistance measurements during steady state creep of Al and Al-Mg alloy were undertaken by Ahlquist and Nix[26]. Figure 21 shows the measurement results in polycrystalline Al, crept to steady state at 300°C and 350°C under a range of applied stresses from 2.8MPa to 10.4MPa.

At a constant applied stress, the internal resistance decreases with an increase in temperature, Figure 21. At constant temperature, the relative magnitude of internal resistance to applied stress decreases with an increase in applied stress, whereas the absolute internal resistance increases with applied stress. For the creep deformation at 300°C, internal resistances of 4.4MPa and 2.9MPa were obtained for the applied stresses of 10.4MPa and 3.4MPa, respectively.

Measurement of internal resistance during the primary creep stage was also attempted by Ahlquist and Nix[26]. However, this was unsuccessful due to large errors in the measured internal resistance. This was attributed to the rapid change in dislocation structures during the primary creep stage, so that the constant structure assumption was no longer valid[26]. A key factor to judge whether the measured internal resistance reflects the internal state of a creep deformed material before the stress disturbance is based on how quickly the measurement can be completed[23, 147, 150].

In addition, Blum and Finkel[38] claimed that the determination of the deformation limit from the zero strain rate, $\dot{\varepsilon}_c = 0$, after an immediate stress reduction is subjective. To overcome this, it has been attempted by them to measure the value of the reduced stress, where the subsequent anelastic strain starts to become negative, $\dot{\varepsilon}_c < 0$. Using this modified dip test technique, they have obtained a lower value of the internal resistance, $0.5\sigma_a$, in steady state creep of Al-11 wt.% Zn alloy for tests undertaken at 250°C and stresses ranging from 5.5MPa to 18.4MPa[38]. It was claimed that highly reproducible measurements can be obtained by using this method[38].

The measurement of internal resistance using a constant structure stress reduction technique was proposed by Cuddy[146] for specimens of Type 304 stainless steel subjected to different creep induced pre-strains, i.e. different internal states. Five specimens were creep strained to 15% at 247MPa and 704°C, followed by reducing the applied stress to five different stress levels: 222MPa, 200MPa, 169MPa, 147MPa and 124MPa. The immediate creep strain rates after the stress reduction were measured for five separate tests and then plotted against the corresponding reduced stress levels. Absolute values of internal resistance were evaluated by two indirect methods.

In the first method, creep strain rate was described as:

$$\dot{\varepsilon}_c \exp(\frac{Q}{kT}) = A\sigma_a^n \tag{18}$$

A and n values for the creep condition, strained to 15% at 247MPa and 704°C, were obtained from equation 18. If more than one set of creep pre-strain conditions were considered, the values of A and n for each condition were plotted against the pre-strain stress, σ_p. Five pre-strain conditions were created by Cuddy[146]. Extrapolating to σ_p=0 gave the values of A and n for this condition, σ_{ir}=0, i.e. σ_a=σ_{op}. σ_{ir} is the internal resistance and σ_{op} is the operative stress. Thus the creep strain rate based on σ_{op} was described as:

$$\dot{\varepsilon}_c \exp(\frac{Q}{kT}) = 1.6\times10^{-9}\sigma_{op}^{5.8} \tag{19}$$

In this case A=1.6×10^{-9} and n=5.8 were obtained by extrapolation as described above. Then for each creep pre-strain condition, the difference between the operative stress obtained by extrapolation and the applied stress at the same creep strain rate is a measure of the internal resistance, σ_{ir}.

In the second method proposed by Cuddy[146], the value of applied stress, σ_a, required to maintain a given strain rate after creep pre-straining was plotted against the creep pre-strain stress, σ_p. Extrapolating to σ_p=0, where σ_{ir}=0 and σ_a=σ_{op}, gave a unique value of σ_{op} necessary to maintain each creep rate. Values of σ_{ir} were then obtained from σ_{ir}=σ_a-σ_{op} at constant creep strain rate, $\dot{\varepsilon}_c$.

The values of internal resistance obtained from these two methods were in good agreement and a relation between the internal resistance and the creep pre-strain stress was obtained:

$$\sigma_{ir} = \sigma_p^{1.7} \tag{20}$$

The ratio of the internal resistance to the applied stress, σ_{ir}/σ_a was in the range 0.10 to 0.25. The internal resistance measured by this constant structure stress reduction technique proposed by Cuddy[146] was much smaller than those measured using strain transient dip test technique, shown in Figure 19 and Figure 21.

5.5. Comparison of measurement techniques

In general, the internal stress and internal resistance measurement techniques have their characteristic length-scales, determined by the sampled gauge length relative to the controlling microstructural features, ranging from dislocation, sub-grain, grain to bulk material, as illustrated in Figure 9. Typical results are summarised in Table 1 for internal stress and Table 2 for internal resistance. The measured values relative to the initial applied stress are used in Table 1 and Table 2. Thus, a positive sign for the relative value of the internal stress indicates that this stress has the same direction to the applied stress, and vice versa.

TEM measurement of the radius of curvature of bowed dislocations provides an evaluation of Type III internal stress associated with individual dislocation[36, 37, 58]. In the cell interiors that are composed of the three dimensional dislocation networks, a value of internal stress, τ_{is}^{ci}/τ_a = 1 to 4 was obtained from the Al-11 wt.% Zn alloy[58], while the internal stress of σ_{is}/σ_a = 0.25 was obtained in Type 316H stainless steel exhibiting the three dimensional dislocation networks[65]. In addition, a high value of internal stress in the cell walls, τ_{is}^{cw}/τ_a = 9 to 25, was obtained by Morris and Martin[58]. However, it is unclear whether the measured internal stress has a positive sign or negative sign relative to the applied stress. This is due to the limitation of the measurement technique, which has been described in section 5.2.1.

The high value of internal stress associated with a high dislocation density in the cell walls measured by TEM is inconsistent with the values derived from the analysis of peak asymmetry in X-ray diffraction. Analysis of peak asymmetry gave a value of $\sigma_{is}^{cw}/\sigma_a$ = +1.8 at cell walls of room temperature deformed single crystal Cu[132] and a value of $\sigma_{is}^{cw}/\sigma_a$ = +0.36 at cell walls of creep deformed single crystal Cu[127], Table 1. The positive sign indicates that the internal stress has the same direction to the applied stress. However, we cannot reach a conclusion about which technique provides a correct measure of Type III internal stress in the cell walls, because the TEM based method is a direct measurement technique whereas the analysis of peak asymmetry in X-ray diffraction relies on the soft and hard region model proposed by Mughrabi[37]. In addition, the analysis of X-ray diffraction peak asymmetry provides a measure of a sub-class of Type II internal stresses at the sub-grain length-scale, averaged over

many sub-grains and many grains, all with different orientations and neighbouring grain relations[35, 132]. Thus it is inappropriate to compare the internal stress measurement results from these two techniques.

CBED can provide a measure of Type III internal stress when a few dislocations are present in the cell interiors, but cannot measure directly the internal stress at cell walls or sub-grain boundaries which contain a high density of dislocations[123, 127]. A comparison between the results from the CBED technique and the analysis of peak asymmetry in X-ray diffraction shows a relatively good agreement, where the former gives a value of $\sigma_{is}^{ci}/\sigma_s$ = -0.15 and the latter gives a value of $\sigma_{is}^{ci}/\sigma_s$ = -0.05, Table 1. The negative sign indicates that the direction of the internal stress is opposite to the applied stress. The synchrotron X-ray diffraction technique has the advantage, in particular when using the micro-beam[130, 131], that it samples dynamically a volume with a sub-grain length-scale within a bulk sized material. A sub-class of Type II internal stress associated with the cell interiors was derived from the synchrotron X-ray micro-beam studies[130, 131], Table 1, where $\sigma_{is}^{ci}/\sigma_a$ = -0.28 for compressive pre-loading and $\sigma_{is}^{ci}/\sigma_a$ = -0.17 for tensile pre-loading, respectively. Here the internal stress is in the opposite direction to the applied stress. The change in lattice spacing, measured by both the X-ray diffraction[136] and neutron diffraction[34], can provide a direct measure of Type II internal stress over a length-scale comparable to the grains. Typical results by these two techniques are shown in Table 1. For such a large sized sample gauge volume, Figure 9, the internal stress associated with the dislocation sub-structure would not be measured.

In terms of the internal resistance, two direct methods are available: (i) measurement of dislocation link length by TEM and (ii) measurement of material flow stress macroscopically in the Bauschinger and permanent softening effect test. The measurement of dislocation link length gave σ_{ir}/σ_a=0.5, Table 2. This method has to assume that dislocation glide occurs by breaking the nodes formed by dislocation links. Measurement of material flow stress is feasible at room temperature. However the possibility of using this technique at high temperature has not been considered.

After reviewing many techniques within the stress reduction type tests, it is clear that these indirect methods provide some measure of internal resistance when used in conjunction with a model[26, 30, 38]. These macroscopic measurements of internal resistance give a value averaged over the bulk material. After several years of

modifications, the strain transient dip test technique could offer a reliable measure of the internal resistance in creep deformed material (σ_{ir}/σ_a=0.5 to 0.6 for Al-11 wt.% Zn)[38] see Table 2. However, it is not possible to establish whether the change of dislocation arrangement representative of internal resistance, or the existence of a sub-class of Type II internal stress, leads to a zero creep strain rate after the applied stress was reduced to a critical value. This concern has also been put forward by Okazaki et al[151]. It would be instructive to undertake some stress reduction type tests combined with diffraction techniques, such as neutron diffraction and synchrotron X-ray diffraction to separate these two contributions. This combined approach would provide further insights into both the separate contributions and any potential correlation between them.

Direct observation of dislocation geometry created by the prior creep deformation using TEM can provide a measure of the internal resistance. Both Type III internal stress and internal resistance can be measured using TEM, see Table 1 and Table 2. However the main deficiencies of TEM are related to the thin foil specimens[35], since the possibility of the loss and re-arrangement of dislocations during foil preparation and/or during observation is well-recognised. Two pinning dislocation techniques have been developed to retain the dislocation sub-structures in their loaded state for TEM examination. Pinning dislocations under load together with a quenching technique has been used by Morris and Martin[58]. Low temperature fast neutron irradiation has been used by Mughrabi[37] to pin dislocation sub-structures both after unloading and in the loaded state. Although success has been achieved using these two techniques, two fundamental limitations remain. First, TEM only images a small volume of material so that it becomes practically difficult to obtain a statistically representative measure of internal resistance. Second, the image overlap where high dislocation densities are present such as in cell walls or sub-grain boundaries makes the identification of individual dislocations difficult[35].

6. Concluding Comments

This review has highlighted the importance of (i) separating internal stress and internal resistance in creep; (ii) establishing a link between these two terms and the dislocation creep mechanisms; and (iii) providing confidence in the measurement of these two terms by either direct or indirect techniques. The underlying need is for

these two contributions to be incorporated into creep deformation models that improve the ability to predict overall creep life of components both at the stage of design and for the extension of the service life. A typical example of the latter is Type 316H austenitic stainless steel components used in AGR nuclear plant in the UK. To date several of these plants have operated for periods of more than 30 years. However, there is an expectation that it should be possible to extend the operating life by at least another five to seven years[152]. To achieve this it is important to be able to predict the remanent life with high confidence. This requires that unnecessary conservatisms are removed which are included in the present assessment methodology[153].

From the above review it is clear that both the internal stress and internal resistance are important when considering creep strain rate. There are several factors which may lead to the changes in both the internal stress and internal resistance. For service components this will be a combination of the initial microstructure of the material and the creep history over the service life. Type II internal stress has been shown to be a function of creep deformation time, i.e. creep strain, Figure 14, where the relative strengths of grain families determine the magnitude of the internal stress. The increase in Type III internal stress arising from the creep deformation is shown to be a function of the creep strain, Figure 10. The development of the dislocation sub-structure in creep deformed material, as described in Figure 5, leads to the presence of high values of both a sub-class of Type II and Type III internal stresses[147, 154].

Internal resistance originates mainly from three contributions: (i) dislocation to dislocation interaction, which is a function of both dislocation density and arrangement; (ii) dislocation interaction with solute elements; and (iii) dislocation interaction with second-phase particles/precipitates. This becomes an important issue for the Type 316H stainless steel components subjected to extended periods of high temperature service life. There will be progressive changes in the underlying microstructure of the material over the service life, such as the amount of second-phase precipitates with associated changes in the composition of the austenite matrix and changes in the density and arrangement of dislocations[94, 155, 156]. These changes arise from a complex interaction between the magnitude and state of the applied stress combined with thermal ageing. Figure 22 shows a schematic diagram highlighting the influence of different sources of the internal resistance on the creep rate, where three contributions to internal resistance are considered. They are indicative of the contributions (i), (ii) and (iii) described above. For each creep deformation

mechanism, there is an internal resistance represented by the critical stress required to effect deformation, see σ_{ir}^{1} , σ_{ir}^{2} and σ_{ir}^{3} in Figure 22. In region 1, creep deformation is controlled by mechanism 1. This mechanism is then replaced by mechanism 2 in region 2 with increase in the applied stress. Finally mechanism 3 controls the highest creep rate in region 3. Although we present these changes as a function of applied stress, they will be related also to temperature, or strain history over the total creep life of the material. It is essential to establish the roles of the progressive microstructural changes on both internal stress and internal resistance to allow improved creep life prediction using physically based models.

Finally, the creep strain rate, $\dot{\varepsilon}_c$, may be predicted by using a modified form of equation 6:

$$\dot{\varepsilon}_c = A[\exp(-\frac{Q}{kT})][\sigma_{is+a} - \sigma_{ir}]^{\frac{ab}{kT}} \tag{21}$$

where σ_{is+a} describes a sum of the internal stress, σ_{is}, and the applied stress, σ_a, in the material. σ_{ir} is the characteristic internal resistance which controls the creep deformation. Both σ_{is} and σ_{ir} have characteristic length-scales. If a creep rate at the grain length-scale is considered, then the stress σ_{is+a} describes a localised stress state within a grain at the loaded state. In this case, the internal stress, σ_{is}, represents the presence of Type II internal stress. Accordingly, the magnitude of internal resistance, σ_{ir}, represents an averaged value over many dislocations, rather than a single dislocation. Thus it is important to select an appropriate measurement technique to provide values for both the internal stress and internal resistance at the required characteristic length-scale as shown in Figure 9. The confidence in the prediction of creep rate is determined directly by the measured values. Also, in the constitutive model such as equation 21, the internal stress and internal resistance must be defined in a consistent manner. For example, in the model for a heterogeneous dislocation sub-structure[37, 72, 76], we could interpret σ_{is} and σ_{ir} as representing the internal stress and internal resistance either in the cell walls or cell interiors. Whichever description is chosen it should give rise to the same macroscopic creep response.

Acknowledgements

We are grateful for the financial support from EDF Energy. Bo Chen acknowledges with great gratitude the sustained support from his family members in China. Some of the ideas in this review were enlightened by the long term research collaboration with Dr Shu Yan Zhang at ISIS, UK. Peter Flewitt acknowledges Wolfson College, Oxford University, for facilitating this collaboration. David Smith was additionally supported by the Royal Academy of Engineering and Rolls Royce plc.

References

1. R. Lagneborg, *Int. Metall. Rev.*, 1972, **17**, 130-146.
2. K.L. Murty and I. Charit, *J. Nucl. Mater.*, 2008, **383**, 189-195.
3. B. Wilshire and P.J. Scharning, *Int. Mater. Rev.*, 2008, **53**, 91-104.
4. R.W. Evans and B. Wilshire: 'Creep of Metals and Alloys'; 1985, London, The Institute of Metals.
5. M.F. Ashby, *Acta Metall.*, 1972, **20**, 887-897.
6. H.J. Frost and M.F. Ashby: 'Deformation-mechanism Maps'; 1982, Exeter, Pergamon.
7. R.J. Fields, T. Weerasooriya, and M.F. Ashby, *Metall. Mater. Trans. A*, 1980, **11**, 333-347.
8. D.A. Miller and T.G. Langdon, *Metall. Trans. A*, 1979, **10**, 1635-1641.
9. F.R.N. Nabarro: 'Report of a conference on the strength of solids', 1948, The Physical Society.
10. C. Herring, *J. Appl. Phys.*, 1950, **21**, 437-445.
11. R.L. Coble, *J. Appl. Phys.*, 1963, **34**, 1679-1682.
12. M.E. Kassner: 'Fundamentals of Creep in Metals and Alloys'; 2009, Amsterdam, Elsevier.
13. O.D. Sherby and P.M. Burke, *Prog. Mater. Sci.*, 1968, **13**, 325-390.
14. S. Takeuchi and A.S. Argon, *Acta Metall.*, 1976, **24**, 883-889.
15. A. Orlova and J. Cadek, *Mater. Sci. Eng.*, 1986, **77**, 1-18.
16. M.E. Kassner and M.T. Perez-Prado, *Prog. Mater. Sci.*, 2000, **45**, 1-102.
17. J. Gittus: 'Creep, Viscoelasticity and Creep Fracture in Solids'; 1975, London, Applied Science Publisher.
18. S. Takeuchi and A.S. Argon, *J. Mater. Sci.*, 1976, **11**, 1542-1566.
19. W. Blum, *Mater. Sci. Eng. A*, 2001, **319**, 8-15.
20. F.A. Mohamed and T.G. Langdon, *Acta Metall.*, 1974, **22**, 779-788.
21. B.F. Dyson, *Mater. Sci. Tech.*, 2009, **25**, 213-220.
22. A. Ma, D. Dye, and R.C. Reed, *Acta Mater*, 2008, **56**, 1657-1670.
23. M. Biberger and J.C. Gibeling, *Acta Metall. Mater.*, 1995, **43**, 3247-3260.
24. N. Hansen and X. Huang, *Acta Mater*, 1998, **46**, 1827-1836.
25. B. Bay, N. Hansen, D.A. Hughes, and D. Kuhlmann-Wilsdorf, *Acta Metall. Mater.*, 1992, **40**, 205-219.
26. C.N. Ahlquist and W.D. Nix, *Acta Metall.*, 1971, **19**, 373-385.
27. A. Orlova, K. Milicka, and F. Dobes, *Mater. Sci. Eng. A*, 1995, **194**, 9-16.
28. V. Sklenicka, K. Kucharova, M. Svoboda, L. Kloc, J. Bursik, and A. Kroupa, *Mater. Charact.*, 2003, **51**, 35-48.
29. J.C. Gibeling and W.D. Nix, *Mater. Sci. Eng.*, 1980, **45**, 123-135.
30. J. Cadek, *Mater. Sci. Eng.*, 1987, **94**, 79-92.
31. J.D. Parker and B. Wilshire, *Metal Sci.*, 1978, **12**, 453-458.
32. M. McLean, *Proc. R. Soc. Lond. A*, 1980, **371**, 279-294.
33. I.G. Crossland, R.B. Jones, and G.W. Lewthwaite, *J. Phys. D: Appl. Phys.*, 1973, **6**, 1040-1046.
34. A. Rao, K.B. Chong, P.J. Bouchard, and M.E. Fitzpatrick, 'ASME Pressure Vessels and Piping Division Conference', Baltimore, 2011.
35. T. Ungar, H. Mughrabi, D. Ronnpagel, and M. Wilkens, *Acta Metall.*, 1984, **32**, 333-342.
36. M.A. Morris and J.L. Martin, *Acta Metall.*, 1984, **32**, 1609-1623.
37. H. Mughrabi, *Acta Metall.*, 1983, **31**, 1367-1379.
38. W. Blum and A. Finkel, *Acta Metall.*, 1982, **30**, 1705-1715.
39. J. Friedel: 'Dislocations'; 1964, London, Pergamon Press Ltd.
40. W.D. Nix and B. Ilschner: 'Strength of Metals and Alloys'; 1980, Oxford, Pergamon.
41. A.K. Mukherjee: 'Treatise on Materials Science and Technology'; 1975, New York, Academic Press.
42. M.E. Kassner, *Mater. Lett.*, 1984, **2**, 451-454.
43. W.R. Cannon and O.D. Sherby, *Metall. Trans.*, 1970, **1**, 1030-1032.
44. P.K. Chaudhury and F.A. Mohamed, *Metall. Mater. Trans. A*, 1987, **18**, 2105-2114.
45. D.G. Morris and D.R. Harries, *Metal Sci.*, 1978, **12**, 525-531.
46. M.E. Kassner, J.W. Elmer, and C.J. Echer, *Metall. Trans. A*, 1986, **17**, 2093-2097.
47. A.K. Mukherjee, J.E. Bird, and J.E. Dorn, *Trans. ASM*, 1969, **62**, 155-179.
48. A.M. Brown and M.F. Ashby, *Scripta Metall.*, 1980, **14**, 1297-1302.
49. F.A. Mohamed, S.A. Shei, and T.G. Langdon, *Acta Metall.*, 1975, **23**, 1443-1450.
50. P. Yavari and T.G. Langdon, *Acta Metall.*, 1982, **30**, 2181-2196.

51. A.H. Cottrell and M.A. Jaswon, *Proc. R. Soc. Lond. A*, 1949, **199**, 104-114.
52. J.C. Fisher, *Acta Metall.*, 1954, **2**, 9-10.
53. J. Weertman, *J. Appl. Phys.*, 1957, **28**, 1185-1189.
54. J. Weertman, *Trans. Met. Soc. AIME*, 1960, **218**, 207-218.
55. C.M. Young, S.L. Robinson, and O.D. Sherby, *Acta Metall.*, 1975, **23**, 633-639.
56. H. Mecking and Y. Estrin, *Scripta Metall.*, 1980, **14**, 815-819.
57. R.W. Logan, R.G. Castro, and A. K. Mukherjee, *Scripta Metall.*, 1983, **17**, 63-66.
58. M.A. Morris and J.L. Martin, *Acta Metall.*, 1984, **32**, 549-561.
59. J. Gil Sevillano, P. Van Houtte, and E. Aernoudt, *Prog. Mater. Sci.*, 1980, **25**, 69-134.
60. S.L. Robinson and O.D. Sherby, *Acta Metall.*, 1969, **17**, 109-125.
61. S.I. Hong and C. Laird, *Acta Metall. Mater.*, 1990, **38**, 1581-1594.
62. X.X. Yu and C.Y. Wang, *Acta Mater*, 2009, **57**, 5914-5920.
63. M.J. Whelan, P.B. Hirsch, R.W. Horne, and W. Bollmann, *Proc. Phys. Soc. London A*, 1957, **240**, 524-538.
64. A.S. Argon and W.C. Moffatt, *Acta Met.*, 1981, **29**, 293-299.
65. D.G. Morris, *Acta Metall.*, 1978, **26**, 1143-1151.
66. R. Lagneborg, *Metal Sci.*, 1972, **6**, 127-133.
67. W. Carrington, K.F. Hale, and D. McLean, *Proc. R. Soc. Lond. A*, 1960, **259**, 203-227.
68. B. Modeer and R. Lagneborg, *Jernkont. Ann.*, 1971, **155**, 363-367.
69. B.P. Kashyap, K. McTaggart, and K. Tangri, *Phil. Mag. A*, 1988, **57**, 97-114.
70. T. Suzuki and T. Imura, 'Bristol Conference', London, 1954, Phys. Soc.
71. O.D. Sherby, *Acta Metall.*, 1962, **10**, 135-147.
72. F. Dobes and W. Blum, *Phys. Stat. Sol. (a)*, 1994, **144**, 343-352.
73. R. Sedlacek and W. Blum, *Comp. Mat. Sci.*, 2002, **25**, 200-206.
74. S. Vogler and W. Blum, Proc 4th Int. Conf. Creep and Fracture of Engineering Materials and Structures, Eds B. Wilshire and R,W. Evans, The Institute of Metals, London, 1990, 65-79., 1990.
75. M. Meier and W. Blum, *Mater. Sci. Eng. A*, 1993, **164**, 290-294.
76. H. Mughrabi, *Mater. Sci. Eng.*, 1987, **85**, 15-31.
77. M. Pahutova, J. Cadek, and V. Cerny, *Mater. Sci. Eng.*, 1984, **62**, 33-40.
78. K.D. Challenger and J. Moteff, *Metall. Trans.*, 1973, **4**, 749-755.
79. M.J. Mills, J.C. Gibeling, and W.D. Nix, *Acta Metall.*, 1985, **33**, 1503-1514.
80. F.A. Mohamed, *Mater. Sci. Eng.*, 1983, **61**, 149-165.
81. H. Suzuki, *Sci. Rep. Res. Inst. Tohoku Univ. A*, 1952, **4**, 455-463.
82. P. Yavari, F.A. Mohamed, and T.G. Langdon, *Acta Metall.*, 1981, **29**, 1495-1507.
83. E. Arzt, G. Dehm, P. Gumbsch, O. Kraft, and D. Weiss, *Prog. Mater. Sci.*, 2001, **46**, 283-307.
84. E. Orowan, 'Symp. on Internal Stresses', London, 1947, Inst. Metals, 451-453.
85. R.W. Lund and W.D. Nix, *Acta Metall.*, 1976, **24**, 469-481.
86. M. McLean, *Acta Metall.*, 1985, **33**, 545-556.
87. R. Lagneborg, *Scripta Metall.*, 1973, **7**, 610-614.
88. B. Reppich, *Acta Mater*, 1997, **46**, 61-67.
89. J.H. Schroder and E. Arzt, *Scripta Metall.*, 1985, **19**, 1129-1134.
90. R. Behr, J. Mayer, and E. Arzt, *Scripta Mater.*, 1997, **36**, 341-345.
91. J. Cadek, H. Oikawa, and V. Sustek, *Mater. Sci. Eng. A*, 1995, **190**, 9-23.
92. A. Wasilkowska, M. Bartsch, U. Messerschmidt, R. Herzog, and A. Czyrska-Filemonowicz, *J. Mater. Process. Technol.*, 2003, **133**, 218-224.
93. H.J. Kestenbach, W. Krause, and T.L. da Silveira, *Acta Metall.*, 1978, **26**, 661-670.
94. B. Chen: 'Effects of Thermo-Mechanical History on Creep Damage in 316H Austenitic Stainless Steel', PhD thesis, University of Bristol, Bristol, 2011.
95. R.K. Bhargava, J. Moteff, and R.W. Swindeman, *Metall. Trans. A*, 1976, **7**, 879-884.
96. K. Milicka, *Acta Metall. Mater.*, 1993, **41**, 1163-1172.
97. G.M. Pharr and W.D. Nix, *Scripta Metall.*, 1976, **10**, 1007-1010.
98. R.S. Mishra, T.K. Nandy, and G.W. Greenwood, *Phil. Mag. A*, 1994, **69**, 1097-1109.
99. Y. Li and T.G. Langdon, *Scripta Mater.*, 1997, **36**, 1456-1460.
100. J.C. Gibeling and W.D. Nix, *Acta Metall.*, 1980, **28**, 1743-1752.
101. H. Burt, J.P. Dennison, and B. Wilshire, *Metal Sci.*, 1979, **13**, 295-300.
102. P.W. Davies, G. Nelmes, K.R. Williams, and B. Wilshire, *Metal Sci.*, 1973, **7**, 87-92.
103. J.C. Gibeling and W.D. Nix, *Metal Sci.*, 1977, **11**, 453-457.
104. P.J. Withers and H.K.D.H. Bhadeshia, *Mater. Sci. Tech.*, 2001, **17**, 355-365.
105. P.J. Withers and H.K.D.H. Bhadeshia, *Mater. Sci. Tech.*, 2001, **17**, 366-374.

106. B. Clausen, T. Lorentzen, and T. Leffers, *Acta Mater*, 1998, **46**, 3087-3098.
107. M.R. Daymond and P.J. Bouchard, *Metall. Mater. Trans. A*, 2006, **37**, 1863-1873.
108. A. Rao, P.J. Bouchard, S.M. Northover, and M.E. Fitzpatrick, *Acta Mater*, 2012, **60**, 6851-6861.
109. E. Macherauch, H. Wohlfahrt, and U. Wolfstieg, *HTM Härterei-Techn. Mitt.*, 1973, **28**, 201-211.
110. B. Clausen, T. Lorentzen, M.A.M. Bourke, and M.R. Daymond, *Mater. Sci. Eng. A*, 1999, **259**, 17-24.
111. M. Pahutova, K. Kucharova, J. Cadek, and V. Cerny, *Mater. Sci. Eng.*, 1984, **62**, 25-32.
112. D. Kuhlmann-Wilsdorf, *Phil. Mag. A*, 1999, **79**, 955-1008.
113. G. I. Taylor, *Proc. Roy. Soc.*, 1934, **145**, 362-387.
114. R. Lagneborg and B.H. Forsen, *Acta Metall.*, 1973, **21**, 781-790.
115. D. Hull and D.J. Bacon: 'Introduction to Dislocations'; 2001, Oxford, Butterworth-Heinemann.
116. D. McLean, *Rep. Prog. Phys.*, 1966, **29**, 1-33.
117. K.R. Williams and B. Wilshire, *Metal Sci.*, 1973, **7**, 176-179.
118. E. Orowan, *Proc. Phys. Soc.*, 1940, **52**, 8-22.
119. N. Furushiro, M. Toyoda, and S. Hori, *Acta Metall.*, 1988, **36**, 523-529.
120. B. Chen, A. Skouras, Y.Q. Wang, J.F. Kelleher, S.Y. Zhang, D.J. Smith, P.E.J. Flewitt, and M.J. Pavier, *Mater. Sci. Eng. A*, 2014, **59**, 374-383.
121. J.W. Steeds: 'Introduction to Analytical Electron Microscopy'; 1979, New York, Plenum Press.
122. P.A. Stadelmann, *Ultramicroscopy*, 1987, **21**, 131-146.
123. H.J. Maier, H. Renner, and H. Mughrabi, *Ultramicroscopy*, 1993, **51**, 136-145.
124. M.E. Kassner, M.T. Perez-Prado, M. Long, and K.S. Vecchio, *Metall. Mater. Trans. A*, 2002, **33**, 311-317.
125. M.E. Kassner, M.T. Perez-Prado, K.S. Vecchio, and M.A. Wall, *Acta Mater*, 2000, **48**, 4247-4254.
126. S.N. Alhajeri, A.G. Fox, and T.G. Langdon, *Acta Mater*, 2011, **59**, 7388-7395.
127. S. Straub, W. Blum, H.J. Maier, T. Ungar, A. Borbely, and H. Renner, *Acta Mater*, 1996, **44**, 4337-4350.
128. M. Ojima, Y. Adachi, S. Suzuki, and Y. Tomota, *Acta Mater*, 2011, **59**, 4177-4185.
129. A.M. Fincharm and G.R. Spedding, *Exp. Fluids*, 1997, **23**, 449-462.
130. B. Jakobsen, H. F. Poulsen, U. Lienert, J. Almer, S. D. Shastri, H. O. Sorensen, C. Gundlach, and W. Pantleon, *Science*, 2006, **312**, 889-892.
131. L. E. Levine, B. C. Larson, W. G. Yang, M. E. Kassner, J. Z. Tischler, M. A. Delos-Reyes, R. J. Fields, and W. J. Liu, *Nature Mater.*, 2006, **5**, 619-622.
132. H. Mughrabi, T. Ungar, W. Kienle, and M. Wilkens, *Phil. Mag. A*, 1986, **53**, 793-813.
133. H.M. Ledbetter and E.R. Naimon, *J. Phys. Chem. Ref. Data*, 1974, **3**, 897-935.
134. G.B. Greenough, *Nature*, 1947, **160**, 258.
135. W.A. Wood and N. Dewsnap, *Nature*, 1948, **161**, 682-683.
136. D.V. Wilson, *Acta Metall.*, 1965, **13**, 807-814.
137. D.V. Wilson and Y.A. Konnan, *Acta Metall.*, 1964, **12**, 617-628.
138. A. Rao: 'Creep and Anelastic Deformation in Austenitic Steels', PhD thesis, The Open University, Milton Keynes, 2010.
139. D. Dye, H.J. Stone, and R.C. Reed, *Acta Mater*, 2001, **49**, 1271-1283.
140. E. Orowan, Symp. Internal Stresses and Fatigue in Metals, Detroit and Warren, Michigan, 1958, Elsevier, 59-80.
141. N.E. Dowling: 'Mechanical Behaviour of Materials: Engineering Methods for Deformation, Fracture and Fatigue'; 1998, London, Prentice-Hall International (UK) Limited.
142. M. Wilkens, *Physica Status Solidi (a)*, 1970, **2**, 359-370.
143. A. Borbely, G. Hoffmann, E. Aernoudt, and T. Ungar, *Acta Mater*, 1997, **45**, 89-98.
144. T. Ungar, I. Groma, and M. Wilkens, *J. Appl. Cryst.*, 1989, **22**, 26-34.
145. S. R. MacEwen, O. A. Kupcis, and B. Ramaswami, *Scripta Metall.*, 1969, **3**, 441-448.
146. L. J. Cuddy, *Metall. Trans.*, 1969, **1**, 395-401.
147. J.C. Gibeling and W.D. Nix, *Acta Metall.*, 1981, **29**, 1769-1784.
148. A.A. Solomon, C.N. Ahlquist, and W.D. Nix, *Scripta Metall.*, 1970, **4**, 231-234.
149. E. N. da C. Andrade and B. Chalmers, *Proc. R. Soc. A*, 1932, **138**, 348-374.
150. K. Abe, H. Yoshinaga, and S. Morozumi, *Trans. JIM*, 1977, **18**, 479-487.
151. K. Okazaki, Y. Aono, and T. Kaneyuki, *Mater. Sci. Eng.*, 1978, **33**, 253-266.
152. EDF Energy. 'Announcement made as CEO Vincent de Rivaz opens visitor centre at Hinkley Point B', Dec 2012 [viewed; Available from: http://www.edfenergy.com/media-centre/press-

news/EDF-Energy-announces-seven-year-life-extension-to-Hinkley-Point-B-and-Hunterston-B-nuclear-power-stations.shtml.
153. R.A. Ainsworth, *Int. Mater. Rev.*, 2006, **51**, 107-126.
154. T. Hasegawa, Y. Ikeuchi, and S. Karashima, *Metal. Sci. J.*, 1972, **6**, 78-82.
155. L.P. Stoter, *J. Mater. Sci.*, 1981, **16**, 1039-1051.
156. J.C. Walmsley, M. Weyland, P. Spellward, R.J. Scowen, and B. Lee: 'Electron optical examination of ex-service AGR superheater outlet header material', TE/AGR/REP/0002/96 Issue 1, Magnox Electric, 1997.
157. H. Oikawa, K. Sugawara, and S. Karashima, *Mater. Trans. JIM*, 1978, **19**, 611-615.
158. T. Endo, T. Shimada, and T.G. Langdon, *Acta Metall.*, 1984, **32**, 1991-1999.
159. H. Oikawa, K. Honda, and S. Ito, *Mater. Sci. Eng.*, 1984, **64**, 237-245.

Tables

Table 1. Summary of some typical measurement results for the internal stress using the techniques shown in Figure 9. A specific sign is used for the ratio of the internal stress relative to the applied stress; a positive sign indicates that the internal stress has the same direction to the applied stress, and vice versa. [RT: room temperature]

Material	*Reference*	*Deformation History*	*Measurement Condition*	*Measurement Technique*	*Key observation*
Al-11 wt.% Zn	Morris and Martin[58]	Tensile creep	Unloaded	Radius of curvature of bowed dislocations, TEM	τ_{is}^{cw}/τ_a = 9 to 25 at cell walls, τ_{is}^{ci}/τ_a = 1 to 4 at cell interiors
Type 316 stainless steel	Morris[65]	Tensile creep	Unloaded		σ_{is}/σ_a = 0.25 for dislocation structure with a three dimensional network
Polycrystalline Cu	Maier et al.[123]	RT fatigue	Unloaded	CBED	$\sigma_{is}^{ci}/\sigma_s$ = -0.4 at cell interiors
Polycrystalline Cu	Straub et al.[127]	Compressive creep	Unloaded		$\sigma_{is}^{ci}/\sigma_a$ = -0.15 at cell interiors
Single crystal Cu	Mughrabi et al.[132]	RT tension	Unloaded	Analysis of peak asymmetry in X-ray diffraction	$\sigma_{is}^{cw}/\sigma_a$ = +1.8 at cell walls, $\sigma_{is}^{ci}/\sigma_a$ = -0.8 at cell interiors
Polycrystalline Cu	Straub et al.[127]	Compression creep	Unloaded		$\sigma_{is}^{cw}/\sigma_a$ = +0.36 at cell walls, $\sigma_{is}^{ci}/\sigma_a$ = -0.05 at cell interiors
Single crystal Cu	Levine et al.[131]	RT tensile and compressive deformation	Unloaded	Synchrotron X-ray diffraction	$\sigma_{is}^{ci}/\sigma_a$ = -0.28 for compression, $\sigma_{is}^{ci}/\sigma_a$ = -0.17 for tension
Steel, Brass, Al-Mg, and Al-Cu alloys	Wilson[136]	RT forward and reverse torsion test	Unloaded	X-ray diffraction	$\tau_{is}^{\{hkl\}}/\tau_a$ = 0.09 to 0.24
Type 316 stainless steel	Rao et al.[34]	Tensile creep	Unloaded	Neutron diffraction	$\sigma_{is}^{\{200\}}/\sigma_a$ = +0.56 and $\sigma_{is}^{\{220\}}/\sigma_a$ = -0.11

Table 2. Summary of some typical measurement results for the internal resistance using the techniques shown in Figure 9. [RT: room temperature; HT, high temperature]

Material	*Reference*	*Deformation History*	*Measurement Condition*	*Measurement Technique*	*Key observation*
Type 316 stainless steel	Morris[65]	Tensile creep	Unloaded	Dislocation link length, TEM	$\sigma_{ir}/\sigma_a = 0.5$ for dislocation structure with a three dimensional network
Steel, Brass, Al-Mg, and Al-Cu alloys	Wilson[136]	RT forward and reverse torsion test	Unloaded	Bauschinger and permanent softening effect	$\sigma_{ir}/\sigma_a = 1$
Single crystal Cu and Al-Mg alloy	MacEwen et al.[145]	Tensile HT deformation	Loaded	Incremental unloading	σ_{ir}/σ_a= 0.7 to 0.9 for Cu and σ_{ir}/σ_a= 0.9 Al-Mg alloy
Polycrystalline Al and Al-Mg	Ahlquist and Nix[26]	Tensile creep	Loaded	Strain/stress transient dip test	σ_{ir}/σ_a= 0.38 to 0.84 for Al σ_{ir}/σ_a= 0.4 to 0.7 for Al-Mg
Al-11 wt.% Zn	Blum and Finkel[38]	Tensile creep	Loaded	Modified transient dip test	σ_{ir}/σ_a= 0.5 to 0.6
Type 304 Stainless steel	Cuddy[146]	Tensile creep	Loaded	Constant structure stress reduction	σ_{ir}/σ_a= 0.1 to 0.25

Figure Captions

Figure 1 A deformation mechanism map for Type 316 austenitic stainless steel, with a typical grain size of 50μm[6].

Figure 2 The diffusion coefficient compensated steady state creep rate ($\dot{\varepsilon}_c kT/D_{sd}Gb$) versus the shear modulus compensated steady state stress (σ_a/G) for selected polycrystalline materials: (a) pure Al data are from Ref. [13], Al-2.2 at.% Mg are from Refs. [157, 158], Al-0.5 at.% Mg, Al-1.1% Mg and Al-3.3% Mg are from Ref. [159]; (b) Fe-21Cr-37Ni austenitic stainless steel data are from Ref. [30], Type 316H austenitic stainless steel data are from Refs. [45, 94].

Figure 3 Dislocation structure during creep of a 20% Cr-35% Ni stainless steel, tested at 700°C and 343MPa, showing the presence of dislocation node which has just broken at position A. (After Lagneborg[1, 66])

Figure 4 A schematic diagram of the creep rate as a function of stress in dispersion strengthened and dispersion free materials (After Arzt et al.[83])

Figure 5 A typical creep test curve for austenitic stainless steel at 550°C and 250MPa, together with the dislocation structures observed at different steps of high temperature tests: (a) and (b) five different steps of a creep test; (c) TEM micrograph[67] showing the dislocation structure produced during the loading step at high temperature (T=400°C and ε=2%); (d) TEM micrograph[1, 66] showing a three dimensional dislocation network in secondary steady state creep (T=700°C and σ_a=107MPa); (e) and (f) TEM micrographs[71] showing the dislocation cell structure (T=700°C, σ_a=300MPa, ε=23%) and sub-grain structure (T=750°C, σ_a=100MPa) in secondary steady state creep.

Figure 6 An illustration of the soft and hard regions of a dislocation sub-structure model with a representation of the local stress distribution across the cell where the cell wall has a finite width. Under an applied stress, σ_a, the cell wall has an internal stress, σ_{is+a}^{cw}, and the cell interior has an internal stress, σ_{is+a}^{ci}. If we define σ_a

with a positive sign, the internal stress in the cell wall σ_{is+a}^{cw} is positive and the magnitude of it is larger than σ_a, whereas the internal stress in the cell interior σ_{is+a}^{ci} is positive but with a smaller magnitude. After removing the applied stress, σ_a, the cell wall has a reduced positive internal stress, σ_{is}^{cw}, but the cell interior has an negative internal stress, σ_{is}^{ci}. (After Mughrabi[37] and Čadek[30])

Figure 7 Schematic diagrams of a dislocation link under an applied stress: (a) curvature of a dislocation with a link length of λ, under a shear stress, τ_a; (b) development of a Frank-Read source from the initial step 1 to the final step 6.

Figure 8 A simplified model illustrating the concept of internal stress and internal resistance in a bi-crystal, subject to an elastic, perfectly plastic and creep deformation, under applied stress, σ_a: (a) and (b) showing the stress-strain relationship in both individual grains and the whole bi-crystal; (c) showing the orientation of grain A and grain B, relative to the applied stress axis.

Figure 9 Schematic indicative of the internal stress/resistance measurement techniques covering a range of length-scales.

Figure 10 Distribution of the normalised internal shear stress (internal shear stress/applied shear stress) at sub-grain boundary and the change of its value with the distance from sub-grain boundary for different magnitudes of strains over the creep test. (Recalculated figure after Morris and Martin[58])

Figure 11 Internal stress derived from the EBSD measurements in room temperature tensile deformed austenitic stainless steel: (a) stress-strain curve and the measurement points, including both unloaded and loaded conditions (After Ojima et al.[128]); (b) derived internal stresses for the {200} and {220} grain families.

Figure 12 (a) schematic diagram of the experimental set-up. The real and reciprocal space coordinates (**x**, **y**, **z**) and ($\mathbf{q_x}$, $\mathbf{q_y}$ and $\mathbf{q_z}$) are defined together with diffraction angle of 2θ. The direction $\mathbf{q_y}$ (the radial direction) and ($\mathbf{q_x}$ and $\mathbf{q_z}$) are parallel and perpendicular, respectively, to the ideal reciprocal lattice vector for the

diffraction plane studied, represented by **G**. (b) the intensity distribution of some selected diffraction peaks appearing in the intensity map projected onto $\mathbf{q}_y$. The corresponding profile of the entire mapped intensity is indicated in black. (After Jakobsen et al.[130])

Figure 13 Comparison between the spatially integrated diffraction peak measured by conventional X-ray diffraction technique and spatially resolved measurements of peak position measured by scanning-monochromatic DAXM technique, for the deformed single crystal Cu: (a) compression specimen; (b) tension specimen. The red curves in both figures are spatially averaged axial {006} plane peak profiles obtained from conventional X-ray diffraction technique. The vertical blue lines show the corresponding diffraction peak centres from individual dislocation cell interiors, measured using scanning-monochromatic DAXM technique. (After Levine et al.[131])

Figure 14 Derived Type II internal stress development in the interrupted creep samples measured using neutron diffraction by Rao et al.[34].

Figure 15 Schematic diagram showing the typical behaviour of a plastic deformed metal on stress reversal. Symbols σ_y, σ_f and σ_r denote initial yield strength at forward straining, flow stress at forward straining and flow stress at reverse straining.

Figure 16 Relationship between the magnitude of permanent softening, τ_{sn}, measured from the difference between τ_f and τ_r, and the Type II internal stress, measured by X-ray diffraction: (a) a schematic diagram showing the definition of τ_f, τ_r and τ_{sn} in stress-strain curve together with the permanent softening strain, ε_n; (b) X-ray measurement data from Wilson's work[136].

Figure 17 (a) Typical X-ray diffraction peak profiles of the {002} crystallographic plane of single crystal Cu, for the two deformation values ε=0.26 and ε=0.92 together with the non-deformed state; (b) typical decomposition of an asymmetric diffraction peak into two symmetric sub-peaks. I_w and I_c represent the diffraction peaks from cell walls and cell interiors, respectively. $\Delta\theta_w$ and $\Delta\theta_c$ are the

shifts of the sub-peaks relative to the centre of gravity of the measured peak profile. (After Borbely et al.[143])

Figure 18 Internal stresses at cell walls (compressive stresses), cell interiors (tensile stresses) measured by the analysis of asymmetric peak profile obtained from X-ray diffraction, together with the applied stresses (compressive stresses), plotted as a function of the creep temperatures. (After Straub et al.[127])

Figure 19 Internal resistance and its change with the elapsed time from the instant unloading, measured by a stress reduction type technique in the transient creep state of Type 316H austenitic stainless steel. Internal resistance data were collected from [30].

Figure 20 Schematic representation of the various methods for measuring the internal resistance, σ_{ir}, by using stress reduction type techniques: (a) single stress relaxation, (b) incremental unloading and (c) stress transient dip test. Symbols r and u denote the moment for stress relaxation and unloading, respectively. Symbol t is time.

Figure 21 The ratio of the internal resistance to the applied stress in polycrystalline Al, measured by the strain transient dip test technique showing the temperature dependence and applied stress dependence of the internal resistance. (After Ahlquist and Nix[26])

Figure 22 A schematic diagram showing the influence of different sourced internal resistance on the creep strain rate, where σ_{ir}^{1} , σ_{ir}^{2} and σ_{ir}^{3} represent the individual critical stress required to operate a specific creep deformation mechanism.

Figure 1
Click here to download high resolution image

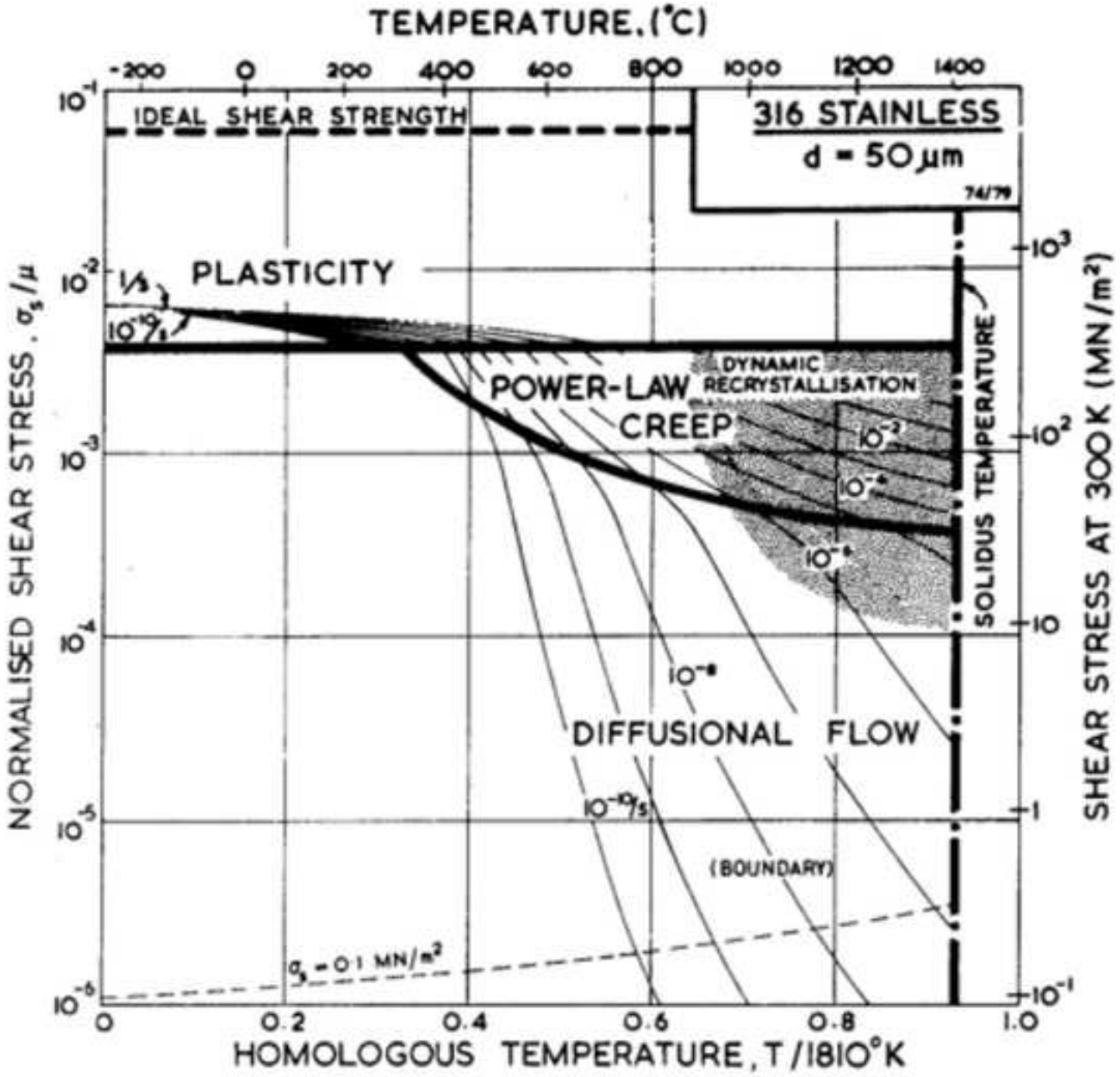

Figure 2
Click here to download high resolution image

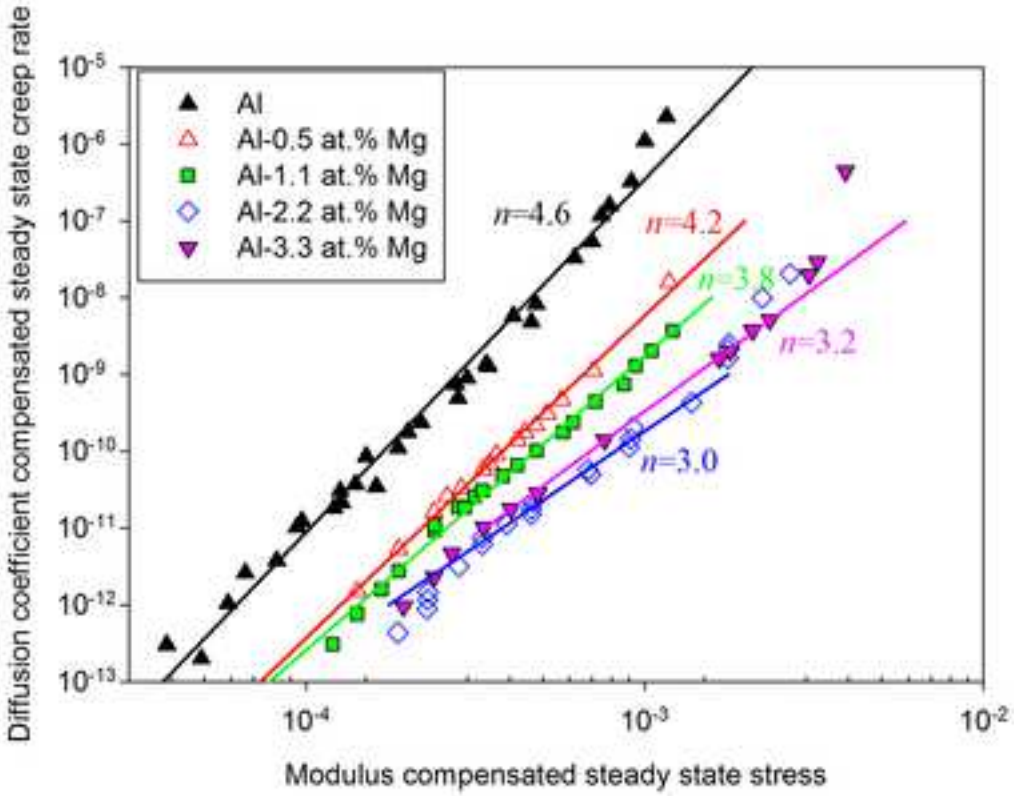

(a)

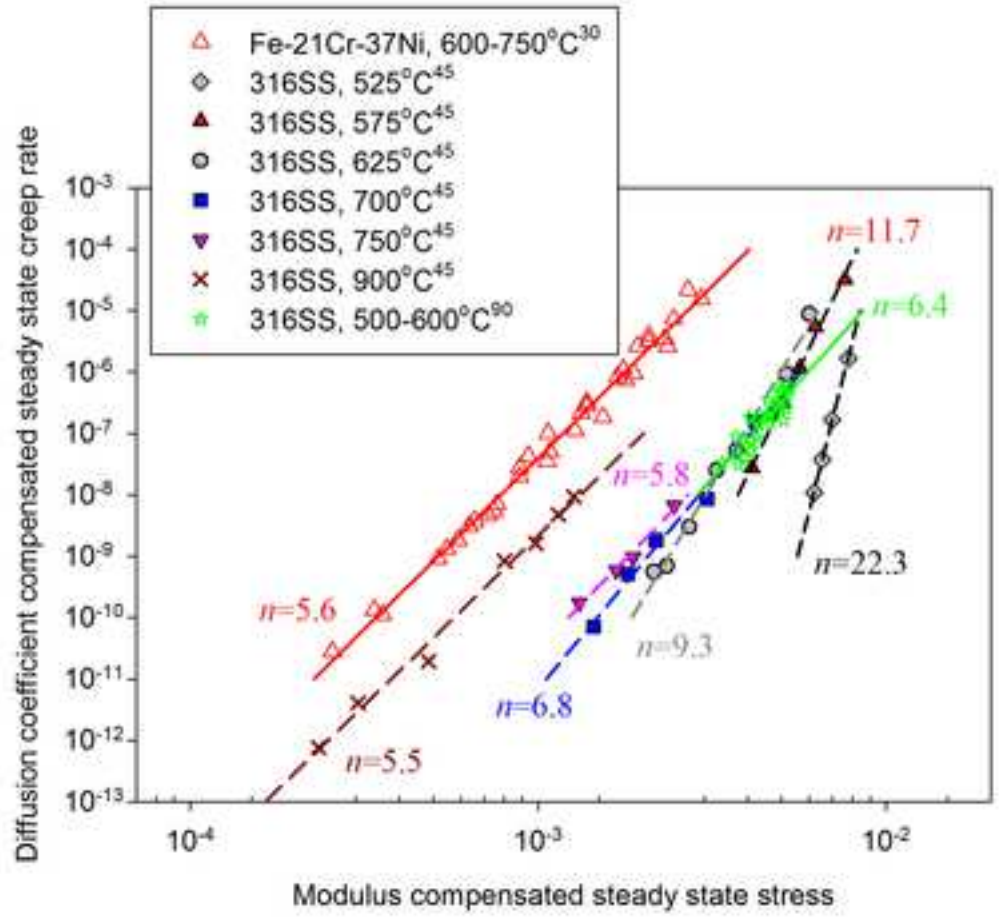

(b)

Figure 3
Click here to download high resolution image

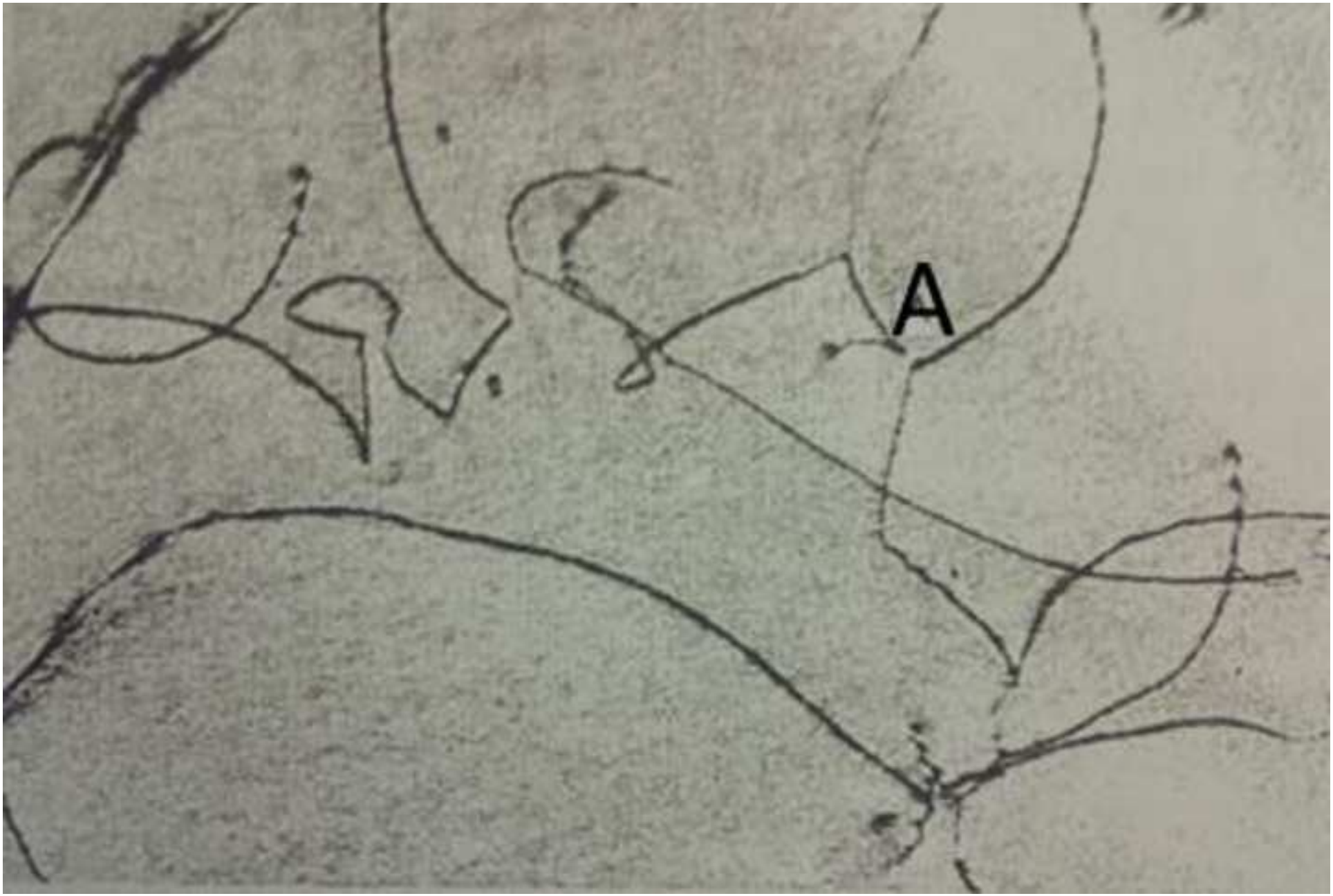

Figure 4
Click here to download high resolution image

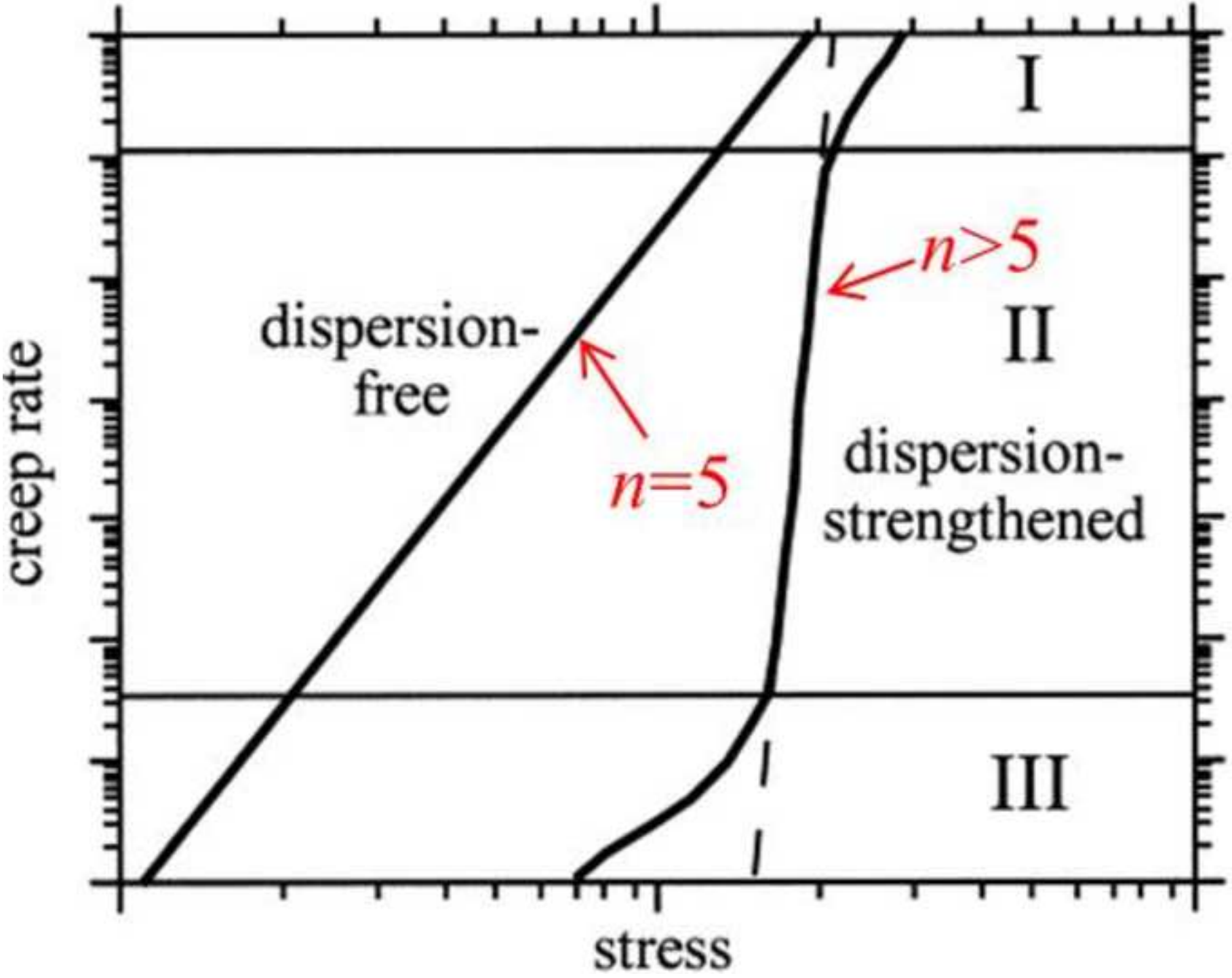

Figure 5
Click here to download high resolution image

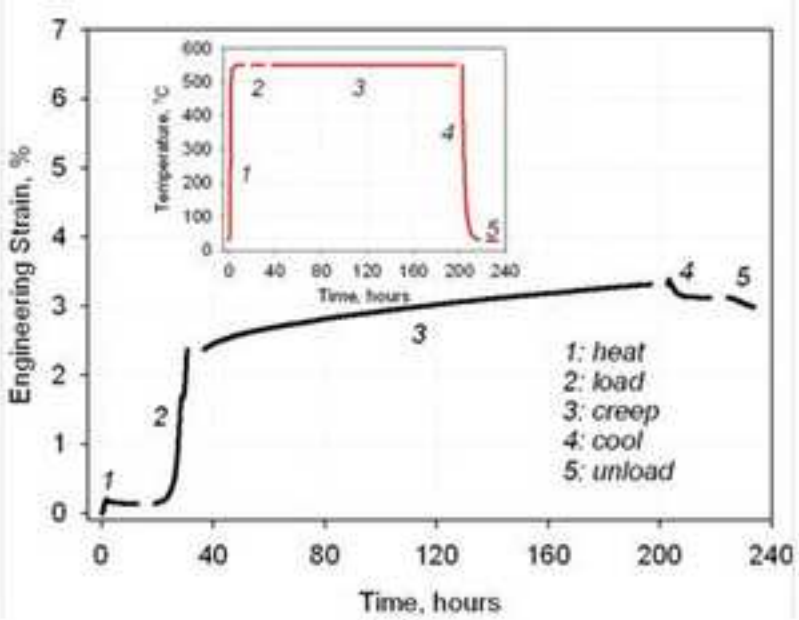

(a)

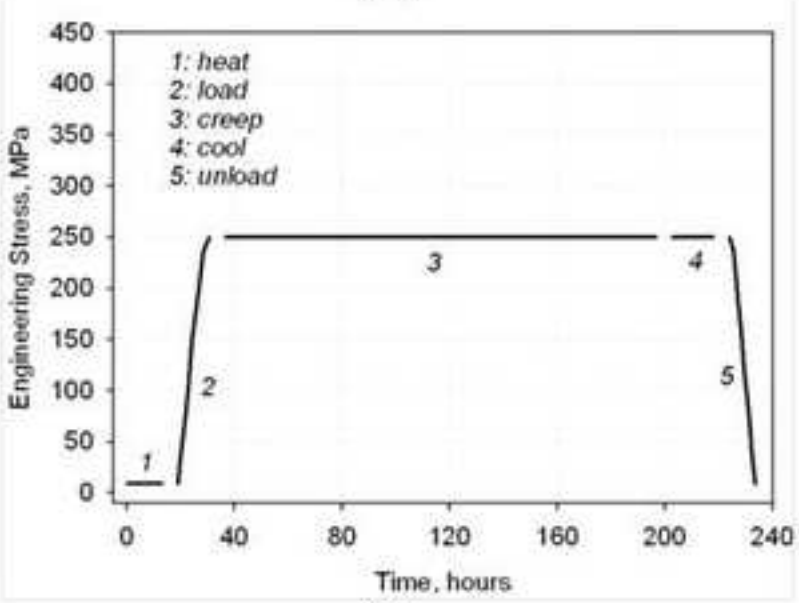

(b)

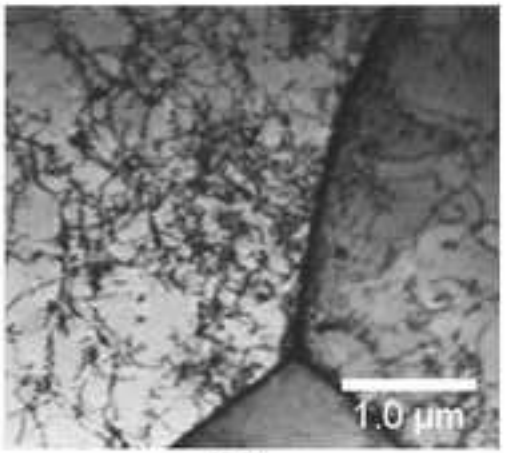

(c)

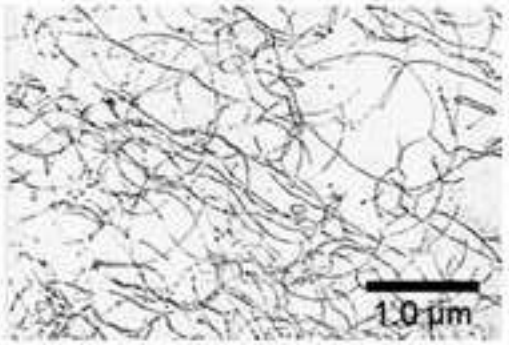

(d)

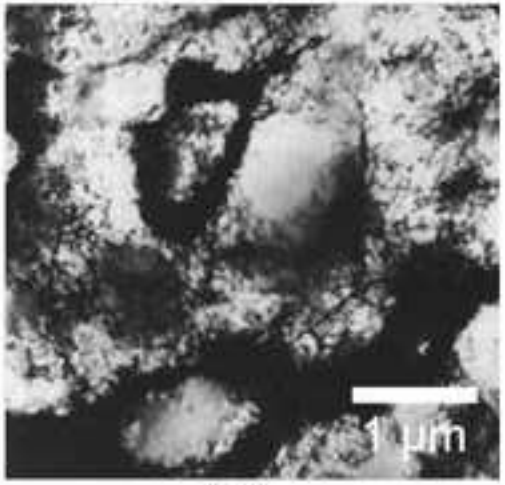

(e)

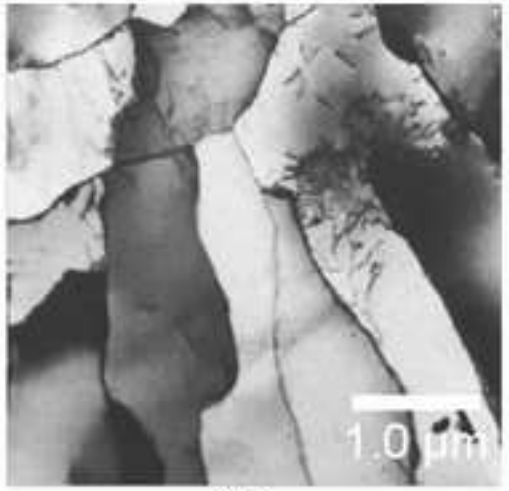

(f)

Figure 6
Click here to download high resolution image

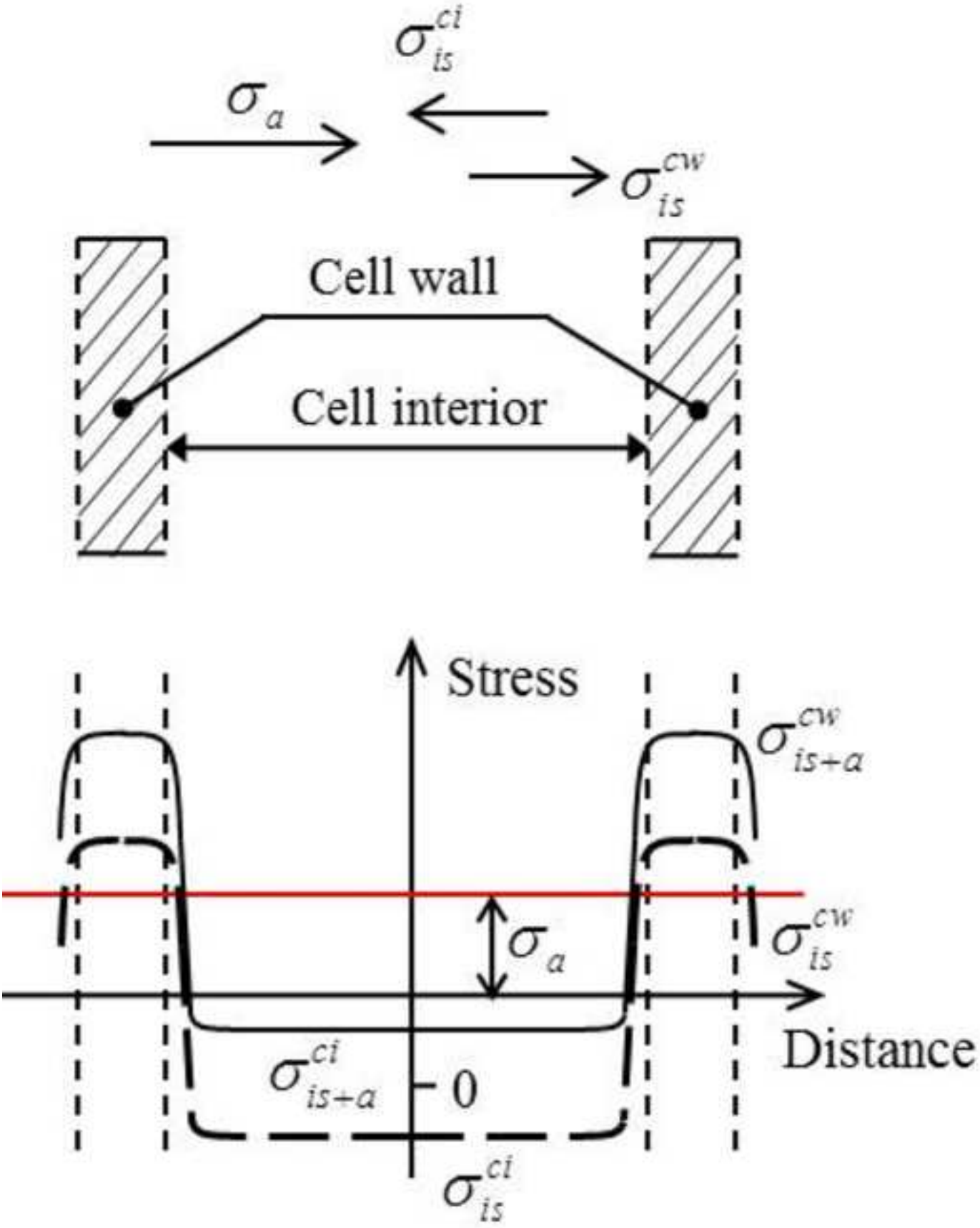

Figure 7
Click here to download high resolution image

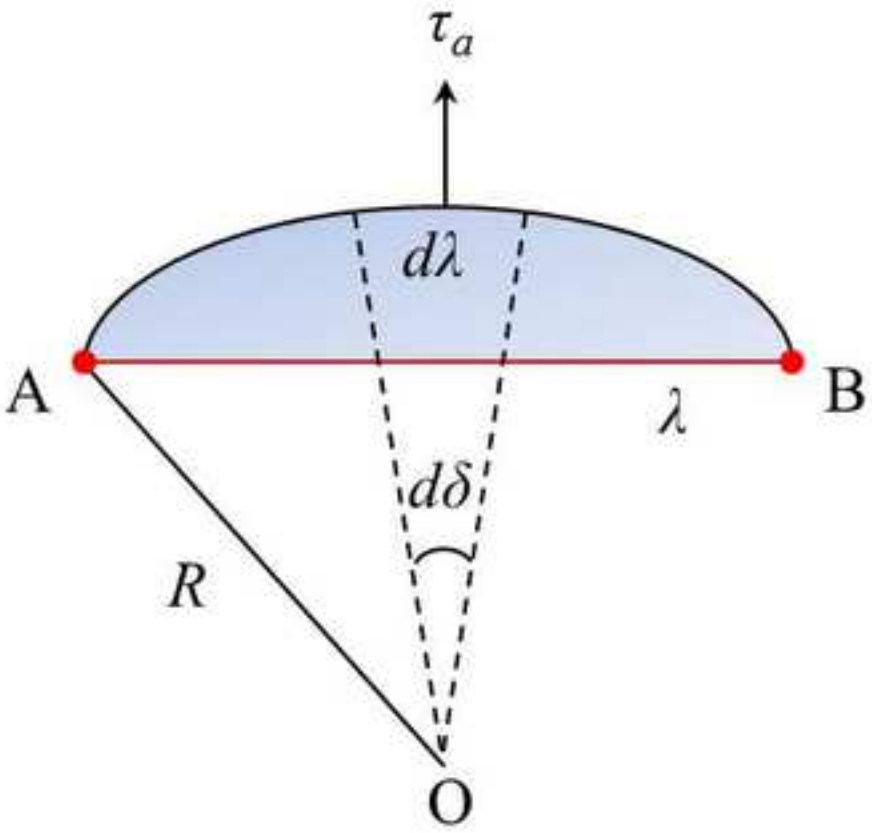

(a)

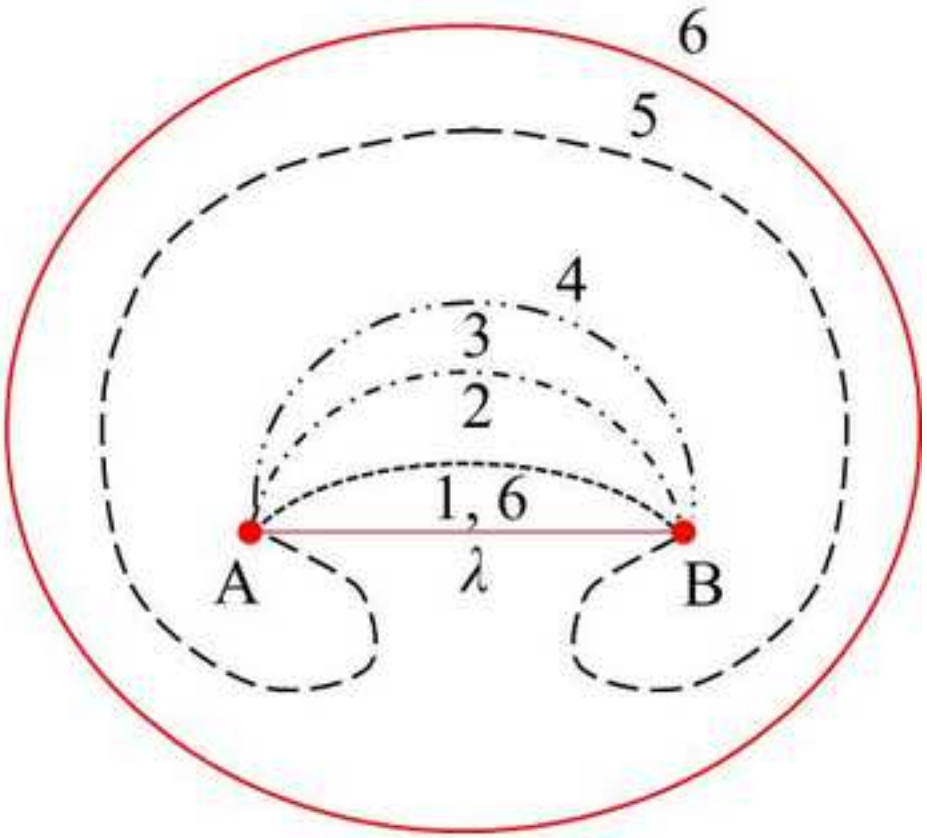

(b)

Figure 8
Click here to download high resolution image

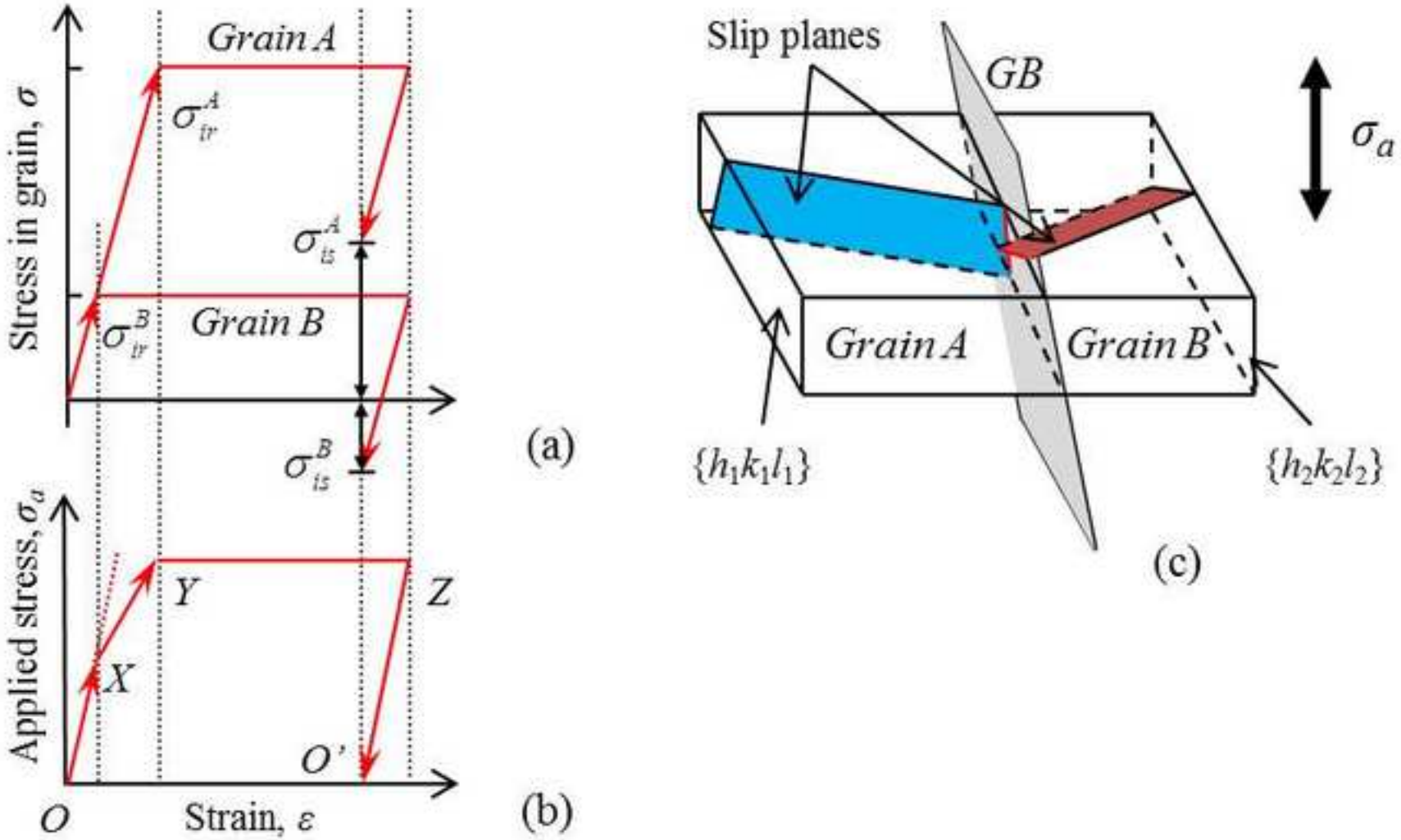

Figure 9
Click here to download high resolution image

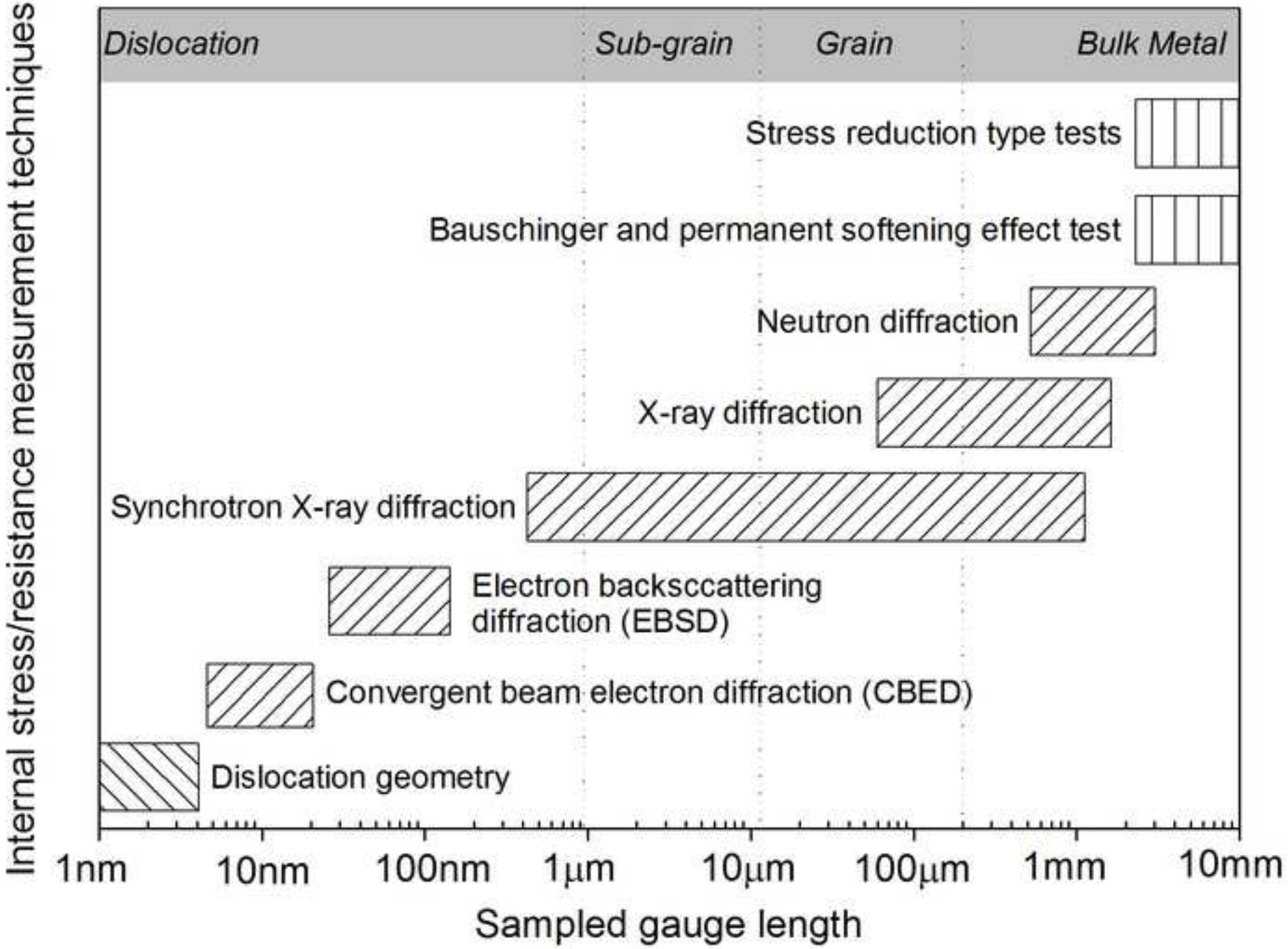

Figure 10
Click here to download high resolution image

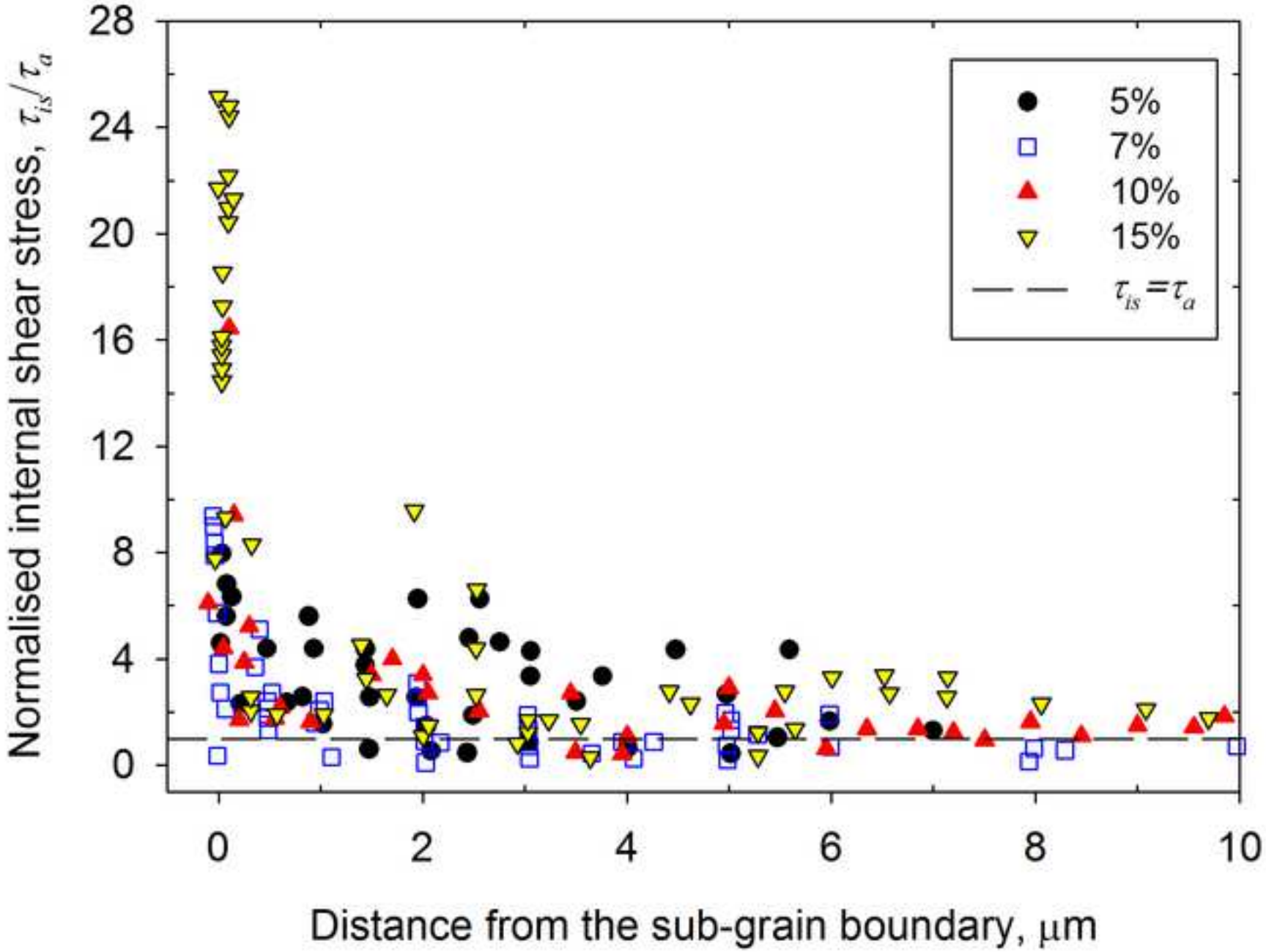

Figure 11
Click here to download high resolution image

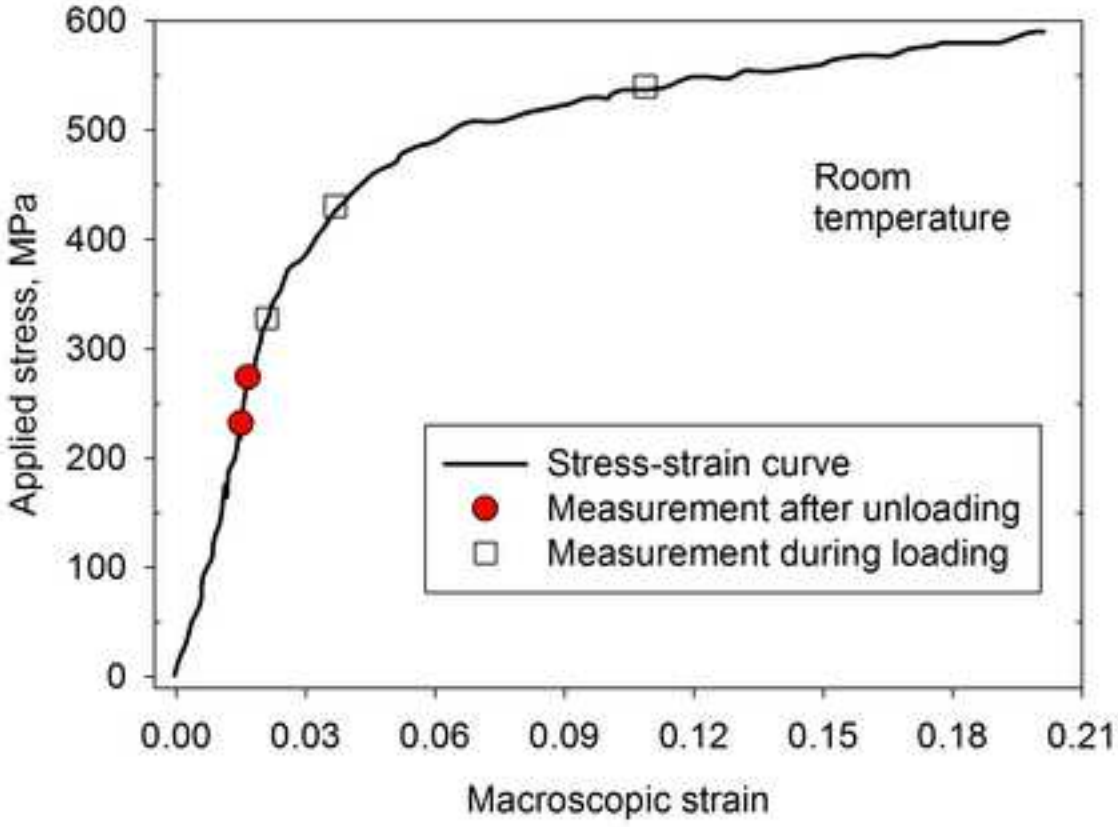

(a)

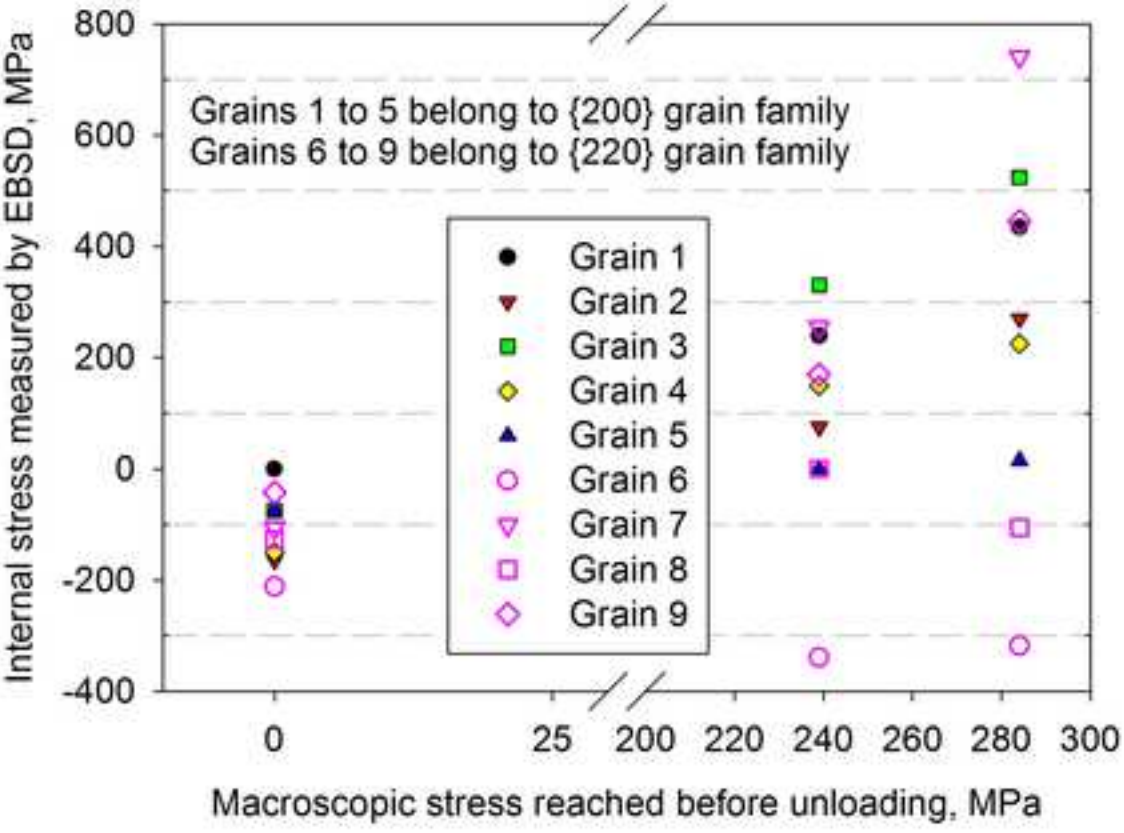

(b)

Figure 12
Click here to download high resolution image

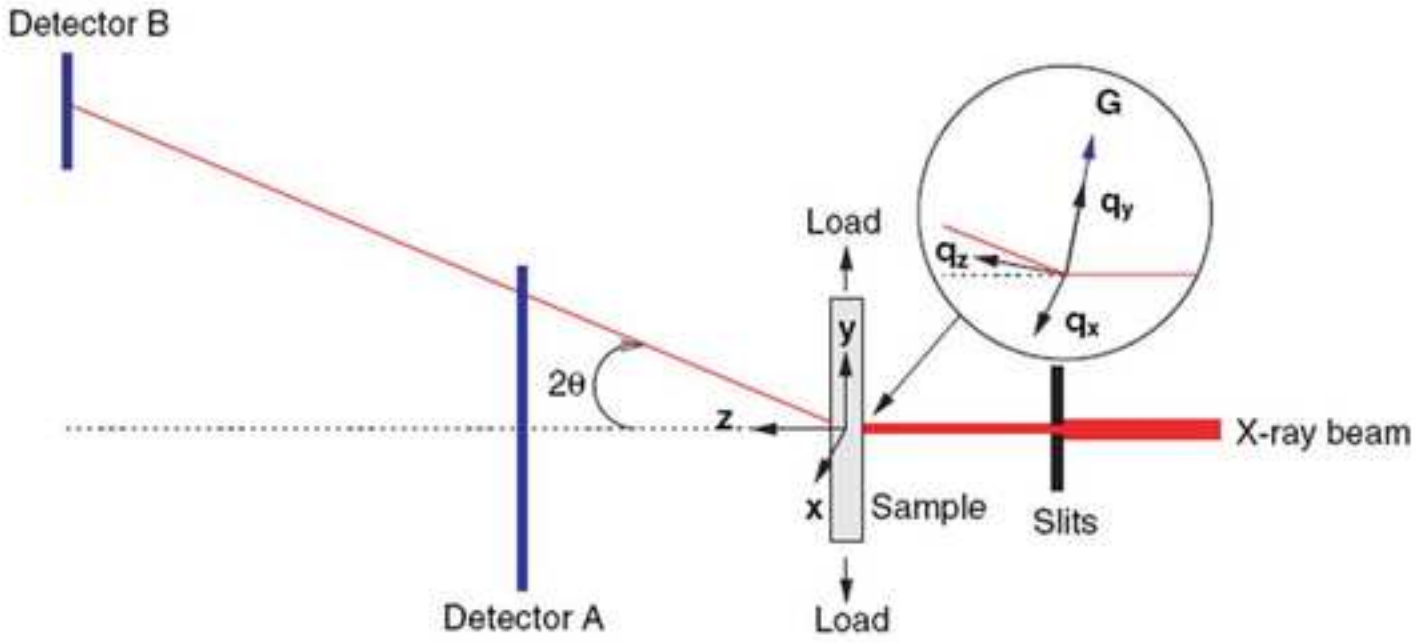

(a)

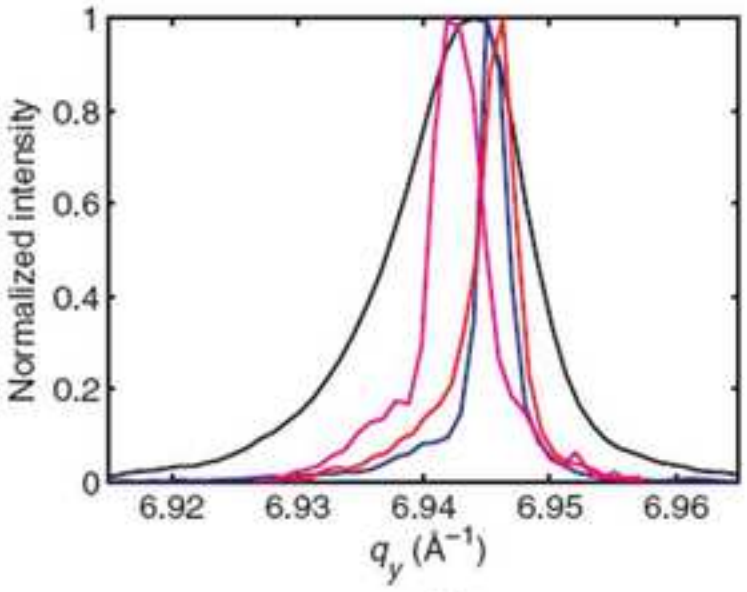

(b)

Figure 13
Click here to download high resolution image

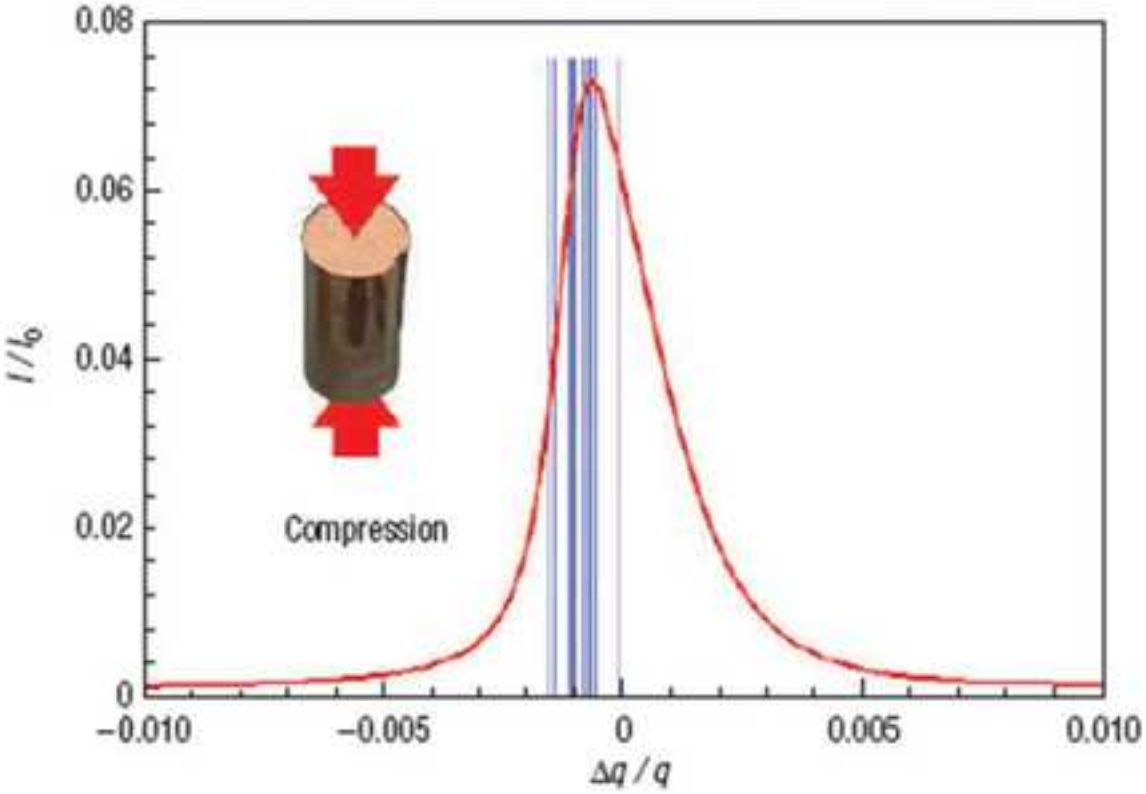

(a)

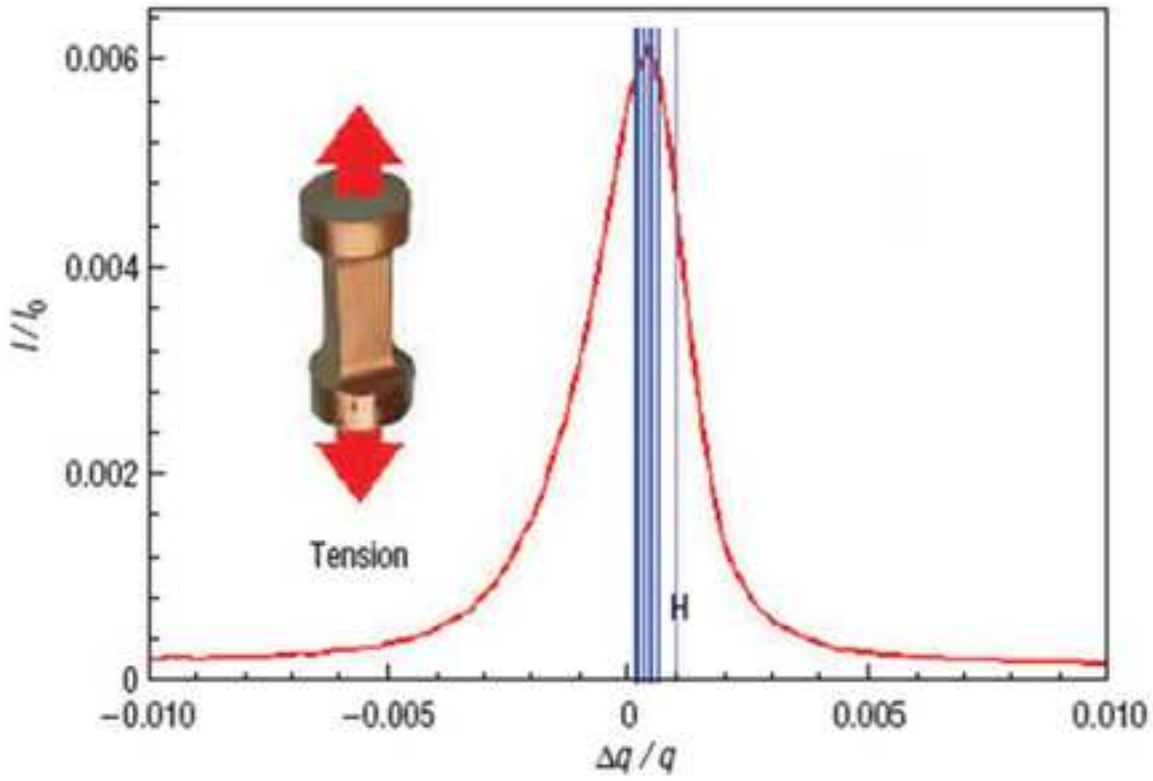

(b)

Figure 14
Click here to download high resolution image

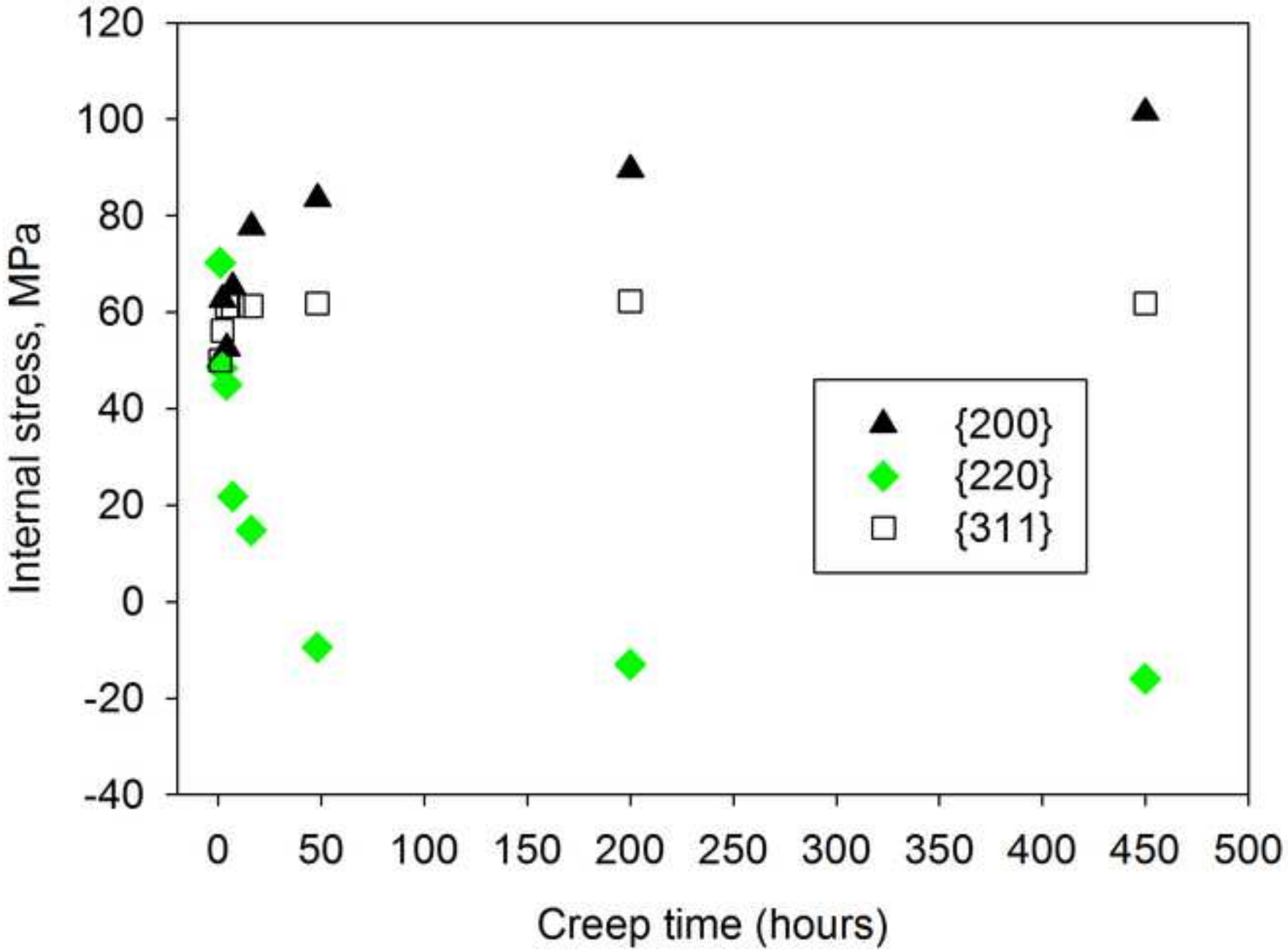

Figure 15
Click here to download high resolution image

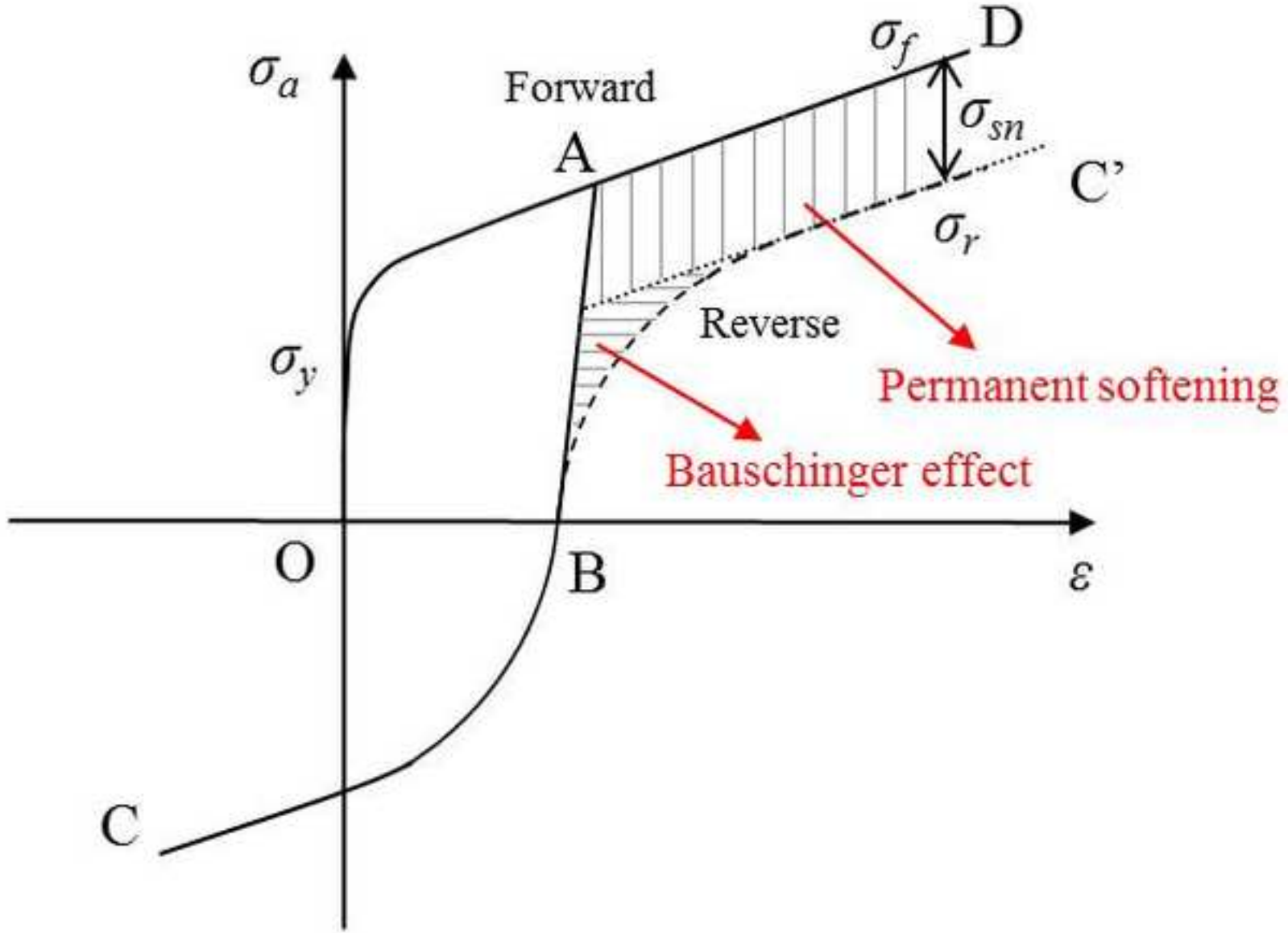

Figure 16 (a)
Click here to download high resolution image

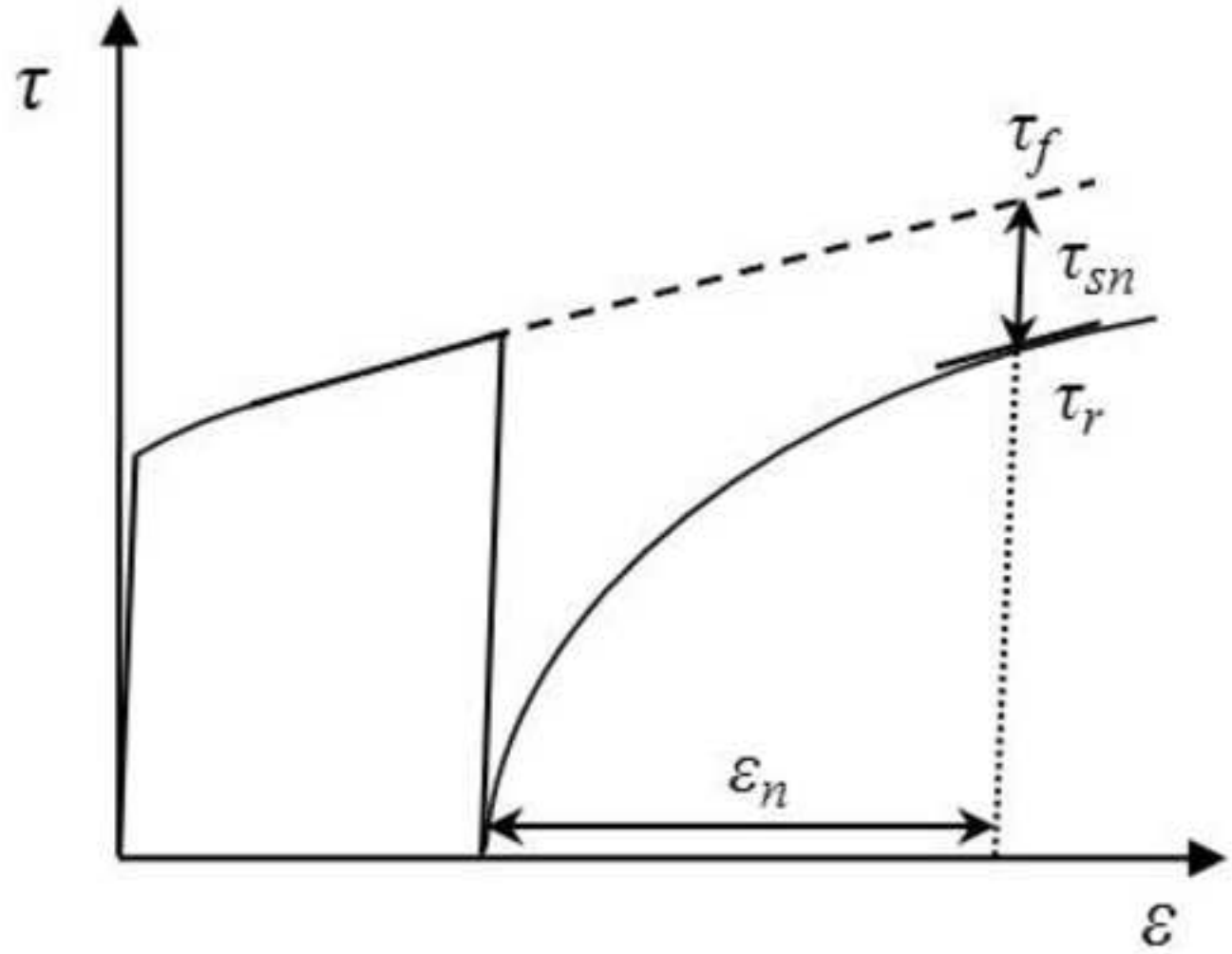

(a)

Figure 16 (b)
Click here to download high resolution image

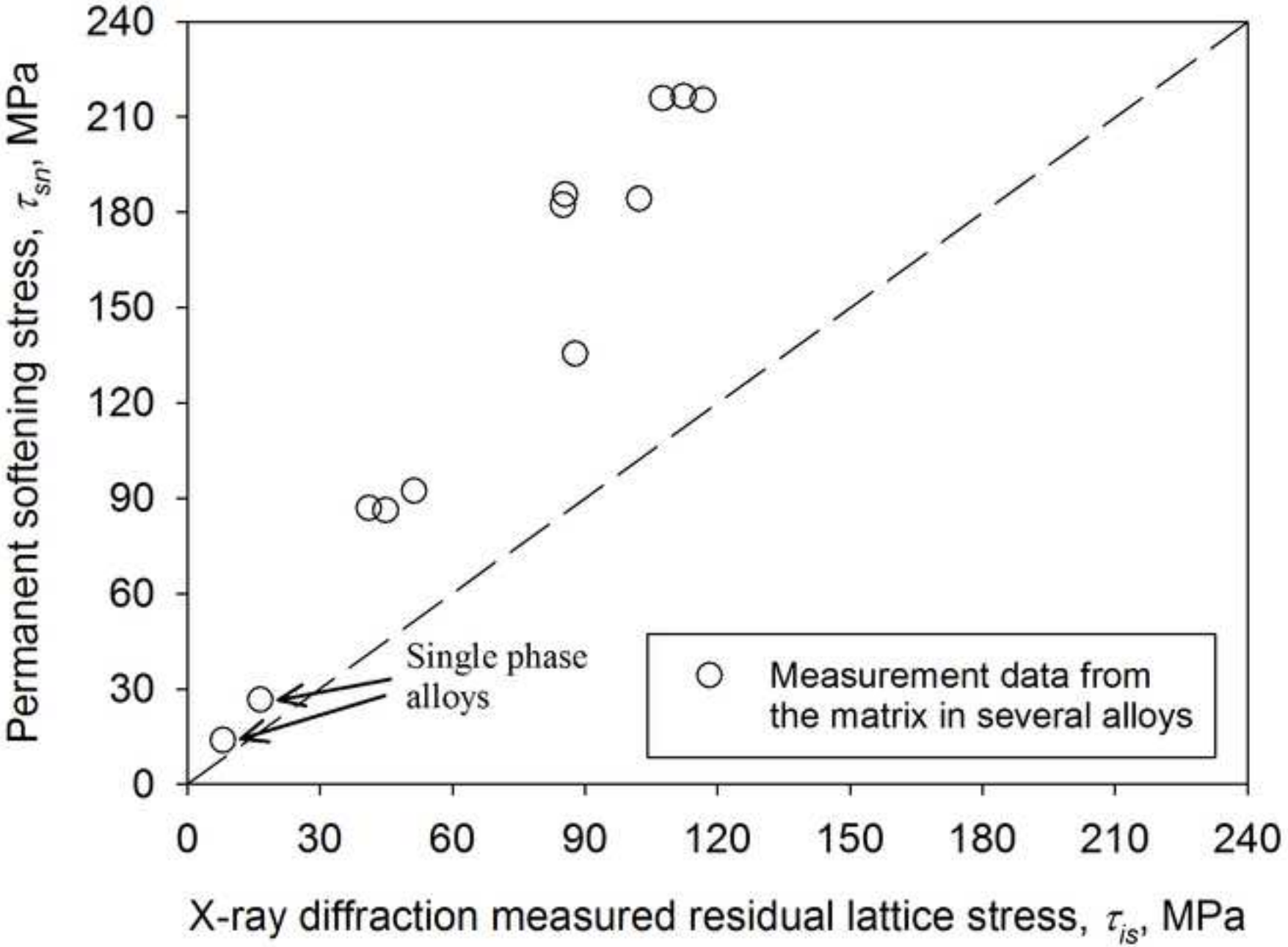

Figure 17
Click here to download high resolution image

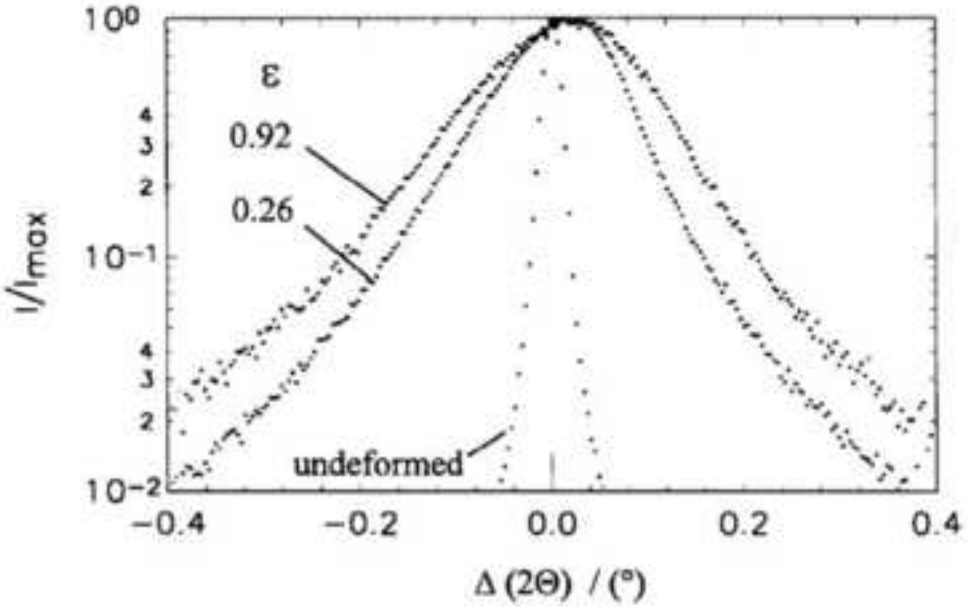

(a)

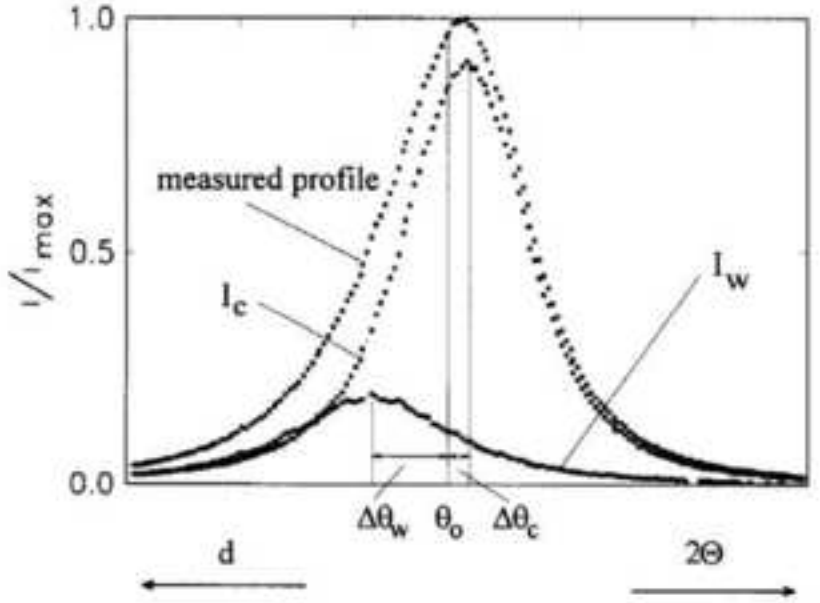

(b)

Figure 18
Click here to download high resolution image

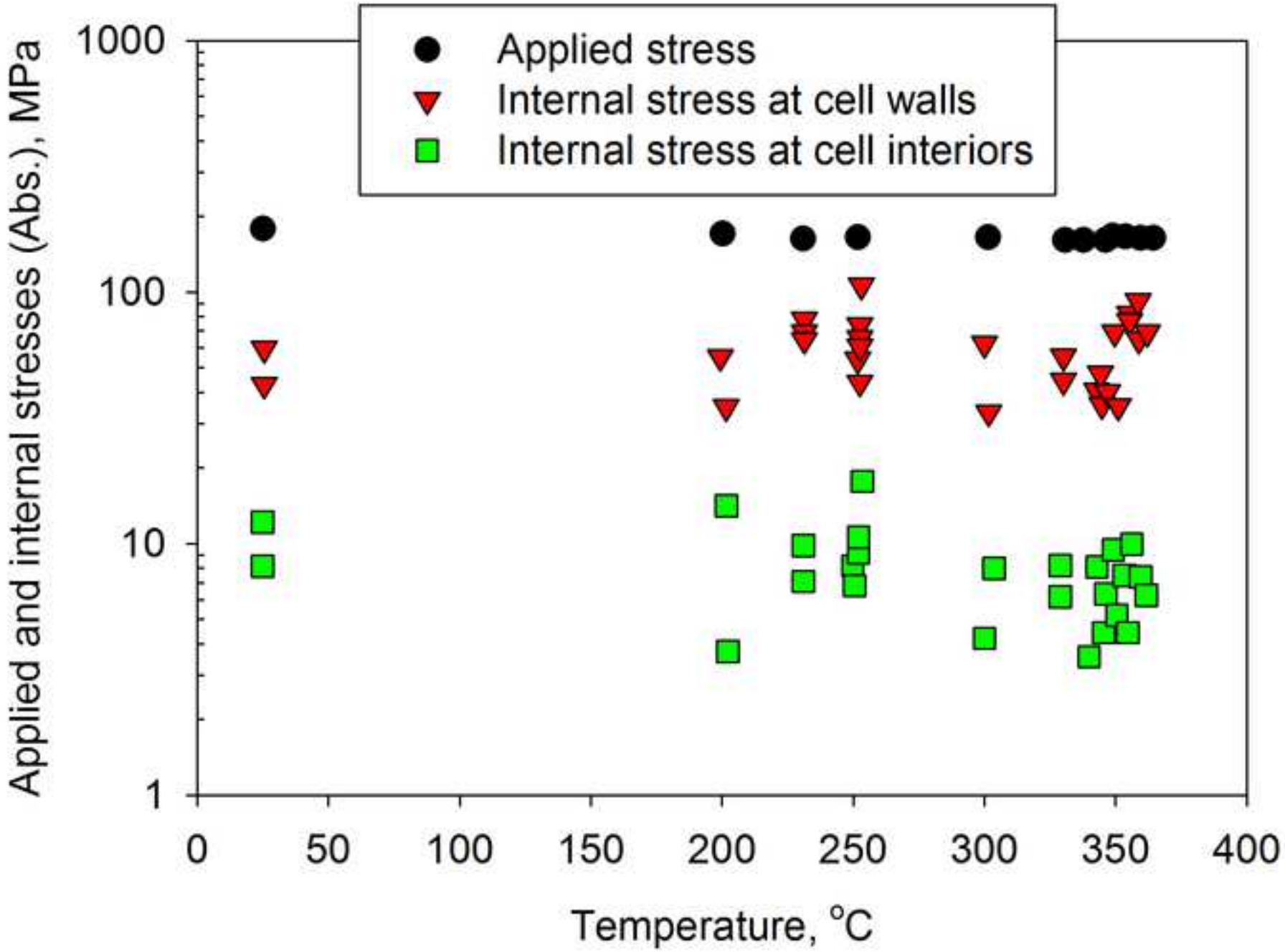

Figure 19
Click here to download high resolution image

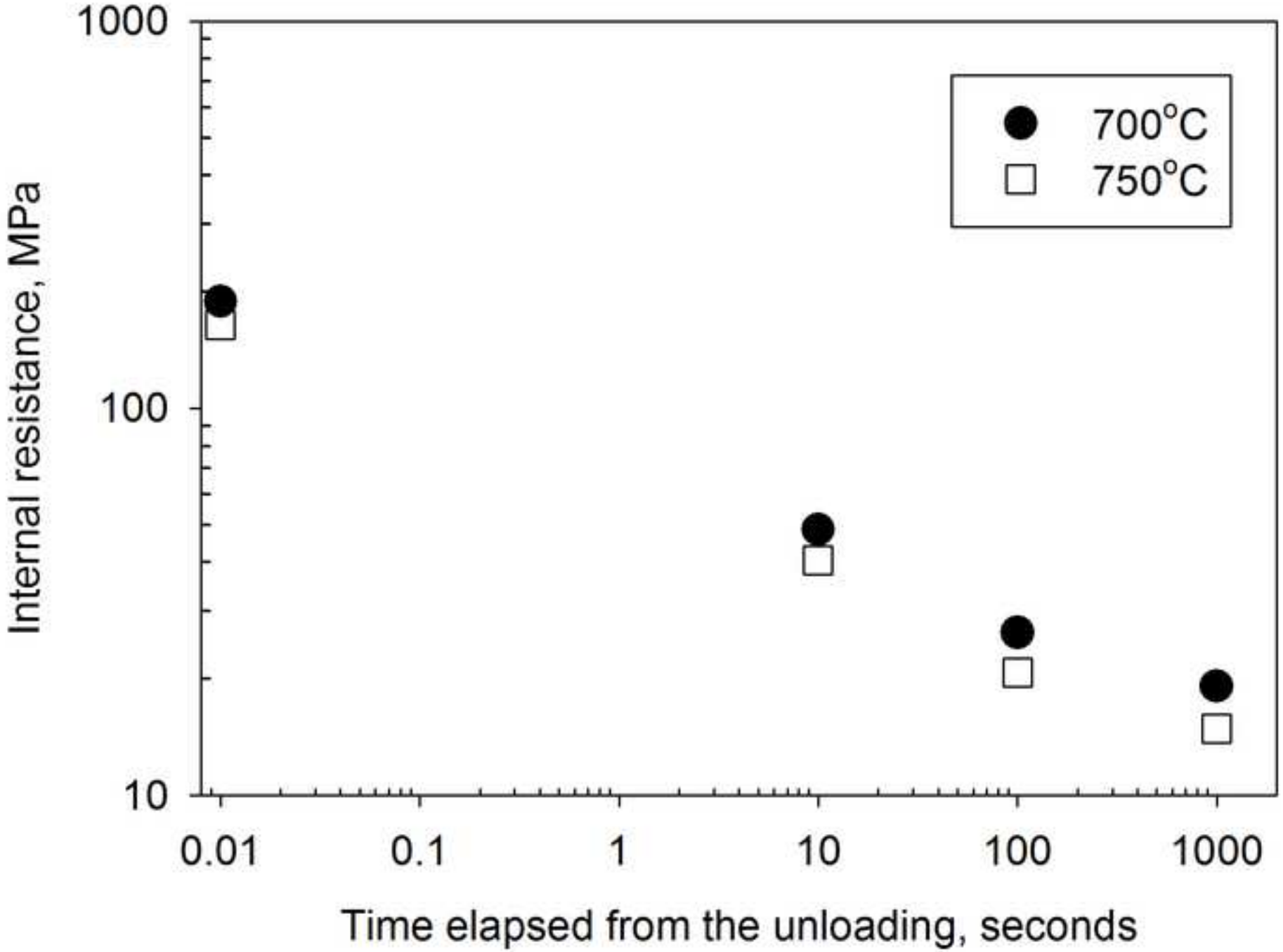

Figure 20
Click here to download high resolution image

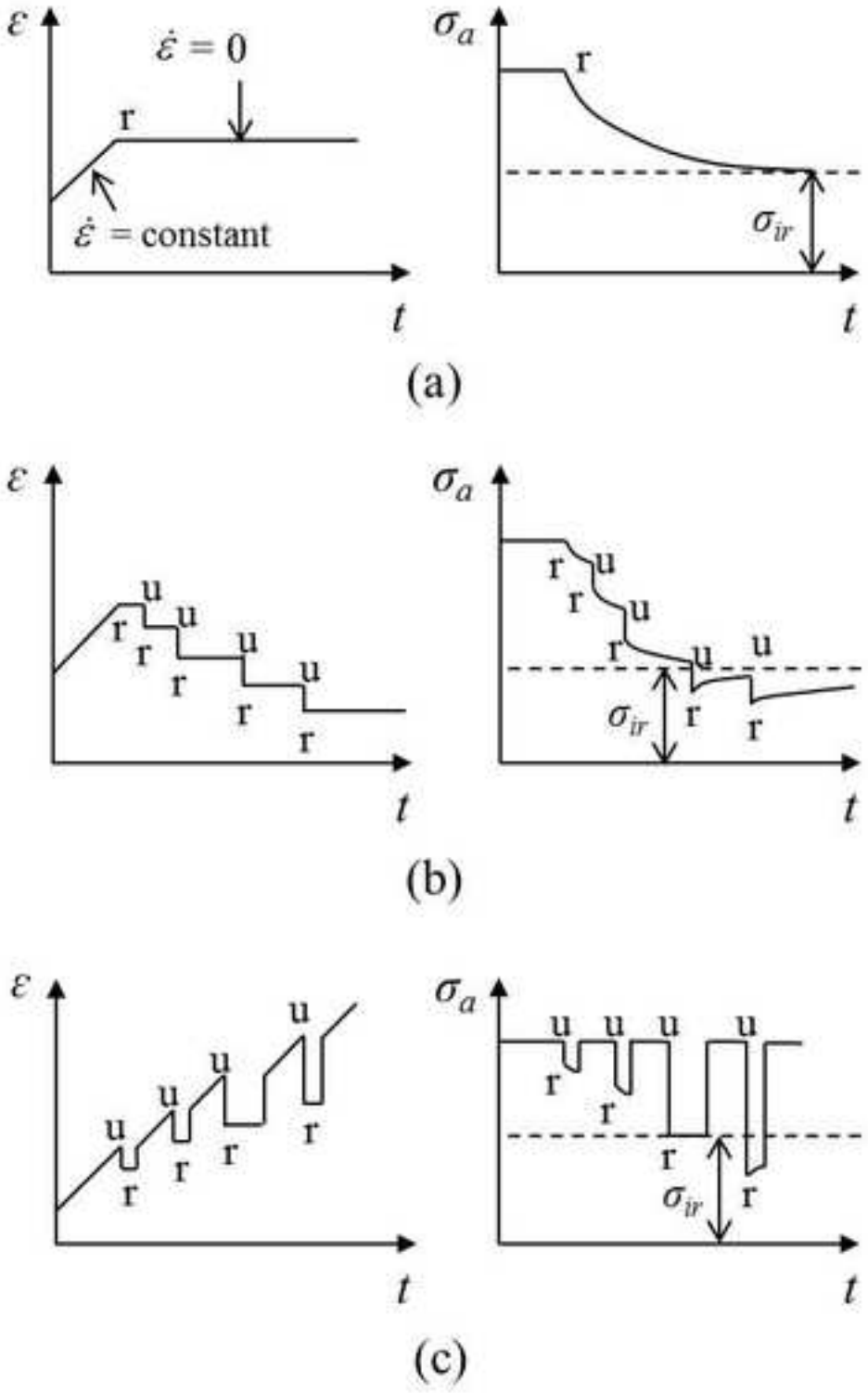

Figure 21
Click here to download high resolution image

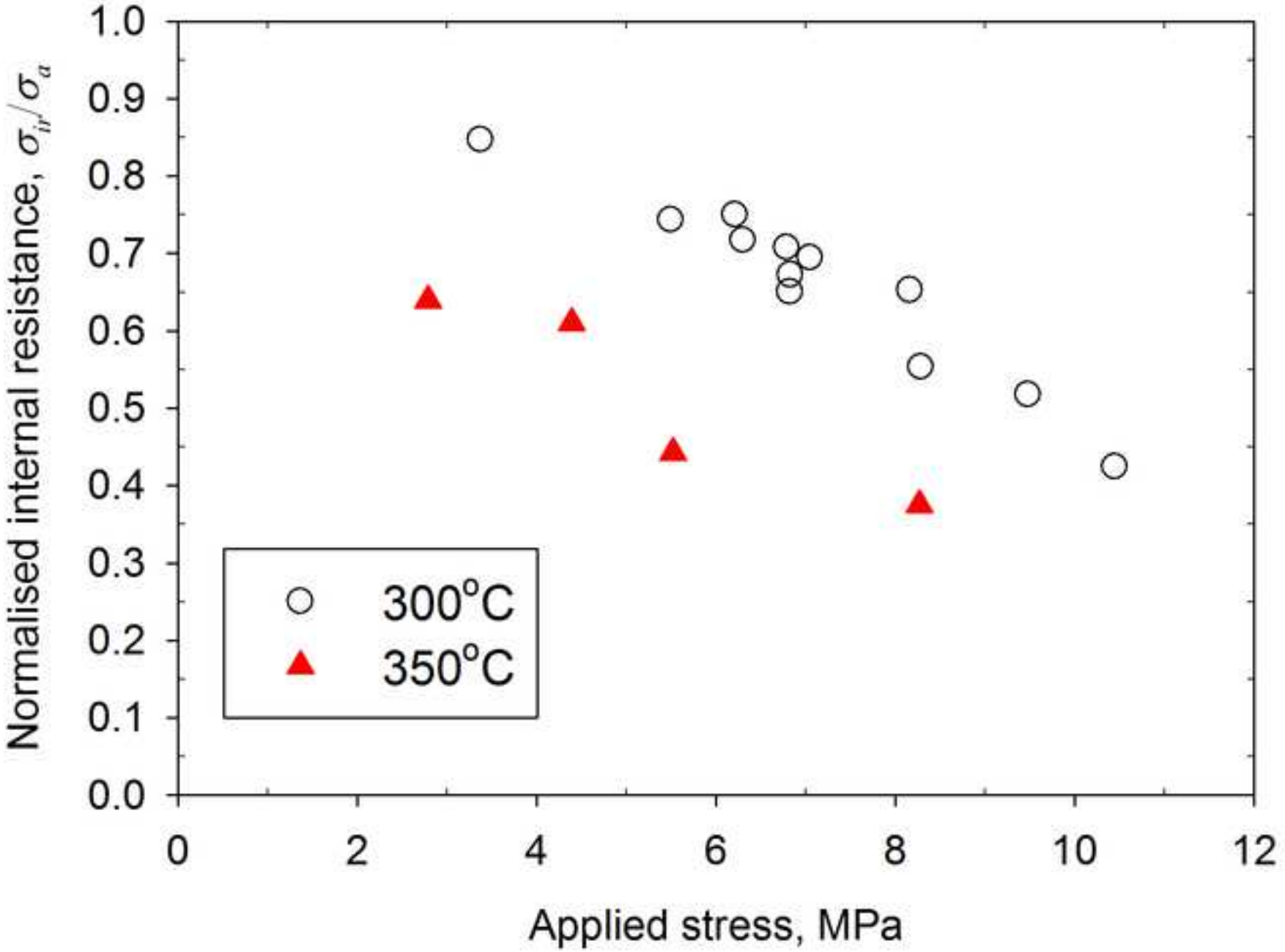

Figure 22
Click here to download high resolution image